Modeling of radiofrequency ablation

Master's thesis

January 2019

Student: R.B. Hijlkema

Primary supervisor: Dr. P.G. Dendooven

Secondary supervisor: Dr. ir. P.M.A. van Ooijen

RUBEN HIJLKEMA

ACKNOWLEDGEMENTS

CONTENTS

INTRODUCTION

Radiofrequency (RF) ablation is a minimally invasive technique broadly used for treating tumors in a wide variety of biological tissues (liver [1], kidney [2], bone [3], prostate [4], and breast [5]). RF ablation is used when the surgical removal of the tissue is unfeasible due to the location of the tissue or the collateral damage in the surgical process. RF ablation involves the placement of a needle-like electrode at the target tissue, combined with ground pads attached to the patient. When a voltage is applied to the needle, an electrical potential will be established, and therefore current will flow. The current flow results in resistive heating, due to the resistance of the tissue in the vicinity of the needle. This, in turn, will induce thermal necrosis in the target tissue. The volume to which the thermal necrosis extends is known as the *ablation zone*. The success of this treatment depends on the extent of the temperature field and the minimization of damage to healthy tissue with a reasonable margin prescribed by an oncologist or surgeon.

For providing optimal treatment, it is highly desired to have a predictive value over the ablation volume after ablation. However, this is highly non-trivial as the ablation volume is not only dependent on treatment parameters, such as duration of ablation, needle placement and applied voltage, but also on patient-specific parameters, such as, blood flow [6], electrical conductivity of the target tissue [7], and the presence of major vascular structures, which can act as heat sinks [8]. Therefore, there is a risk that not all target cells will be destroyed, and treatment is ineffective. Recurrence rates of tumors after RF ablation have been reported up to 60% [9].

The target temperature of RF ablation is usually between 90 - 105 °C. At around 100 °C water content of tissue starts to evaporate and carbonization of tissue occurs [10]. As a result, the power deposited in the tissue is sub-optimal. To achieve and optimize the temperature profile, different kinds of RF ablation systems exist. These include monopolar electrodes, bipolar electrodes, multi-prong ('umbrella type'), and *Cool-Tip* electrodes. In the latter, the electrode is actively cooled during the process to avoid carbonization at the electrode.

Furthermore, the regulation of the power delivery can be adjusted too. In general, two different types of control are used, temperature and impedance control. Temperature controlled electrodes monitor the temperature at the tip of the electrode and adjust the delivered power according to a preset target temperature, whereas an impedance control system monitors the impedance of the system, which will
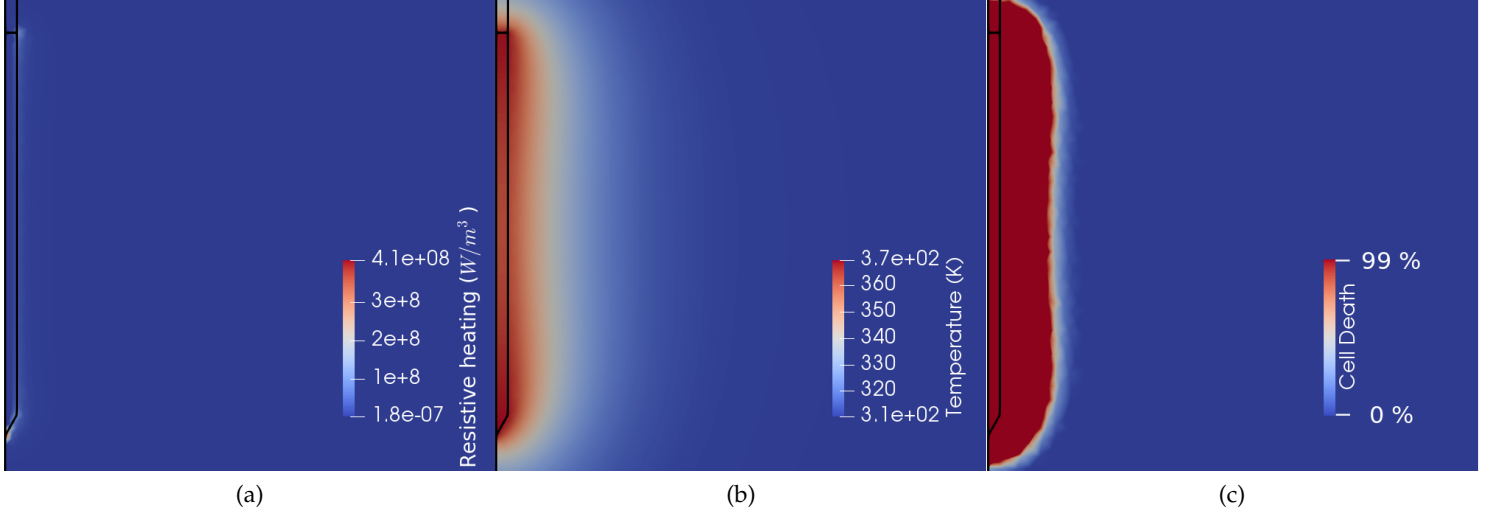
Figure 1: Example distributions of quantities associated with RF ablation. The black outline denotes the electrode. (a) The heat generated due to resistive heating. (b) A temperature distribution. (c) A cell death distribution

show an increase when tissue carbonizes. If this impedance reaches a threshold, the system will stop delivering power for some time; usually a couple of seconds, to let the tissue cool before power is resumed [11].

Further examples of what the model should contain are given in figure 1. First, due to the resistive heating of the electrode, heat is continuously generated as seen in figure 1(a). Then, the accumulation and diffusion of this heat must be modeled by a form of the heat equation, which will give us the temperature distribution, as seen in figure 1(b). However, secondary effects such as cooling due to blood perfusion and phase change phenomena should be accounted for too. Last, for there to be a predictive value of the ablation zone, we need the inclusion of a cell death model. Such a model should be able to relate the temperature history to a quantity which can tell if a cell has died. The result is a cell death distribution, as seen in 1(c).

The objective of this thesis is to provide a model that can describe the different processes involved in RF ablation, including different geometries and different patient-specific properties. In the end, a simulation model has been created, which can handle the RF ablation process for three-dimensional models, as well as, two-dimensional, axisymmetric models. Furthermore, the model includes; temperature-dependent material properties, handling of phase-change phenomena, different power control schemes, different cell death models and two time stepping schemes. The details of the above are given in chapter 3. Furthermore, figure 12 shows a simplified schematic of the model.

It is, however, always important to verify the implementation of the model. A simple coding mistake can give entirely different results. Therefore, chapter 4 has been dedicated to various tests which show if various parts of the model have been implemented correctly.

After the model has been verified, simulations have been performed on models of Atypical Cartilaginous Tumors (ACTS). Furthermore, pre- and post-procedure image-data was available for four patient cases having such a tumor. Patient-specific models were created from the pre-procedure image-data on which simulations were performed and the results compared against the post-procedure image-data.

However, before we can proceed, we need to know how to obtain results as seen in figure 1. As it turns out, these processes are governed by (non-)linear partial differential equations. A finite element approach has been chosen, as it allows for the approximation of partial differential equations, on a predefined model. In the following chapter, the basis of this method will be explained.

THE FINITE ELEMENT METHOD

The Finite Element Method (FEM) has been an active field of research since the 1940s [12]. As such, there is a plethora of literature on the topic. The following chapter is influenced by a number of authors and acts as a short introduction to the fundamentals, and concepts which are used to validate the model.

In particular, *Introduction to Numerical Methods for Variational Problems* by Langtangen and Mardal [13], which has an excellent introduction to the variational method from a general point of view. Also, *Li et al.* gives a great overview of the function spaces relevant to the finite element method in *Theoretical Foundations of the Finite Element Method* [14]. Lecture notes of Flaherty [15] on the finite element method consist of a concise write-up of the errors associated with the finite element method, and in particular, the convergence of the error with respect to the types of elements and basis functions used. These lecture notes have been of tremendous help in understanding the *a-priori* error-analysis. As such, a similar route is taken with regards to the explanation of the relevant results for our model, glancing over many details found in the original notes. Finally, *Advanced Finite Element Methods* by Sonnendrücker and Ratnani [16] gave insight in the practical implementation of different boundary conditions.

2.1 APPROXIMATION OF VECTORS

FEM is a method for obtaining numerical solutions to partial differential equations (PDE) on a given domain. Within the FEM, approximate solutions are found on sub-domains, known as *finite elements*. The collection of all elements within a domain is known as a *mesh*. The mesh allows for the calculation of approximate solutions on complex geometries, including geometries consisting of more than one material type. The goal of FEM is to find an approximate solution to a PDE in the form of

$$u(x) \approx \sum_{i=0}^{n} c_i N_i(x) \tag{2.1.1}$$

Where $N(x)$ are predefined functions and c_i are unknown coefficients to be determined. To illustrate how one arrives at such a solution it is more intuitive to look at the approximation of vectors. This introductory will then be generalized to the approximation of functions and finally to the FEM.
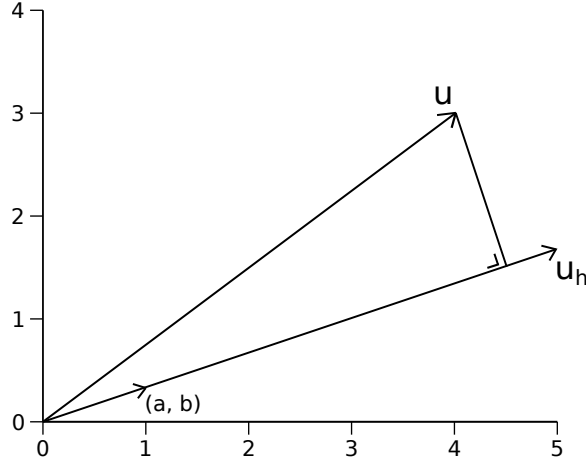
Figure 2: Approximation of a vector u by a vector u_h, which is constrained to lie along (a, b). Finding the best approximation requires minimizing the distance between u and u_h.

2.1.1 *One-dimensional vector space*

The simplest vector approximation problem is one where a vector is approximated by another, which is restricted to be aligned with another vector. To demonstrate this, let $\mathbf{u} = (4, 3)$ be a vector in the xy plane and $\mathbf{u}_h$ our approximation which is confined to be aligned with a vector (a, b), see figure 2. First we define a vector space V spanned by the vector $\mathbf{N}_0 = (a, b)$:

$$V = span\{\mathbf{N}_0\} \qquad (2.1.2)$$

Here $\mathbf{N}_0$ is the basis vector of space V. Next, our goal is to find the best approximation, $\mathbf{u}_h$, to $\mathbf{u}$:

$$\mathbf{u}_h = c_0 \mathbf{N}_0 \in V \qquad (2.1.3)$$

To arrive at a best approximation we have to define a metric which assesses the quality of the approximation in some way. A method is to require the length of the difference, the error, to be minimized. The length of the error is given by the norm:

$$\|e\| = \sqrt{\langle e, e \rangle} \qquad (2.1.4)$$

where $< \mathbf{a}, \mathbf{b} >$ denotes the inner product of vector $\mathbf{a}$ and $\mathbf{b}$.

2.1.1.1 *Least squares method.*

Now that we have defined an error norm, we can derive the coefficient c_0 for which $\mathbf{u}_h$ is optimal. This is done by minimizing the error-norm, $\|e\|$, or rather, the square of the error-norm $\|e\|^2$.

First we define the error as the difference between the actual solution and the approximate solution:

$$e(c_0) = \mathbf{u} - \mathbf{u}_h = \mathbf{u} - c_0\mathbf{N}_0 \qquad (2.1.5)$$

then, the squared norm is:

$$\|e(c_0)\|^2 = (\langle \mathbf{u} - c_0\mathbf{N}_0, \mathbf{u} - c_0\mathbf{N}_0\rangle) \qquad (2.1.6)$$

$$= \mathbf{u} \cdot \mathbf{u} - 2c_0(\mathbf{u} \cdot \mathbf{N}_0) + c_0^2(\mathbf{N}_0 \cdot \mathbf{N}_0) \qquad (2.1.7)$$

Minimizing $\|e(c_0)\|^2$ is equivalent to requiring the derivative to be zero:

$$\frac{\partial\|e(c_0)\|^2}{\partial c_0} = 0 \qquad (2.1.8)$$

Substituting eq. 2.1.7 into 2.1.8 we arrive at:

$$-2(\mathbf{u} \cdot \mathbf{N}_0) + 2c_0(\mathbf{N}_0 \cdot \mathbf{N}_0) = 0 \qquad (2.1.9)$$

Which is equivalent to:

$$\{\mathbf{u} - c_0\mathbf{N}_0, \mathbf{N}_0\rangle = \{e, \mathbf{N}_0\rangle = 0 \qquad (2.1.10)$$

Rearranging the terms in 2.1.9 leads to:

$$c_0 = \frac{\mathbf{u} \cdot \mathbf{N}_0}{\mathbf{N}_0 \cdot \mathbf{N}_0} \qquad (2.1.11)$$

Substituting our vectors, $\mathbf{u} = (4,3), \mathbf{N}_0 = (a,b)$, into the expression above leads to:

$$c_0 = \frac{4a + 3b}{a^2 + b^2} \qquad (2.1.12)$$

2.1.1.2 *The Galerkin method*

Here Now we show that minimizing $\|e\|^2$ is the same as demanding that:

$$\langle e, v\rangle = 0 \qquad \forall \quad v \in V \qquad (2.1.13)$$

In other words, e must be orthogonal to any vector v in V. Referring back to figure 2 we see that this makes sense in a geometric way, as the orthogonal vector, e, has the shortest distance between the two.

Any $v \in V$ can be written as $v = c\mathbf{N}_0$, and thus we demand that:

$$\langle e, c\mathbf{N}_0\rangle = c\langle e, v\rangle = 0 \qquad (2.1.14)$$

Which reads that the error must be orthogonal to the *basis* function in V:

$$\langle e, \mathbf{N}_0\rangle = 0 \qquad (2.1.15)$$

which we also found by the least squared method in eq. 2.1.10. This method of minimization is referred to as projection or the Galerkin method

2.1.1.3 *The Galerkin method in higher-dimension vector spaces*

The previous section was valid for a one-dimensional vector space. Here we will generalize the Galerkin method to arbitrary dimensions. The goal is to find the best approximation to a vector $\mathbf{u}$ in the space V, spanned by basis-functions, $\mathbf{N}_i$:

$$V = \operatorname{span}\{\mathbf{N}_0, \cdots, \mathbf{N}_n\} \tag{2.1.16}$$

It is assumed that the dimension of V is $n+1$ and that the basis vectors are linearly independent. Now we can write any $u_h \in V$ as a linear combination of the basis vectors:

$$u_h = \sum_{j=0}^{n} c_j \mathbf{N}_j \tag{2.1.17}$$

with $c_j \in \mathbb{R}$. Then for the Galerkin method we require that the error, $\mathbf{e}$, is orthogonal to all $v \in V$:

$$\langle \mathbf{e}, v \rangle = 0 \qquad \forall \quad v \in V \tag{2.1.18}$$

And since any $v \in V$ can be rewritten as the sum of its basis vectors (eq. 2.1.17) we end up with:

$$\langle \mathbf{e}, \sum_{i=0}^{n} c_i \mathbf{N}_i \rangle = \sum_{i=0}^{n} c_i \langle \mathbf{e}, \mathbf{N}_i \rangle = 0 \tag{2.1.19}$$

To find an optimum value of c_i, we must require that the individual contributions to the sum vanish, i.e.:

$$\langle \mathbf{e}, \mathbf{N}_i \rangle = 0, \qquad i = 0, \cdots, n \tag{2.1.20}$$

Remembering that $e = u - u_h$ and using equation 2.1.17 we can write that:

$$\langle \mathbf{u} - \sum_{i=0}^{n} c_i \mathbf{N}_i, \mathbf{N}_j \rangle = \langle \mathbf{u}, \mathbf{N}_i \rangle - \sum_{j=0}^{n} \langle \mathbf{N}_i, \mathbf{N}_j \rangle c_j = 0 \tag{2.1.21}$$

concluding:

$$\sum_{j=0}^{n} \langle \mathbf{N}_i, \mathbf{N}_j \rangle c_j = \langle \mathbf{u}, \mathbf{N}_i \rangle, \qquad i = 0, \cdots, n \tag{2.1.22}$$

Which is a linear system of $n+1$ equations and $n+1$ unknowns and can be written as:

$$\sum_{j=0}^{n} A_{i,j} c_j = b_j \tag{2.1.23}$$

where

$$A_{i,j} = \langle \mathbf{N}_i, \mathbf{N}_j \rangle \tag{2.1.24}$$

$$b_j = \langle \mathbf{N}_i, \mathbf{u} \rangle \tag{2.1.25}$$

2.2 APPROXIMATION OF FUNCTIONS

Analogous to approximating vectors, we can extend the Galerkin method to deal with the approximation of functions. Instead of a vector space , let V be a function space spanned by a set of basis functions $N_0, \cdots, N_n$

$$V = \mathrm{span}\{N_0, \cdots, N_n\} \tag{2.2.1}$$

such that any function $u \in V$ can be written as a linear combination of the basis functions:

$$u = \sum_{j=0}^{n} c_j N_j \tag{2.2.2}$$

Now let us find the best approximation, $u_h(x) \in V$, of an arbitrary function $u(x)$. Analogous to the previous section, we have to minimize the error, $e(x)$, which is equivalent to minimizing the distance $u(x) - u_h(x)$, previously expressed through the inner product of two vectors. This leaves us with finding the equivalent of the inner product for functions. Where the inner product of two discretized vectors involved pairwise summation, the inner product of two arbitrary functions, $g(x)$ and $f(x)$, is conceptually similar. In this case we integrate the product of both functions on their shared domain, denoted by Ω:

$$\langle f, g \rangle = \int_\Omega f(x)g(x)dx \tag{2.2.3}$$

Now that we have defined the inner product for functions, the minimization problem can be stated as:

$$\langle e, v \rangle = 0, \qquad \forall \quad v \in V \tag{2.2.4}$$

or:

$$\int_\Omega e(x)v(x)dx = 0, \qquad \forall \quad v \in V \tag{2.2.5}$$

Which is also known as the projection of a function on a subspace V.

Again since any $v \in V$ can be written in the form of equation 2.2.2, we can write

$$\langle e, \sum_{i=0}^{n} c_i N_i \rangle = 0, \tag{2.2.6}$$

Once more, to find an optimum value for c_i, we require that the individual contributions vanish

$$\langle e, N_i \rangle = 0, \quad i = 0, \cdots, n \tag{2.2.7}$$

rewriting the left hand side

$$\langle e, \sum_{i=0}^{n} N_i \rangle = \int_{\Omega} e(x) \sum_{i=0}^{n} N_i \, dx \qquad (2.2.8)$$

$$= \int_{\Omega} (u - \sum_{j=0}^{n} c_j N_j) N_i \, dx \qquad (2.2.9)$$

$$= \int_{\Omega} u N_i - \sum_{j=0}^{n} N_i N_j c_j \, dx \qquad (2.2.10)$$

and requiring it to be zero leads to:

$$\sum_{j=0}^{n} \int_{\Omega} N_i N_j c_j \, dx = \int_{\Omega} u N_i \, dx \qquad (2.2.11)$$

or:

$$\sum_{j=0}^{n} \langle N_i, N_j \rangle c_j = \langle u, N_i \rangle \qquad (2.2.12)$$

And we end up with a similar linear system of equations for approximating functions as in the vector case (equation 2.1.23).

2.2.1 *Lagrange polynomials*

As stated in the previous section, we need to use basis-functions for the construction of the approximation. Let us take a look at the most simple basis-function, the family of linear functions.

For that, let $\Omega = [x_0, x_1]$ be an interval on the real axis and $V(\Omega)$ the function space of linear functions on Ω, defined by:

$$V(\Omega) = \{v : v(x) = c_0 + c_1 x\} \quad \text{with} \quad \begin{cases} x & \in \Omega \\ c_0, c_1 & \in \mathbb{R} \end{cases} \qquad (2.2.13)$$

In other words, $V(\Omega)$ contains all functions of the form $v(x) = c_0 + c_1 x$ on Ω. In this case v has two degrees of freedom, as every function can be uniquely determined by its coefficients, c_0 and c_1. However, it is also possible to define v by another set of degrees of freedom.

Every linear function can be uniquely defined by a set of points that satisfy that function. In fact, any pair of points within Ω will function as degrees of freedom for v. To this end, we claim that function v can be uniquely determined by the values at its endpoints of Ω, $\beta_0 = v(x_0)$ and $\beta_1 = v(x_1)$.

proof: Let the end-points of v on $\Omega = [x_0, x_1]$ be defined as:

$$c_0 + c_1 x_0 = \beta_0 \qquad (2.2.14)$$

$$c_0 + c_1 x_1 = \beta_1 \qquad (2.2.15)$$
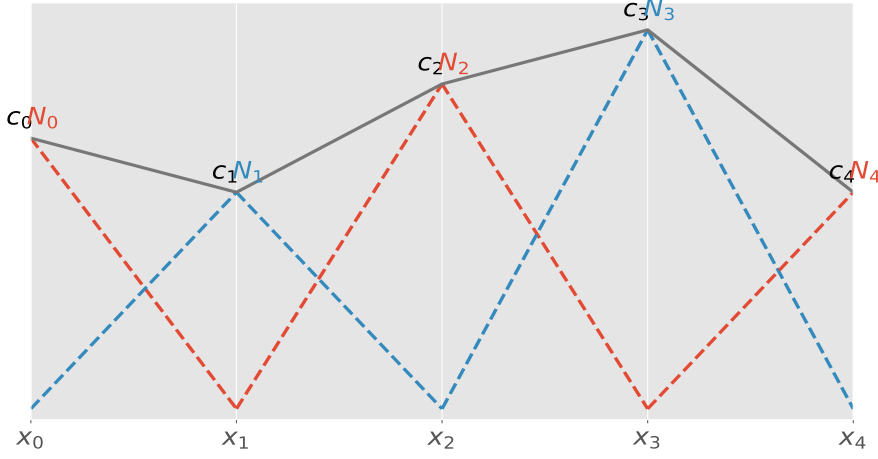
Figure 3: A piecewise continuous function constructed from a Lagrangian nodal basis of degree one. Note how each N in the bulk (N_1, N_2, N_3) forms a triangular structure, from which it derives its nickname of 'hat-functions'. Similarly, functions at the boundaries (N_0, N_4), only form 'half-hat-functions'.

Writing it as a linear system:

$$\begin{bmatrix} 1 & x_0 \\ 1 & x_1 \end{bmatrix} \begin{bmatrix} c_0 \\ c_1 \end{bmatrix} = \begin{bmatrix} \beta_0 \\ \beta_1 \end{bmatrix} \tag{2.2.16}$$

The determinant of this system equals $x_1 - x_0$, which is nothing but the length of the interval Ω. The determinant is positive, and thus there exists a unique solution to the linear system. The end-points of Ω (x_0, x_1) are referred to as *nodes* within the context of the FEM.

The next step is to define a new basis for our function space $V(\Omega)$, the so called *nodal*-basis shown in figure 3. From this figure it is seen that a piecewise continuous function can be uniquely defined by its nodal values. Consequently, for each set of nodal values, there exists one unique function $v \in V$, where each basis function can now be written as

$$N_j(x) \begin{cases} 0 & x < x_{i-1}, \\ (x - x_{i-1})/(x_i - x_{i-1}) & x_{i-1} \leqslant x \leqslant x_i, \\ 1 - (x - x_i)/(x_{i+1} - x_i) & x_i < x \leqslant x_{i+1} \\ 0 & x > x_{i+1} \end{cases} \tag{2.2.17}$$

which has the property

$$N_j(x_i) = \begin{cases} 1, & \text{if} \quad i = j \\ 0, & \text{if} \quad i \neq j \end{cases}, \quad i, j = 0, 1, \cdots, n \tag{2.2.18}$$

This nodal basis is orthogonal as it takes on the value of unity at its own index, and zero everywhere else. This allows us to write our

function v as a linear combination of the nodal basis and its coefficients:

$$v = \sum_{i=0}^{n} c_i N_i(x) \tag{2.2.19}$$

In fact, the above nodal basis is known as a *Lagrange* polynomial, of degree one. We can extend the notation to an arbitrary degree of n:

$$\mathbb{P}(x) = \prod_{j=0, j \neq i}^{n} \frac{x - x_j}{x_i - x_j} \tag{2.2.20}$$

All $\mathbb{P}$ are polynomials of various degrees, usually denoted $\mathbb{P}^n$, and all exhibit the property as in equation 2.2.18.

The orthogonal properties of the basis functions within the finite element method is a desired one, but not required. As we will show in the next section, the use orthogonal basis functions will lead to a strictly tridiagonal coefficient matrix. In practice, these kinds of matrices are much easier to handle as they often require less computational operations due to the sparsity of the matrix.

2.2.2   *One dimensional approximation*

In this section, we will demonstrate how we use the nodal basis to find an approximation.

To this end, let u be the function to be approximated and u_h our approximation, both on an interval Ω. Let this interval be divided into n non-overlapping sub-intervals e.g.:

$$\Omega = \Omega^{(0)} \cap \cdots \cap \Omega^{(n)} \tag{2.2.21}$$

Each sub-interval, $\Omega^{(n)}$, is known as an *element* which can be uniquely numbered. Now each sub interval contains a number of points, the so called *nodes*. Together they form a *mesh*.

Let the exact solution be $u = x^2$ and u_h its approximation, based on the Lagrangian basis functions of degree one, $\mathbb{P}^{(1)}$. In the previous sections, it was derived that finding the best approximation is requiring that the inner product of the error w.r.t some function basis vanishes. Since these basis functions can only retrieve the exact solutions of polynomials up to its order (in this case one), we expect there to be an error. For the approximation, we will use a uniform partitioned mesh of three elements, on the interval $\Omega \in [0, 3]$.

Figure 3 shows our basis functions. Here the advantage of the orthogonality property of the basis-functions, as stated in equation 2.2.18, becomes apparent. The basis functions associated with each node, i.e., N_i, only overlap their adjacent elements. This means that most of the entries of A will be zero. In fact, A will form a tridiagonal matrix. Such a matrix is in practice much easier to work with

and limits the number of calculations compared to a non-orthogonal basis-function.

To demonstrate this, we assemble the coefficient matrix A, also known as the *stiffness* matrix within FEM. We will use the fact that the length of the interval of a uniform partitioned mesh is the same as, $h = x_i - x_{i-1}$ and our formulation of the basis as in equation 2.2.17.

We first start with assembling the matrix for nodes not associated with a boundary. As seen in figure 3 we see that these form so-called 'hat-functions' due to their shape, and overlap with their neighbors. Lastly, we consider the two special cases at the boundary, which only form 'half-hat' functions and only overlap with one other function. For the non-boundary nodes

$$A_{i,i} = \int_\Omega N_i^2 \, dx \tag{2.2.22}$$

$$= \int_{x_{i-1}}^{x_i} \left(\frac{x - x_{i-1}}{h}\right)^2 dx + \int_{x_i}^{x_{i+1}} \left(1 - \frac{x - x_{i+1}}{h}\right)^2 dx \tag{2.2.23}$$

$$= \frac{2h}{3} \tag{2.2.24}$$

For the integrals involving the function basis at the edges, we denote that in this case there is only one element involved and thus:

$$A_{0,0} = A_{n,n} = \frac{h}{3} \tag{2.2.25}$$

Now for the off diagonal indices:

$$A_{i,i-1} = A_{i-1,i} = \int_\Omega N_i N_{i-1} \, dx \tag{2.2.26}$$

$$= \int_{x_i-2}^{x_i+1} N_i N_{i-1} \, dx \tag{2.2.27}$$

$$= \int_{x_i-2}^{x_i-1} N_i N_{i-1} + \int_{x_i-1}^{x_i} N_i N_{i-1} + \int_{x_i}^{x_i+1} N_i N_{i-1} \tag{2.2.28}$$

$$= \int_{x_i-1}^{x_i} N_i N_{i-1} \tag{2.2.29}$$

$$= \int_{x_{i-1}}^{x_i} \left(1 - \frac{x - x_{i-1}}{h}\right)\left(\frac{x - x_i}{h}\right) dx \tag{2.2.30}$$

$$= \frac{h}{6} \tag{2.2.31}$$

Now we assemble the tridiagonal matrix A for our mesh with 3 elements on Ω, and thus 4 nodes:

$$A = \frac{h}{6} \begin{bmatrix} 2 & 1 & 0 & 0 \\ 1 & 4 & 1 & 0 \\ 0 & 1 & 4 & 1 \\ 0 & 0 & 1 & 2 \end{bmatrix} \tag{2.2.32}$$

Now for b_i we denote that the product of $N_i b_i \neq 0$ only over the interval of the basis. And thus for the node basis not associated with the boundary, $(i \neq 0, i \neq n)$, we have:

$$b_i = \int_{x_{i-1}}^{x_i} \left(\frac{x - x_i}{h}\right) u(x)\,dx + \int_{x_i}^{x_{i+1}} \left(1 - \frac{x - x_{i-1}}{h}\right) u(x)\,dx, \quad i \neq 0, i \neq n \tag{2.2.33}$$

and for basis on the boundary:

$$b_0 = \int_0^{x_{i+1}} \left(1 - \frac{x}{h}\right) u(x)\,dx \tag{2.2.34}$$

and respectively,

$$b_n = \int_{x_{n-1}}^{x_n} \left(\frac{x - x_n}{h}\right) u(x)\,dx \tag{2.2.35}$$

Assembling b is a bit more cumbersome as it requires the integral of the function $u(x)$ over different sub-intervals. Nevertheless, for our example we end up with:

$$b = \frac{1}{12} \begin{bmatrix} 1 & 14 & 50 & 43 \end{bmatrix}^{\mathsf{T}} \tag{2.2.36}$$

Now substituting 2.2.32 and 2.2.36 into 2.2.11 we end up with:

$$\frac{h}{6} \begin{bmatrix} 2 & 1 & 0 & 0 \\ 1 & 4 & 1 & 0 \\ 0 & 1 & 4 & 1 \\ 0 & 0 & 1 & 2 \end{bmatrix} \begin{bmatrix} c_0 \\ c_1 \\ c_2 \\ c_3 \end{bmatrix} = \frac{1}{12} \begin{bmatrix} 1 \\ 14 \\ 50 \\ 43 \end{bmatrix} \tag{2.2.37}$$

Solving the above system leads to our best approximation:

$$c = \frac{1}{12} \begin{bmatrix} -2 & 10 & 46 & 106 \end{bmatrix}^{\mathsf{T}} \tag{2.2.38}$$

The result is shown in figure 4.

The results of this approximation, is just that, an approximation. It should be intuitive that splitting the domain into more elements yields a better result, and that the approximate solution should converge to the analytic solution as the number of elements is increased.
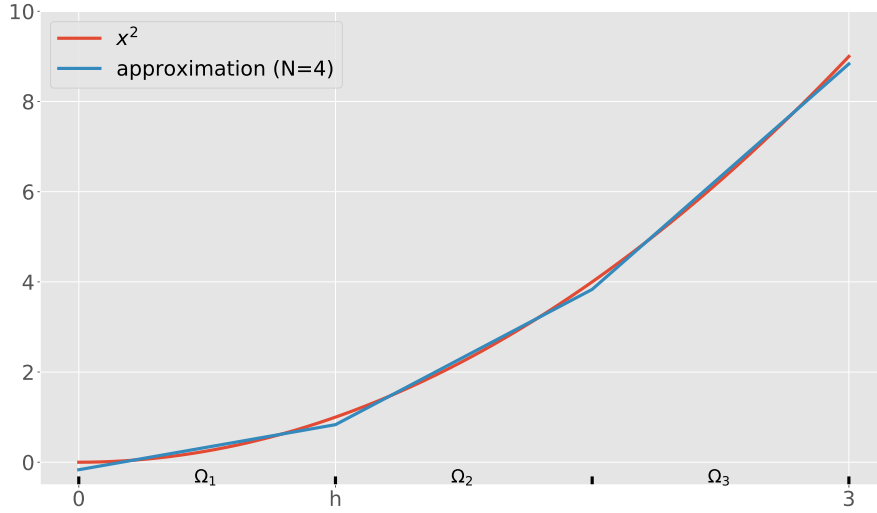
Figure 4: The approximation to x^2 over the domain $\Omega \in [0,3]$ by the Galerkin method, using Lagrangian basis functions of order one. The mesh consisted of four equally spaced nodes (N=4), and three sub-intervals Ω_i, $i = 1, 2, 3$.

However, knowing the convergence of the solution with respect to some mesh parameter gives valuable insight into the error of the method, also known as the *a-priori* error estimation. To arrive at an exact convergence rate for the Galerkin projection is not trivial. Instead, we look for an upper bound of the error in some norm. For this we need the *interpolation*, or *collocation* method.

2.2.3 *Linear interpolation*

The simplest linear approximation of a function f based on a mesh of n nodes is the piecewise continuous function where the coefficients are defined by the function values evaluated at the node coordinates. This is known as interpolation.

To define how well our interpolant approximates the real function, we have to define the error, e, in some norm. To this end we use the $L^2(\Omega)$-norm, provided that v is a square integrable function, meaning that;

$$\int_\Omega |v|^2 < \infty \tag{2.2.39}$$

Then the $L^2(\Omega)$-norm is defined as:

$$\|v\|^2_{L^2(\Omega)} = \int_\Omega |v|^2 dx \tag{2.2.40}$$

2.2.4   *Error of interpolation*

In this section we will make some preliminary claims on the error of our interpolation. To this end we will use the fundamental theorem of calculus [17]

$$f(x_1) = f(x_0) + \int_{x_0}^{x_1} f'(x)\,dx \tag{2.2.41}$$

and the *Cauchy-Schwartz* inequality [18]

$$\left| \int_\Omega f(x)g(x)\,dx \right|^2 \leqslant \int_\Omega |f(x)|^2\,dx \int_\Omega |g(x)|^2\,dx \tag{2.2.42}$$

Now let f be a continuous function on $\Omega = [x_0, x_1]$ and g the linear interpolant of f with nodes at the end-points of Ω:

$$g(x) = f(x_0)\lambda_0 + f(x_1)\lambda_1 \tag{2.2.43}$$

Then let the interpolation error be defined as:

$$e(x) = f(x) - g(x) \tag{2.2.44}$$

Now using equation 2.2.41 we can write the error of any $x_i \in \Omega$ as:

$$e(x_i) = e(x_0) + \int_{x_0}^{x_i} e'(x)\,dx \tag{2.2.45}$$

Using the fact that linear interpolation is exact at the mesh nodes, e.g. $e(x_0) = 0$

$$e(x_i) = \int_{x_0}^{x_i} e'(x)\,dx \tag{2.2.46}$$

$$\leqslant \int_{x_0}^{x_i} |e'(x)|\,dx \tag{2.2.47}$$

$$\leqslant \int_\Omega 1 \cdot |e'(x)|\,dx \tag{2.2.48}$$

$$= \int_\Omega \sqrt{(1 \cdot |e'(x)|)^2}\,dx \tag{2.2.49}$$

$$\leqslant \sqrt{\int_\Omega 1^2\,dx \int_\Omega e'^2(x)\,dx} \quad \text{(eq. 2.2.42)} \tag{2.2.50}$$

$$= \sqrt{h}\,\|e'(x)\|_{L^2(\Omega)} \tag{2.2.51}$$

Where h is the length of domain Ω. Thus we obtain:

$$e(x_i)^2 \leqslant h\|e'\|_{L^2(\Omega)}^2 \tag{2.2.52}$$

First integrating the left hand side over Ω:

$$\int_\Omega e(x_i)^2\,dx_i = \|e(x)\|_{L^2(\Omega)}^2 \tag{2.2.53}$$

For the right hand side of equation 2.2.52, as it does not depend on x_i, we end up with:

$$\int_\Omega h\|e'(x)\|^2_{L^2(\Omega)}\,dx_i = h^2\|e'(x)\|^2_{L^2(\Omega)} \tag{2.2.54}$$

Combining the two results in our first expression for the interpolation error:

$$\|e(x)\|_{L^2(\Omega)} \leqslant h\|e'(x)\|_{L^2(\Omega)} \tag{2.2.55}$$

Next we want to make a preliminary claim on the estimate of $\|e'(x)\|_{L^2(\Omega)}$. First, let us start again by stating:

$$e'(x_i) = e'(x_0) + \int_{x_0}^{x_i} e''(x)\,dx \tag{2.2.56}$$

However, this won't allow us to make a simplification as $e'(x_0)$ generally does not equal zero. Now remember that our approximation at nodes was exact, in other words $e(x_0) = e(x_1) = 0$. Then, there must be a point $\gamma = \{\gamma \in \Omega : e'(\gamma) = 0\}$. Thus, allowing us to write

$$e'(x_i) = e'(\gamma) + \int_\gamma^{x_i} e''(x)\,dx = \int_\gamma^{x_i} e''(x)\,dx \tag{2.2.57}$$

Following the same steps as our first claim, we end up with:

$$\|e'(x)\|_{L^2(\Omega)} \leqslant h\|e''(x)\|_{L^2(\Omega)} \tag{2.2.58}$$

Combining equation 2.2.55 and 2.2.58:

$$\|e(x)\|_{L^2(\Omega)} \leqslant h\|e'(x)\|_{L^2(\Omega)} \leqslant h^2\|e''(x)\|_{L^2(\Omega)} \tag{2.2.59}$$

Since our interpolation is linear in nature, the second derivative of the error is nothing but the second derivative of our original function:

$$\|e(x)\|_{L^2(\Omega)} \leqslant h^2\|f''(x)\|_{L^2(\Omega)} \tag{2.2.60}$$

$$\|e'(x)\|_{L^2(\Omega)} \leqslant h\|f''(x)\|_{L^2(\Omega)} \tag{2.2.61}$$

Extending this we can make a similar claim to the interpolation error of a piecewise continuous function, $g \in V$:

$$\|f - g\|_{L^2(\Omega)} = \sum_{i=0}^n \|f - g\|_{L^2(\Omega)} \tag{2.2.62}$$

$$\leqslant \sum_{i=0}^n h_i^2\|f''(x)\|_{L^2(\Omega)} \tag{2.2.63}$$

And since we know that the Galerkin method retrieves the best approximation we have

$$e_{Galerkin} \leqslant e_{collocation} \leqslant \sum_{i=0}^n h_i^2\|f''(x)\|_{L^2(\Omega)} \tag{2.2.64}$$

h	$||u_e - u_h||_{L^2}$	r_{L^2}
1	2.36×10^1	-
$\frac{1}{2}$	4.33×10^0	2.00
$\frac{1}{4}$	9.43×10^{-1}	2.00
$\frac{1}{8}$	2.21×10^{-1}	2.00

Table 1: Convergence rates (r_{L^2}) of the error ($||u_e - u_h||_{L^2}$) of the Galerkin approximation on the Lagrangian basis functions of degree one. With the exact solution, $u_e = x^2$, and h denoting the element size. The domain of interest was $\Omega \in [0,3]$.

In other words, the error converges quadratically w.r.t the mesh size when Lagrangian basis functions of order one are considered.

We can test this result by reconsidering the problem as in figure 4, refining the mesh, i.e., adding more elements, and calculating the convergence rate. Doing so should retrieve the quadratic convergence as stated in equation 2.2.64. The convergence rate between two subsequent solutions can be calculated as

$$r = \frac{\ln(\frac{e_{i+1}}{e_i})}{\ln(\frac{h_{i+1}}{h_i})} \qquad (2.2.65)$$

where e_{i+1}, e_i are the errors, and h_{i+1}, h_i the element length of the two solutions respectively.

The resulting convergence rates are shown in table 1. The expected quadratic convergence results are retrieved, meaning that we have a correct implementation of the Galerkin method. As we will see later on, testing the finite element method w.r.t the expected convergence is a powerful method for validating the implementation of finite element method.

2.3   THE FINITE ELEMENT METHOD

In this section, we will see that the finite element method follows the same principles as in the sections mentioned above. To make proper claims we have to introduce more rigorous definitions of the techniques used in the previous sections. To this end, we start with the definition of function spaces. One of these is the *Sobolev space*, fundamental for the finite element method. If a solution to a partial differential equation exists, it will belong to some Sobolev space.

2.3.1 *Function spaces*

A function space is a topological space whose points are functions. A most basic function space is the function space of continuous functions on the domain Ω:

$$C(\Omega) = C^0(\Omega) = \{f, \, f \text{ is continuous on } \Omega\} \qquad (2.3.1)$$

This function space is said to be linear as any combination of $\alpha, \beta \in \mathbb{R}$ and $f_1 \in C(\Omega), f_2 \in C(\Omega)$ can be written as $\alpha f_1 + \beta f_2 \in C(\Omega)$. Further, the function space of functions of multiple variables with continuous derivatives up to order m can be written as:

$$C^m(\Omega) = f(x_1, x_2, \cdots, x_n), \quad D^\alpha f \text{ are continuous on } \Omega, |\alpha| \leqslant m \qquad (2.3.2)$$

where $D^\alpha f$ is the partial derivative written in *multi-index* notation [19], i.e.:

$$D^\alpha f(x) = \frac{\delta^{|\alpha|} f}{\delta x_1^{\alpha_1} \delta x_2^{\alpha_2} \cdots \delta x_n^{\alpha_n}}, \qquad |\alpha| = \alpha_1 + \alpha_2 + \cdots + \alpha_n, \alpha_i \geqslant 0 \qquad (2.3.3)$$

A function space which has a distance defined is known as a *metric space*. The distance in $C^m(\Omega)$, between two functions f, g can be defined as:

$$d(f, g) = \max_{0 \leqslant |\alpha| \leqslant m} \qquad (2.3.4)$$

Similarly to the space of continuous functions, we can define spaces for integrable functions. These are known as the $L^p(\Omega)$ spaces, or the *Lebesque spaces*, and is defined as:

$$L^p(\Omega) = \left\{ f(x), \int_\Omega |f(x)|^p \, dx \right\}^{\frac{1}{p}} \qquad (2.3.5)$$

The distance in an $L^p(\Omega)$ space is defined as:

$$d(f, g) = \left(\int_\Omega |f - g|^p \, dx \right)^{\frac{1}{p}} \qquad (2.3.6)$$

The special case of $p = 2$ results in a *Hilbert space*. Hilbert spaces are function spaces which have a corresponding inner product defined.

2.3.2 *Weak derivative and Sobolev spaces*

The weak derivative is a generalization for functions who are not differentiable but are locally integrable, that is to say $f \in L_{loc}^1$. Then the definition is as follows:

Let $u \in L_{loc}^1$, and α be a multi-index. A function $v \in L_{loc}^1$ is said to be an α-th *weak derivative* of u if:

$$\int_\Omega u D^\alpha \psi \, dx = (-1)^{|\alpha|} \int_\Omega v \psi \, dx, \qquad \forall \psi \in C_0^\infty(\Omega) \qquad (2.3.7)$$
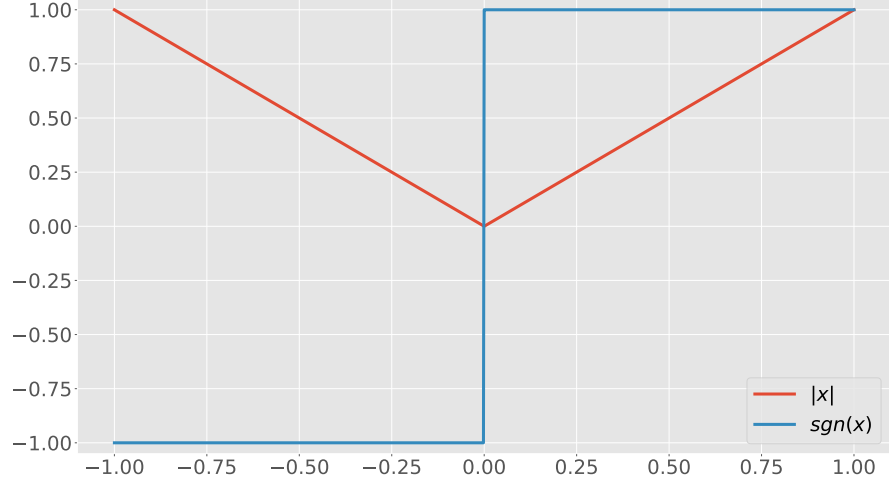
Figure 5: The function $|u(x)|$ and its weak derivative $sgn(x)$

For example, consider the absolute function $u(x)$:

$$u(x) = \begin{cases} -x, & x < 0 \\ x, & x \geqslant 0 \end{cases} \qquad (2.3.8)$$

Which has no classical derivative as the function is not differentiable at $x = 0$. However it does have a weak derivative, known as the sign function:

$$sgn(x) = \begin{cases} -1, & x < 0, \\ 0, & x = 0, \\ 1, & x > 0 \end{cases} \qquad (2.3.9)$$

which is a function not in C, but rather in H^1, a *Sobolev space*. Sobolev space is the space of functions possessing weak derivatives such as above. The Sobolev space for functions without a derivative is:

$$H^0(\Omega) = L^2(\Omega) = \left\{ f(x), \int_\Omega |f|^2 dx < \infty \right\} \qquad (2.3.10)$$

and involving first order derivatives:

$$H^1(\Omega) = \left\{ v(x), D^\alpha v \in L^2(\Omega), |\alpha| \leqslant 1 \right\} \qquad (2.3.11)$$

and of general dimension:

$$H^m(\Omega) \left\{ v(x), D^\alpha v \in L^2(\Omega), |\alpha| \leqslant m \right\} \qquad (2.3.12)$$

These Sobolev spaces are important as it will allows us to find the solution to a partial differential equation in the *weak* sense. The term *weak* can be understood as a loosening of the restrictions on the approximation. This in turn allows for the search of the solution in terms

of continuous functions on elements, instead of the whole domain, as seen in figure 5. The need for this requirement arises naturally in the finite element method as the geometry is divided into domains. Furthermore, since $H^m(\Omega)$ is a Hilbert space, it is equipped with the inner product. In particular, the inner product of $H^0(\Omega)$ is the same as for $L^2(\Omega)$:

$$\langle u, v \rangle_{H^0(\Omega)} = \langle u, v \rangle_{L^2(\Omega)} = \int_\Omega uv dx \qquad (2.3.13)$$

and for $H^1(\Omega)$:

$$\langle u, v \rangle_{H^1(\Omega)} = \int_\Omega (uv + u'v') dx \qquad (2.3.14)$$

The Sobolev space has also a norm defined from its inner product. The H^0 norm is defined as:

$$\|u\|_{H^0(\Omega)} = \|u\|_{L^2(\Omega)} = \left(\int_\Omega |u|^2 dx \right)^{\frac{1}{2}} \qquad (2.3.15)$$

the H^1 *semi*-norm:

$$|u|_{H^1(\Omega)} = \left(\int_\Omega (|\nabla u|)^2 dx \right)^{\frac{1}{2}} \qquad (2.3.16)$$

These norms will be useful when analyzing the convergent properties of the finite element method.

2.3.3   *The variational method*

Now that we have introduced the various function spaces, we show how they arise within the Finite element method using the variational method. To this end, consider *Poisson's equation*.

Let $f \in L^2(\Omega)$, then:

$$-\Delta u = f, \quad \in \Omega \qquad (2.3.17a)$$

$$u = 0, \quad \text{on} \quad \delta\Omega \qquad (2.3.17b)$$

where Δ is the Laplace operator. The first step in the variational method is to transform the above *strong form* into its corresponding *weak form*. This is achieved by multiplying eq. 2.3.17a by a *test-function* $v \in H^1(\Omega)$ on both sides

$$\int_\Omega \Delta u v dx = \int_\Omega f v dx \qquad (2.3.18)$$

And redistributing the second-order derivative to both u and the test-function. This can be achieved by a use of Greens formula, or integration by parts

$$\int_\Omega \nabla u \cdot \nabla v dx - \int_{\delta\Omega} \frac{\delta u}{\delta n} v ds = \int_\Omega f v dx \qquad (2.3.19)$$

Where n is the outward normal at any point of the boundary.

By redistributing the derivatives, we have 'weakened' the requirements imposed on the solution, u, and we can search for the solution in $H^1(\Omega)$. Also, the above problem showcases *essential* boundary conditions, as u does not appear directly in the boundary integral as opposed to v. Since ultimately u and v will be in the same function space, we can incorporate the boundary condition directly in the test space where we only consider functions of v vanishing on the boundary e.g.:

$$H_0^1(\Omega) = \left\{ v(x), \quad v = 0 \quad \text{on} \quad \delta\Omega, \quad v \in H^1(\Omega) \right\} \tag{2.3.20}$$

Then the variational formulation reads:
Find $u \in H_0^1(\Omega)$ such that

$$\int_\Omega \nabla u \cdot \nabla v dx = \int_\Omega f v dx, \quad \forall v \in H_0^1(\Omega) \tag{2.3.21}$$

Once again we arrive at the Galerkin problem:
find $u \in H_0^1(\Omega)$ such that:

$$A(u, v) = \langle f, v \rangle \tag{2.3.22}$$

where

$$\langle f, v \rangle = \int_\Omega f v dx \tag{2.3.23}$$

$$A(u, v) = \int_\Omega \nabla u \cdot \nabla v dx \tag{2.3.24}$$

Existence and uniqueness of the solution are shown by the *Lax-Milgram theorem* [20], which states:

Let V be a Hilbert space equipped with the norm $\|\cdot\|_V$. Let A(u, v) be a continuous, symmetric and coercive bilinear form on V x V, i.e.

1. *Continuity: there exist C such that $\forall u, v \in V$*

$$|A(u, v)| \leqslant C\|u\|_V\|v\|_V \tag{2.3.25}$$

2. *Coercivity: there exists a constant $\alpha > 0$ such that $\forall u \in V$*

$$A(u, u) > \alpha\|u\|_V^2 \tag{2.3.26}$$

Let f(.) be a continuous linear form on V, i.e. there exists C such that $\forall v \in V$

$$|f(v)| \leqslant C\|u\|_V \tag{2.3.27}$$

Then there exists a unique $u \in V$ such that

$$A(u, v) = f(v), \quad \forall v \in V \tag{2.3.28}$$

2.3.4 *Finite element approximation*

To arrive at a computable solution, we want to have a finite number of equations. To this end, we have to look for the solution in a finite dimensional space V_h, which should be a subspace of $H_0^1(\Omega)$. For example, we can take the subspace of piecewise continuous functions which vanish on the boundary

$$V_h = \{v_h, \quad v_h = 0 \text{ on } \delta\Omega, \quad v_h \text{ is piecewise continuous}\} \quad (2.3.29)$$

Now reconsider the Galerkin problem stated in equation 2.3.22. To transform it into a finite element problem consider any finite dimensional space $V_h \in H_0^1$ spanned by a set of basis functions $N_0, \cdots, N_n$

$$V_h = span(N_0, \cdots, N_n) \quad (2.3.30)$$

such that any function $u \in V_h$ can be written as a linear combination of the basis functions, i.e.

$$u = \sum_{j=0}^{n} c_j N_j \quad (2.3.31)$$

Since any function can be written in the above form, we can write the approximate solution, u_h, accordingly

$$u_h = \sum_{j=0}^{n} c_j N_j \quad (2.3.32)$$

where the coefficients, c_j, are chosen such that

$$A(u_h, v_h) = \langle f, v_h \rangle, \quad \forall v_h \in V_h \quad (2.3.33)$$

Here we enforce the weak form in the space of V_h instead of H_0^1. In general, this will lead to an approximation error. This is conceptually similar to the vector approximation in figure 2, where the approximated solution was constrained by another vector and also introduced an approximation error. Still, it can be shown that the finite element solution is the best solution with respect to some norm.

Realizing that a linear combination of basis functions can represent any element, we arrive at a linear system of equations

$$A\langle \sum_{j=0}^{n} c_j N_j, N_i \rangle = \langle f, N_i \rangle \quad (2.3.34)$$

or written in matrix form

$$\begin{bmatrix} A(N_0, N_0) & A(N_0, N_1) & \cdots & A(N_0, N_n) \\ A(N_1, N_0) & A(N_1, N_1) & \cdots & A(N_1, N_n) \\ \vdots & \vdots & \vdots & \vdots \\ A(N_n, N_0) & A(N_n, N_1) & \cdots & A(N_n, N_n) \end{bmatrix} \begin{bmatrix} c_0 \\ c_1 \\ \vdots \\ c_n \end{bmatrix} = \begin{bmatrix} \langle f, N_0 \rangle \\ \langle f, N_1 \rangle \\ \vdots \\ \langle f, N_n \rangle \end{bmatrix}$$
$$(2.3.35)$$

To prove the existence and uniqueness of the problem of equations we have to show that this system adheres to the *Lax-Milgram theorem*, as stated in the previous section. That is to say, A must be *symmetric, continuous* and *coercive*.

It is obvious that the coefficient matrix A is symmetric, *i.e.*, $A_{ij} = A_{ji}$. Continuity can be proved using the *Cauchy–Schwarz inequality* which states for any vectors, u, v, of an inner-product space

$$|\langle u, v \rangle| \leqslant \langle u, u \rangle + \langle v, v \rangle \qquad (2.3.36)$$

Applying it to equation 2.3.24

$$|A(u, v)| = |\int_\Omega \nabla u \cdot \nabla v dx| \leqslant \|\nabla u\|_{H^0} \|\|\nabla v\|_{H^0} \qquad (2.3.37)$$

Using that $\|\nabla u\|_{H^0} \leqslant \|u\|_{H^1}$, we can conclude that A is continuous in H^1, i.e.

$$|A(u, v)| \leqslant \|u\|_{H^1} \|v\|_{H^1} \qquad (2.3.38)$$

Coercivity of A in H^1 can be proved using *Friedrichs's first inequality* which states that there is a constant $\alpha > 0$ such that

$$\|\nabla u\|_{H^0}^2 \geqslant \alpha \|u\|_{H^0}^2 \qquad (2.3.39)$$

Using that

$$A(u, u) = \|\nabla u\|_{H^0}^2 = \frac{1}{2}\|\nabla u\|_{H^0}^2 + \frac{1}{2}\|\nabla u\|_{H^0}^2 \qquad (2.3.40)$$

Combining the two we obtain

$$A(u, u) \geqslant \frac{1}{2}\|\nabla u\|_{H^0}^2 + \frac{\alpha}{2}\|u\|_{H^0}^2 \geqslant \frac{\max\{1, \alpha\}}{2}\|u\|_{H^1}^2 \qquad (2.3.41)$$

And thus A is coercive in H^1. These three properties of A lead to the existence of a unique solution to the Galerkin problem provided that f is a smooth continuous function.

Next, we need to prove that the solution is the best approximation to the problem in an appropriate norm, thus showing that

$$\|u - u_h\| \leqslant \|u - v_h\|, \quad \forall v_h \in V_h \qquad (2.3.42)$$

To this end we introduce the *energy norm*

$$\|u\|_\alpha = \sqrt{A(u, u)} \qquad (2.3.43)$$

The energy norm is only well-defined when A is symmetric, i.e, the problem is self-adjoint. We state that finite element solution is the best approximation in the energy norm, i.e

$$\|u - u_h\|_\alpha \leqslant \|u - v_h\|_\alpha, \quad \forall v_h \in V_h \qquad (2.3.44)$$

First we proof that u_h is the projection of u onto V_h through the inner product $A(u,v)$. We have

$$A(u,v) = \langle f, v \rangle, \quad \forall v \in H_0^1 \qquad (2.3.45)$$

Introducing the finite element space $V_h \subset H_0^1$

$$A(u, v_h) = \langle f, v_h \rangle, \quad \forall v_h \in V_h \qquad (2.3.46)$$

The solution can be expressed as a linear combination of the basis of V_h, thus we replace u by u_h

$$A(u_h, v_h) = \langle f, v_h \rangle, \quad \forall v_h \in V_h \qquad (2.3.47)$$

subtracting equation 2.3.47 from equation 2.3.46 we end up with

$$A(u - u_h, v_h) = 0, \quad \forall v_h \in V_h \qquad (2.3.48)$$

Now to show that u_h is the best approximation in V_h

$$\begin{aligned}
\|u - v_h\|_\alpha^2 &= A(u - v_h, u - v_h) & (2.3.49) \\
&= A(u - u_h + u_h - v_h, u - u_h + u_h - v_h) & (2.3.50) \\
&= A(u - u_h, u - u_h + u_h - v_h) + A(u_h - v_h, u - u_h + u_h - v_h) \\
& & (2.3.51) \\
&= \|u - u_h\|_\alpha^2 + \|u_h - v_h\|_\alpha^2 & (2.3.52) \\
&\geqslant \|u - u_h\|_\alpha^2 & (2.3.53)
\end{aligned}$$

Taking the square root on both sides concludes the proof.

$$\|u - u_h\|_\alpha \leqslant \|u - v_h\|_\alpha, \quad \forall v_h \in V_h \qquad (2.3.54)$$

2.4 BOUNDARY CONDITIONS

The previous section dealt with a case of *homogeneous* boundary conditions, conditions which are explicitly imposed on the solution. However, within the finite element method, different types of boundary conditions need to be handled differently.

One form of boundary conditions correspond to the *Dirichlet* boundary conditions which specify the solution, u, on some part of the domain, Ω, and are of the form of

$$u = g \quad \text{on} \quad \delta\Omega \qquad (2.4.1)$$

Homogeneous boundary conditions arise when $g = 0$, these are dealt with easily as we can restrict the test function to $v \in H_0^1$, the family of functions vanishing on the boundary. For *non-homogeneous* conditions, i.e., $g \neq 0$, this condition is not met. The right approach is splitting the solution into $u = u_0 + u_g$ where u_0 is the solution to the problem with homogeneous boundary conditions and u_g corresponds to the

boundary conditions. Using this we can restate the Galerkin problem (equation 2.3.45) as:

find $u_0 \in H_0^1$ such that

$$A(u_0, v) = \langle f, v \rangle - A(u_g, v), \quad \forall v \in H_0^1 \tag{2.4.2}$$

In practice, these conditions can be satisfied by modification of the coefficient matrix, a_{ij} and the load vector b_i. To demonstrate this, consider a 3x3 system, e.g.

$$\begin{bmatrix} a_{00} & a_{01} & a_{02} \\ a_{10} & a_{11} & a_{12} \\ a_{20} & a_{21} & a_{22} \end{bmatrix} \begin{bmatrix} c_0 \\ c_1 \\ c_2 \end{bmatrix} = \begin{bmatrix} b_0 \\ b_1 \\ b_2 \end{bmatrix} \tag{2.4.3}$$

Now let a Dirichlet condition be specified on the domain corresponding to the node $c_i = \alpha_i$. Then the augmented system can be systematically implemented by first subtracting the product of $a_{ij}\alpha_i$ from every f_i. Then assign zero to both row and column $a_{ij} = a_{ji} = 0$ and replace a_{ii} with 1. Finally, set the corresponding r.h.s to $alpha_i$. Repeat for all applicable conditions. For example, letting $c_0 = \alpha_0$ leads to the augmented system

$$\begin{bmatrix} 1 & 0 & 0 \\ 0 & a_{11} & a_{12} \\ 0 & a_{21} & a_{22} \end{bmatrix} \begin{bmatrix} c_0 \\ c_1 \\ c_2 \end{bmatrix} = \begin{bmatrix} \alpha_0 \\ b_1 - a_{10}\alpha_0 \\ b_2 - a_{20}\alpha_0 \end{bmatrix} \tag{2.4.4}$$

And the boundary condition is satisfied.

Another type of boundary conditions is the so-called *natural* conditions. These conditions arise naturally within the weak formulation and present itself in the form of *Neumann* boundary conditions, which have the form

$$\frac{\delta u}{\delta n} = g \text{ on } \delta\Omega \tag{2.4.5}$$

A special variant occurs when $g = 0$, as it is handled 'automatically' within the Galerkin formulation. These are called *homogeneous* Neumann conditions. To see this we restate the result obtained in equation 2.3.19, i.e.

$$\int_\Omega \nabla u \cdot \nabla v dx - \int_{\delta\Omega} \frac{\delta u}{\delta n} v ds = \int_\Omega f v dx \tag{2.4.6}$$

Now instead of finding the solution in a restricted function space, we see immediately that the second term vanishes and is therefore 'automatically' handled trough the Galerkin method.

Non-homogeneous, i.e. $g \neq 0$, Nuemann conditions are explicitly handled trough the weak formulation. Knowing the value for g and substituting it in equation 2.4.6 we end up with

$$\int_\Omega \nabla u \cdot \nabla v dx - \int_{\delta\Omega} g v ds = \int_\Omega f v dx \tag{2.4.7}$$
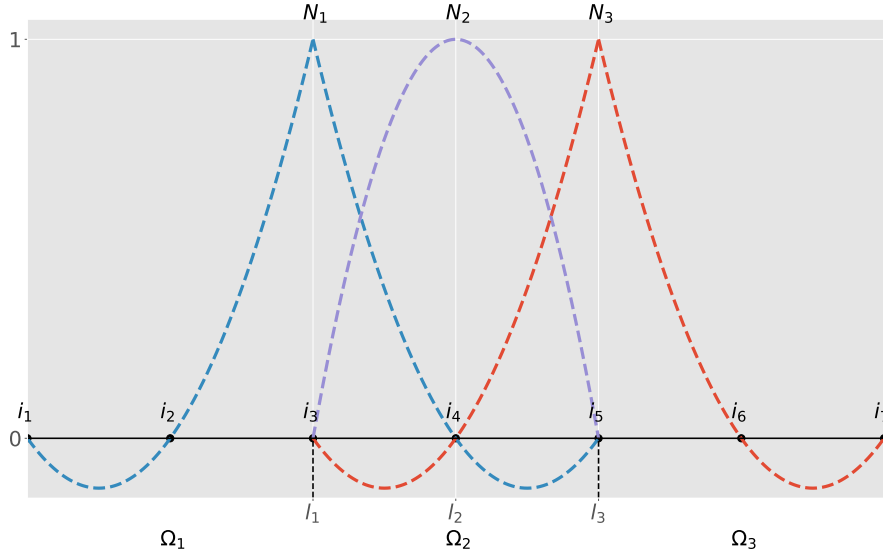
Figure 6: Example of one-dimensional quadratic Lagrangian basis (p=2) with three elements, Ω_i. Only basis functions, N_i, belonging to Ω_2 are shown. Each element has three nodes, i_i denotes a global node number, whereas l_i is a local node number. Note how each basis function takes the value of unity only at its corresponding node. Furthermore, see that the functions still overlap only their own element, and its neighbour.

2.5 CONSTRUCTION OF FINITE ELEMENT SPACES

Up to now, we have seen how to derive a weak formulation and impose different types of boundary conditions. However, we are also interested in the error introduced by a finite element space. In particular, we are interested in the convergence of this error as we refine the mesh, i.e., we are looking for the finite element equivalent of the convergence results we found for the one-dimensional case (see eq. 2.2.64). However, finite element models are rarely one-dimensional. Furthermore, until now, we have restricted ourselves to linear basis functions. The following sections serve to explain higher-order basis functions, as well as elements associated with two- and three-dimensional models. In the end, we find the desired convergence rates. Knowing these convergence rates is of importance, as it will allow us to validate the implementation of our model.

The construction of the basis functions of finite element spaces requires a *mesh*. For the one-dimensional piecewise-linear basis it led to the so-called *hat-functions* (see fig. 3). One method of improving the accuracy of the finite element method is the so-called p-refinement, where we increase the order of the finite element basis. For example, increasing the order to two, or three would lead to a quadratic and cubic piecewise Lagrangian basis respectively. Increasing the order does come at a cost, as increasing the order of the basis increases

the degrees of freedom, or *nodes*, associated with each element. For the one-dimensional piecewise linear basis there were two degrees of freedom, each associated with one end of the element, whereas a quadratic function will have three.

Constructing higher-order basis functions become increasingly more complicated, as more nodes are associated with each element. From the second order and upwards, it is common to refer to nodes with a *global* and *local* number. The global number is a unique number compared to all other nodes in the mesh, whereas a unique local number is given for each node pertaining to an element.

Considering the above, let each local node number, l, in element Ω_e, where e is the number associated with the element, correspond to a global node number i. Then, the construction of the Lagrangian basis $N_i(x)$ of degree p is as follows;

If the node with local number l is located within Ω_e, $N_i(x)$ is the Lagrange polynomial of degree p that is 1 on l and zero at all other nodes in Ω_e. If the node is located on the boundary of Ω_e, $N_i(x)$ is the Lagrange polynomial of degree p that is one over element Ω_e combined with the polynomial of the adjacent element which is also one at the same node. An example of the one-dimensional quadratic Lagrangian basis can be seen in figure 6. Due to the distinct shapes the basis functions produce, they are also known as *shape functions*.

2.5.1   *Two-dimensional Lagrangian basis*

In two dimensions the mesh has to be partitioned into a collection of simple geometric shapes, usually triangles or rectangles. Here we will restrict ourselves to the use of triangular meshes. The most simple two-dimensional Lagrangian finite element space involves the construction of piecewise linear polynomials on a mesh of triangular elements. This is analogous to the one-dimensional hat functions. In addition to *nodes*, triangular elements are also associated *vertices* and *edges*. To construct this basis, consider Ω_e a triangular element associated with domain Ω, with its vertices numbered 1 to 3, where each vertex j has a coordinate (x_j, y_j). Furthermore, the Lagrangian shape functions belonging to vertex j are only non-zero on its index, e.g.

$$N_j(x_i, y_i) = \delta_{j,i}, \quad j, i = 1, 2, 3 \tag{2.5.1}$$

To the end of $N_j(x, y)$ being a piecewise linear polynomial let $N_j(x, y)$ be of the form

$$N_j(x, y) = \alpha_1 + \alpha_2 x + \alpha_3 y, \quad (x, y) \in \Omega_e \tag{2.5.2}$$

Writing the system of equations for the three basis functions N_1, N_2, N_3

$$\begin{bmatrix} 1 & x_1 & y_1 \\ 1 & x_2 & y_2 \\ 1 & x_3 & y_3 \end{bmatrix} \begin{bmatrix} \alpha_1 \\ \alpha_2 \\ \alpha_3 \end{bmatrix} = \begin{bmatrix} N_1 \\ N_2 \\ N_3 \end{bmatrix} \tag{2.5.3}$$
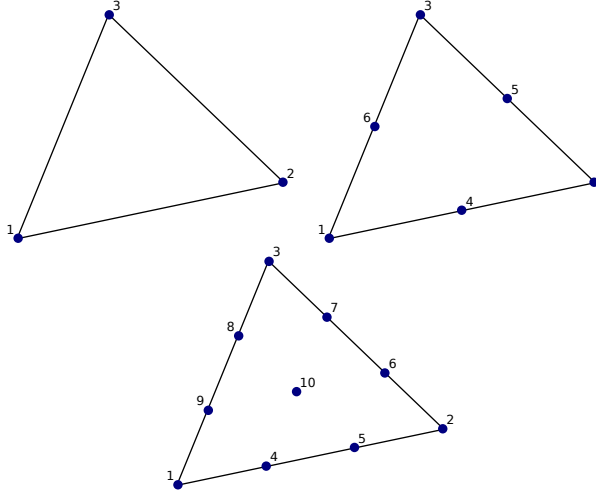
Figure 7: Nodes and their local numbering for triangular elements using Lagrangian basis functions of order one, two and three respectively.

which can be solved for a particular α, using *Cramer's rule* e.g.

$$\alpha_1 = \frac{1}{C} \det \begin{bmatrix} N_1 & x_1 & y_i \\ N_2 & x_2 & y_2 \\ N_3 & x_3 & y_3 \end{bmatrix} \tag{2.5.4}$$

$$= \frac{1}{C}\{(x_2 y_3 - x_3 y_2)N_1 + (x_3 y_1 - x_1 y_3)N_2 + (x_1 y_2 - x_2 y_1)N_3\} \tag{2.5.5}$$

$$\alpha_2 = \frac{1}{C} \det \begin{bmatrix} 1 & N_i & y_i \\ 1 & N_j & y_j \\ 1 & N_k & y_k \end{bmatrix} = \frac{1}{C}\{(y_2 - y_3)N_1 + (y_3 - y_1)N_2 + (y_1 - y_2)N_3\} \tag{2.5.6}$$

$$\alpha_3 = \frac{1}{C} \det \begin{bmatrix} 1 & x_i & N_i \\ 1 & x_j & N_j \\ 1 & x_k & N_k \end{bmatrix} == \frac{1}{C}\{(x_3 - x_2)N_1 + (x_1 - x_3)N_2 + (x_2 - x_1)N_3\} \tag{2.5.7}$$

where

$$C = \det \begin{bmatrix} 1 & x_i & y_i \\ 1 & x_j & y_j \\ 1 & x_k & y_k \end{bmatrix} \tag{2.5.8}$$

With the α_i coefficients determined we can write any linear function over a triangular element as

$$u(x,y) = \frac{1}{C}\{(x_2 y_3 - x_3 y_2 + (y_2 - y_3)x + (x_3 - x_2)y)N_1 \quad (2.5.9)$$

$$+ (x_3 y_1 - x_1 y_3 + (y_3 - y_1)x + (x_1 - x_3)y)N_2 \quad (2.5.10)$$

$$+ (x_1 y_2 - x_2 y_1 + (y_1 - y_2)x + (x_2 - x_1)y)N_3\} \quad (2.5.11)$$

$$= \sum_{j=1}^{3} c_j N_j \quad (2.5.12)$$

To ensure a continuous basis, a node is places at each vertex of the element, see figure 7.

Higher-order basis functions of degree p are constructed similarly. A basis of degree p has

$$n_p = \frac{(p+1)(p+2)}{2} \quad (2.5.13)$$

nodes associated with each element. A second-degree polynomial would result in elements with $n_2 = 6$ nodes and would form a complete polynomial of order 2, e.g.

$$N_j(x,y) = \alpha_1 + \alpha_2 x + \alpha_3 y + \alpha_4 x^2 + \alpha_5 xy + \alpha_6 y^2 \quad (2.5.14)$$

The construction of the triangular element involves placing node points at the vertices, as in the piecewise linear case, with the addition of nodes at the middle of the edges of the triangle (see figure 7. This basis is also continuous due to the dependence of the nodes on adjacent elements. Increasing the order of the polynomial will result in additional nodes placed on the edges, as well as in the center of the triangle. For example, a cubic polynomial would result in 10 nodes, one on each vertex, two on each edge and one in the center of the element. The construction of higher-ordered elements proceeds similarly. However, computations with these elements become increasingly complex. A transformation of the coordinate system can reduce the complexity of the algebraic equations involved, which will be beneficial in our search for the finite element convergence rates.

2.5.2 *The barycentric coordinate system*

In general we want to map an arbitrary triangle from the physical domain (x,y) to a more computational favourable domain. One such transformation is the transformation to the *barycentric*, or *triangular* coordinate system. Every point, $P(x,y)$, inside a triangle with vertices numbered 1, 2, 3 located on (x_i, y_i) and area A_{123}, divides this triangle into three sub-triangles namely P_{12}, P_{13}, P_{23}. Where each sub-triangle has a corresponding area $A_{P12}, A_{P13}, A_{P23}$, as seen in
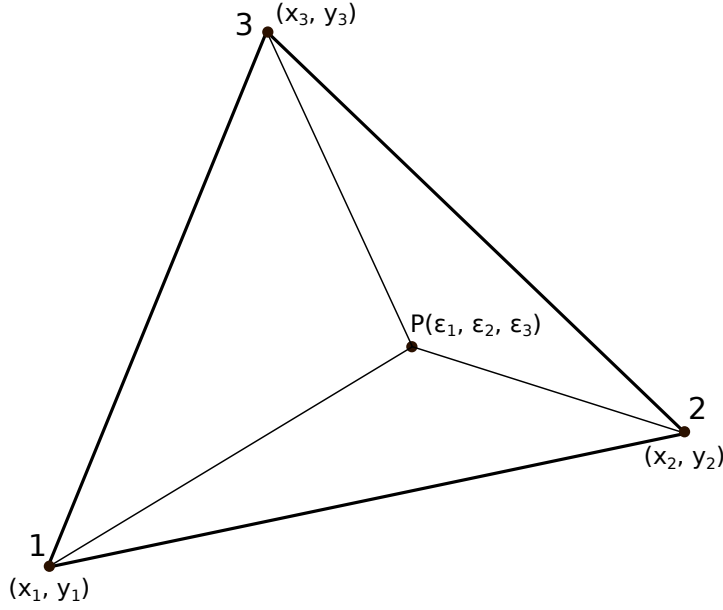
Figure 8: The relation of the Cartesian coordinate system to the Barycen-
tric coordinate system. The point P, divides the triangle into three
sub-triangles. The area of each sub-triangle is used to define the
Barycentric coordinate system.

figure 8. Then the barycentric coordinate ϵ_i is defined as the ratio of
the area of the sub-triangle to the whole, i.e.

$$\epsilon_1 = \frac{A_{P23}}{A_{123}} \tag{2.5.15a}$$

$$\epsilon_2 = \frac{A_{P13}}{A_{123}} \tag{2.5.15b}$$

$$\epsilon_3 = \frac{A_{P12}}{A_{123}} \tag{2.5.15c}$$

However, the area of a triangle with vertices $(x_i, y_i), i = 1, 2, 3$ can be
determined by

$$A_{123} = \frac{1}{2} \det \begin{bmatrix} x_1 & y_1 & 1 \\ x_2 & y_2 & 1 \\ x_3 & y_3 & 1 \end{bmatrix} \tag{2.5.16}$$

substituting this into each equation for ϵ_i will yield the same result
as obtained in equation 2.5.12. For example, ϵ_1 leads to:

$$\frac{A_{P23}}{A_{123}} = \frac{1}{C} \det \begin{bmatrix} 1 & x & y \\ 1 & x_2 & y_2 \\ 1 & x_3 & y_3 \end{bmatrix} \tag{2.5.17}$$

$$= \frac{1}{C}((x_2 y_3 - x_3 y_2) + (y_2 - y_3)x + (x_3 - x_2)y) \tag{2.5.18}$$

Thus the shape functions are obtained by a transformation to barycen-
tric coordinates.
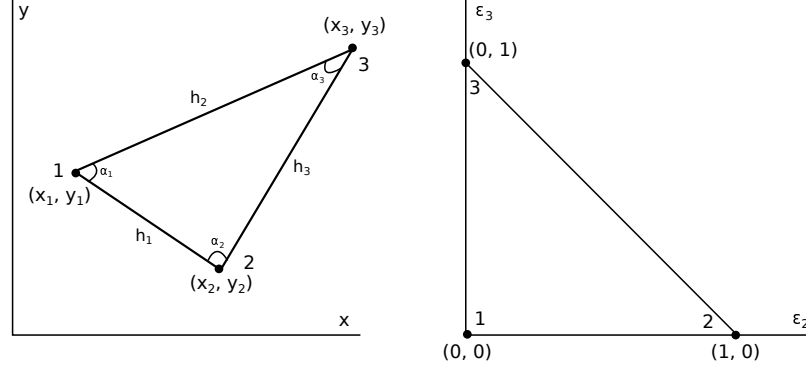
Figure 9: Mapping of an arbitrary triangle in the (x, y) plane to a canonical triangle in the (ϵ_2, ϵ_3)-plane

To transform from barycentric coordinates $(\epsilon_1, \epsilon_2, \epsilon_3)$ to Cartesian coordinates, let (x_i, y_i) be the Cartesian coordinates of vertex i.

$$x = x_1\epsilon_1 + x_2\epsilon_2 + x_3\epsilon_3 \tag{2.5.19a}$$

$$y = y_1\epsilon_1 + y_2\epsilon_2 + y_3\epsilon_3 \tag{2.5.19b}$$

$$1 = \epsilon_1 + \epsilon_2 + \epsilon_3 \tag{2.5.19c}$$

Where the last relation is easily verified, as the summation of the area of each sub-triangle is, of course, the area of the whole triangle. Writing it in matrix form

$$\begin{bmatrix} x_1 & x_2 & x_3 \\ y_1 & y_2 & y_3 \\ 1 & 1 & 1 \end{bmatrix} \begin{bmatrix} \epsilon_1 \\ \epsilon_2 \\ \epsilon_3 \end{bmatrix} = \begin{bmatrix} x \\ y \\ 1 \end{bmatrix} \tag{2.5.20}$$

Reversing the transformation leads to the mapping of the global element to the canonical triangle as pictured in figure 9.

2.5.3 *Three-dimensional Lagrangian basis*

Similarly, a three-dimensional domain can be split up into many different simple geometries. In our case, we limit ourselves to the three-dimensional extension of the triangle, the tetrahedron. Let the vertices be labeled from 1 to 4 having physical coordinates (x_i, y_i, z_i). Again, we want to transform the physical system to the Barycentric coordinate system.

Conceptually similar to the two-dimensional case, a point, $P(x, y, z)$, in a tetrahedron splits it into four sub-tetrahedra, the barycentric coordinate system is defined by

$$\epsilon_1 = \frac{V_{P234}}{V_{1234}} \tag{2.5.21a}$$

$$\epsilon_2 = \frac{V_{P134}}{V_{1234}} \tag{2.5.21b}$$
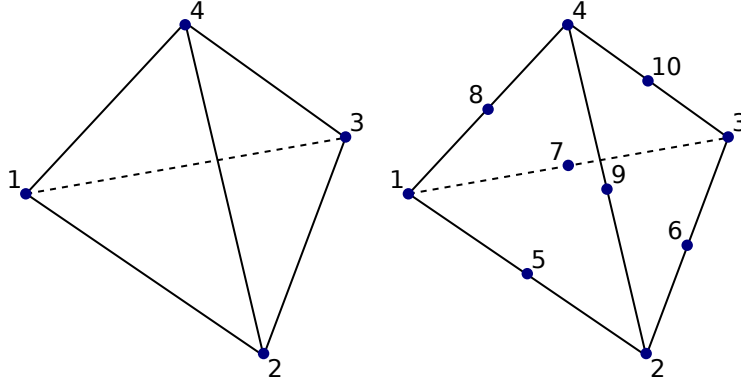
Figure 10: Nodes and their numbering tetrahedral elements using a Lagrangian basis of order one and two respectively.

$$\epsilon_3 = \frac{V_{P124}}{V_{1234}} \tag{2.5.21c}$$

$$\epsilon_4 = \frac{V_{P123}}{V_{1234}} \tag{2.5.21d}$$

where V_{ijkl} is the volume of the tetrahedron with vertices i, j, k, l. Then let the shape functions make up the linear system

$$\begin{bmatrix} 1 & x_1 & y_1 & z_1 \\ 1 & x_2 & y_2 & z_2 \\ 1 & x_3 & y_3 & z_3 \\ 1 & x_4 & y_4 & z_4 \end{bmatrix} \begin{bmatrix} \alpha_1 \\ \alpha_2 \\ \alpha_3 \\ \alpha_4 \end{bmatrix} = \begin{bmatrix} N_1 \\ N_2 \\ N_3 \\ N_4 \end{bmatrix} \tag{2.5.22}$$

Then following the same steps as for the triangular element, we can define the transformation matrix to barycentric coordinates as

$$\begin{bmatrix} x_1 & x_2 & x_3 & x_4 \\ y_1 & y_2 & y_3 & y_4 \\ z_1 & z_2 & z_3 & z_4 \\ 1 & 1 & 1 & 1 \end{bmatrix} \begin{bmatrix} \epsilon_1 \\ \epsilon_2 \\ \epsilon_3 \\ \epsilon_4 \end{bmatrix} = \begin{bmatrix} x \\ y \\ z \\ 1 \end{bmatrix} \tag{2.5.23}$$

Construction of higher-degree polynomials on tetrahedra involves the placement of nodes at the edges, faces and the interior of the tetrahedral. In fact to construct a complete polynomial of order p on a tetrahedral we need

$$n_p = \frac{(p+1)(p+2)(p+3)}{6} \tag{2.5.24}$$

nodes. Placement of nodes of different degrees can be seen in figure 10.

2.5.4 *Interpolation error of finite elements*

In this section, we will focus on the interpolation error on triangular elements. For the one-dimensional case, we found that the inter-

polation error was quadratically proportional to the element size of the mesh (eq. 2.2.64). However, as we will see, in two- and three-dimensions the elements cannot be too distorted, meaning that the angles present in the element cannot be too small or large.

Considering the transformation of a triangular element e to its barycentric coordinates. For this we reconsider equations 2.5.19 and rewrite

$$x = x_1 + (x_2 - x_1)\tilde{x} + (x_3 - x_1)\tilde{y} \qquad (2.5.25a)$$

$$y = y_1 + (y_2 - y_1)\tilde{x} + (y_3 - y_1)\tilde{y} \qquad (2.5.25b)$$

where we substituted $\epsilon_2 = \tilde{x}, \epsilon_3 = \tilde{y}$ for a more common notation in the context of transformations.

The Jacobian associated with this element transformation is

$$J_{el} = \begin{bmatrix} \frac{\delta x}{\delta \tilde{x}} & \frac{\delta x}{\delta \tilde{y}} \\ \frac{\delta y}{\delta \tilde{x}} & \frac{\delta y}{\delta \tilde{y}} \end{bmatrix} \qquad (2.5.26)$$

and its determinant

$$D_{el} = (x_2 - x_1)(y_3 - y_1) - (x_3 - x_1)(y_2 - y_1) \qquad (2.5.27)$$

$$= 2A_{el} \qquad (2.5.28)$$

where A_{el} is the area of the triangular element.

Denote the smallest angle of this element α_{el} and its longest edge h_{el}, then

$$\frac{h_{el}^2}{2} \sin \alpha_{el} \leqslant D_{el} \leqslant h_{el}^2 \sin \alpha_{el} \qquad (2.5.29)$$

To see this, reconsider the arbitrary triangle depicted in figure 9, which shows an element with $\alpha_{el} = \alpha_3$ and $h_{el} = h_2$. Then we can rewrite the Jacobian determinant as

$$D_{el} = h_2 h_3 \sin \alpha_3 \qquad (2.5.30)$$

Using the law of sines, i.e.

$$\frac{\sin \alpha_1}{h_1} = \frac{\sin \alpha_2}{h_2} = \frac{\sin \alpha_3}{h_3} \qquad (2.5.31)$$

we have $h_1 \leqslant h_3 \leqslant h_2$. substituting this in equation 2.5.30, we end up with the r.h.s of equation 2.5.29. The l.h.s. follows from the triangle inequality, i.e., $h_2 < h_1 + h_2$, meaning that either h_1 or $h_3 > h_2/2$.

Next, let Ω_{el} be the domain of the element and Ω_{can} the domain of the canonical element. Furthermore, let $\theta(x,y) \in H^d(\Omega_{el})$ and $\tilde{\theta}(\tilde{x}, \tilde{y}) \in H^d(\Omega_{can})$ such that $\theta(x,y) = \tilde{\theta}(\tilde{x}, \tilde{y})$. Then there exists constants c_0, c_1, such that

$$c_0 h_{el}^{d-1} (\sin \alpha_{el})^{d-\frac{1}{2}} |\theta|_{H^d(\Omega_{el})} \leqslant |\tilde{\theta}|_{H^d(\Omega_{ca})} \leqslant c_1 h_{el}^{d-1} (\sin \alpha_{el})^{d-\frac{1}{2}} |\theta|_{H^d(\Omega_{el})} \qquad (2.5.32)$$

Here we will show the proof for the case $d = 0$. By definition of the transformation we have

$$\int_{\Omega_{el}} \theta^2 \, dx \, dy = D_{el} \int_{\Omega_{ca}} \tilde{\theta}^2 \, d\tilde{x} \, d\tilde{y} \qquad (2.5.33)$$

Using the definition of the H^0 norm (equation 2.3.15)

$$\|\theta\|^2_{H^0(\Omega_{el})} = D_{el} \|\tilde{\theta}\|^2_{H^0(\Omega_{ca})} \qquad (2.5.34)$$

using equation 2.5.29, dividing by D_{el}, and taking the square root, we end up with equation 2.5.32 for the case $d = 0$, i.e.

$$\frac{\|\theta\|_{H^0(\Omega_{el})}}{h_{el}\sqrt{2\sin\alpha_{el}}} \leqslant \|\tilde{\theta}\|_{H^0(\Omega_{ca})} \leqslant \frac{\|\theta\|_{H^0(\Omega_{el})}}{h_{el}\sqrt{\sin\alpha_{el}}} \qquad (2.5.35)$$

with $c_1 = 1/\sqrt{2}$ and $c_2 = 1$.

The proof for higher values of d involve the use of the chain rule and the respective H^d semi-norm, and can be found in [15].

To proof the convergence rates for the finite element, we will, as in the case of the one-dimensional approximation, find the error in an upper bound given by the interpolating polynomial on the canonical element

$$u_i(\tilde{x}, \tilde{y}) = \sum_{j=1}^{n} N_j(\tilde{x}, \tilde{y}) u(\tilde{x}, \tilde{y}) \qquad (2.5.36)$$

Furthermore, we need an application of the *Bramble-Hilbert Lemma* given by [21], which states

Let $u(\tilde{x}, \tilde{y})$ be a polynomial of degree p such that the interpolant, u_i of degree p is exact. Then, there exists a constant $C > 0$ such that

$$|u - u_i|_{H^d(\Omega_{ca})} \leqslant C|u|_{H^{p+1}(\Omega_{ca})} \qquad (2.5.37)$$

Using all of the results above we can state the following:

Let Ω be a domain consisting of n triangular elements, $\Omega_{el}, e = 1, \cdots, n$. Let h_{el} be the largest element edge and $alpha_{el}$ the smallest angle of the element. Let $u(\tilde{x}, \tilde{y})$ be a polynomial of degree p such that the interpolant, u_i of degree p is exact. Then there exists a constant $C > 0$, independent of the mesh and $u \in H^{p+1}$, such that

$$|u - u_i|_{H^d} \leqslant \frac{Ch_{el}^{p-d+1}}{\sin^d \alpha_{el}} |u|_{H^{p+1}} \qquad (2.5.38)$$

The proof follows by first substituting $u - u_i$ in the l.h.s of equation 2.5.32

$$|u - u_i|^2_{H^d(\Omega_{el})} \leqslant \frac{1}{c_0} h_{el}^{2-2d} \sin^{1-2d} \alpha_{el} |\tilde{u} - \tilde{u}_i|^2_{H^d(\Omega_{ca})} \qquad (2.5.39)$$

Following the use of equation 2.5.37

$$|u - u_i|^2_{H^d(\Omega_{el})} \leqslant \frac{1}{c_0} h_{el}^{2-2d} \sin^{1-2d} \alpha_{el} C |\tilde{u}|^2_{H^{p+1}(\Omega_{ca})} \qquad (2.5.40)$$

And using the r.h.s of equation 2.5.32

$$|u - u_i|^2_{H^d(\Omega_{el})} \leqslant \frac{1}{c_0} h_{el}^{2-2d} \sin^{1-2d} \alpha_{el} C c_1 H_{el}^{2d} \sin^{-1} \alpha_{el} |u|^2_{H^{p+1}(\Omega_{el})}$$

(2.5.41)

Combining all the constants and taking the square root yields

$$|u - u_i|_{H^d(\Omega_{el})} \leqslant \frac{C h_{el}^{p-d+1}}{\sin^d \alpha_{el}} |u|_{H^{p+1}(\Omega_{el})}$$

(2.5.42)

Summing over all elements yields the final result.

A more general result is obtained by considering a *uniform* mesh. A mesh is said to be *uniform* if all element angles are bounded away from zero and π, and all aspect ratios are bounded away from zero. In this case, there is no dependence on the smallest angle, and the result of equation 2.5.42 reduces to

$$|u - u_i|_{H^d} \leqslant C h^{p-d+1} |u|_{H^{p+1}}$$

(2.5.43)

Now we know the convergence rates associated with the finite element method. For example, using linear basis functions (p=1), and measuring the error in the $H^0 \equiv L^2$-norm (d=0), yields

$$|u - u_i|_{L^2} \leqslant C h^2 |u|_{H^2}$$

(2.5.44)

which is quadratically convergent, as our original one-dimensional convergence result in equation 2.2.64.

This result gives us an expectation of how the error behaves w.r.t. the number of mesh element size, and is also known as the *a-priori* error estimation. Furthermore, as alluded to, the convergence rates will be used to test the implementation of the solvers. As a wrong implementation will not retrieve the correct convergence rates.

2.6 SOLVING LINEAR SYSTEMS

Up to now, we have seen how to set up the weak formulation, and how the error of the finite element converges. In section 2.3.4 we saw that the weak formulation reduces to a system of equation which are either *linear* or *non-linear*. In this section, we will show, conceptually, how these kinds of systems can be solved. Beginning with the simplest case of a linear system, i.e.

$$Ax = b$$

(2.6.1)

Such a system can be solved by different solvers which fall into two categories, *direct* solvers and *iterative* solvers.

Direct solvers rely on the direct elimination of equations. The most popular methods involve a *LU*-decomposition, where the matrix A is split in an upper, U, and lower, L triangular matrix i.e.

$$A = LU$$

(2.6.2)

and thus by substitution in eq. 2.6.1

$$LUx = b \tag{2.6.3}$$

which can be solved in two steps, first by substitution of $Y = Ux$ and solving for Y

$$LY = b \tag{2.6.4}$$

and then by back-substitution we can solve for x

$$Ux = Y \tag{2.6.5}$$

These methods solve the system of equations exactly and can handle quite ill-imposed problems. However, the main drawback of these direct methods is that the storage of requirements of L and U can be extremely high. In particular, for bigger systems, the computational memory can easily exceed that of a normal desktop computer.

The other type of solvers are the iterative solvers. These try to solve the linear system by increasingly finding better approximations to x. To demonstrate such an iterative concept, let $x^{(k)}$ be the current estimation and $x^{(k+1)}$ the next. If $x^{(k)}$ is close to x then $b - Ax^{(k)}$ is small. Thus an iterative process can be written as

$$x^{(k+1)} = x^{(k)} + Q^{-1}(b - Ax^{(k)}) \tag{2.6.6}$$

Where Q is known as the preconditioner. The goal of the preconditioner is to augment the system to one that is computational easier to solve. The above expression can be rewritten to

$$Qx^{(k+1)} = Nx^{(k)} + b, \quad N = Q - A \tag{2.6.7}$$

Furthermore if $x^{(k+1)}$ converges to x we have

$$Qx = Nx + b \tag{2.6.8a}$$

$$Ax = (Q - N)x = b \tag{2.6.8b}$$

$A = Q - N$ is also known as the splitting of A. The easiest method to implement is known as the *Jacobi* method. The *Jacobi* method has a splitting of $A = D_A + L_A + U_A$ where $D_A = \text{diag}(A)$, L_A is the lower triangular and U_A the upper triangular of A. Then the iterative process reads for each node i,

$$x_i^{(k+1)} = \frac{1}{a_{ii}}(b_i - \sum_{j \neq i}^{n} a_{ij}x_j^{(k)})$$

or in matrix form

$$x^{k+1} = D_A^{-1}(L_A + U_A)x^k + D_A^{-1}b \tag{2.6.9}$$

Now we demonstrate the Jacobi method. Consider the following system of equations

$$8x_1 + x_2 + x_3 = 8 \tag{2.6.10a}$$

$$x_1 + 2x_2 + 2x_3 = 10 \tag{2.6.10b}$$

$$x_1 + x_2 + 3x_3 = 3 \tag{2.6.10c}$$

which can be rewritten as

$$x_1 = \frac{8 - x_2 - x_3}{8} \tag{2.6.11a}$$

$$x_2 = \frac{10 - x_1 - 2x_3}{2} \tag{2.6.11b}$$

$$x_3 = \frac{3 - x_1 - x_2}{3} \tag{2.6.11c}$$

Then, using an initial guess of $x^{(0)} = \{x_1 = 0, x_2 = 0, x_3 = 0\}$, we can find a better approximation using the above equations. Substituting the initial guess in the above expression leads to, new, improved values of

$$x^{(1)} = \{x_1 = 1, \quad x_2 = 5, \quad x_3 = 1\} \tag{2.6.12}$$

Then, the process can be repeated by substituting the values of $x^{(1)}$ into equation 2.6.11. The iteration scheme is stopped when the difference between iterations is less than a specified tolerance, i.e. $x^{(k)} - x^{(k-1)} < \tau_{tol}$. Using a tolerance of $\tau_{tol} = 1 \times 10^{-10}$ for the above example leads to a converged solution after 77 iterations

$$x^{(77)} = \{x_1 = 0.4, \quad x_2 = 5.9, \quad x_3 = -1.1\} \tag{2.6.13}$$

2.7 SOLVING TIME-DEPENDENT AND NONLINEAR SYSTEMS

During RF ablation heat is generated and spread throughout the tissue. As such, the involved equations will include a time dependence. In this section, we show the two most basic methods of dealing with a time derivative, the (explicit) *forward Euler* and (implicit) *backward Euler* methods.

Time discretization models are divided into explicit and implicit methods. Explicit methods are formulations where the solution is only dependent on known functions. Implicit methods solve equations involving the known and unknown parameters. For the next section let us consider the model problem

$$\frac{\delta u(t)}{\delta t} = f(t, u) \tag{2.7.1}$$

Then the *forward Euler* method uses the value at the unknown time step, $u^{(n+1)}$ in terms of the value at the known time step $u^{(u)}$ over the time interval Δt as

$$\frac{u^{(n+1)} - u^{(n)}}{\Delta t} = f(t, u^{(n)}) \tag{2.7.2}$$

which is a linear equation for $u^{(n+1)}$ and can be written as

$$u^{(n+1)} = u^{(n)} + \Delta t f(t, u^{(n)}) \tag{2.7.3}$$

However, this discretization in time introduces some error ϵ, the local truncation error. It is defined as the error introduced at a time step, provided that the previous time step is known, i.e.

$$\epsilon^{(n+1)} = u^{(n+1)} - u^{(n)} + \Delta t f(t, u^{(n)}) \qquad (2.7.4)$$

As we are interested in the order of this error we use the Taylor expansion of $u^{(n+1)}$ around $u(t)$

$$u^{(n+1)} = u(t) + \Delta t u'(t) + \frac{(\Delta t)^2}{2} + u''(t) + \frac{(\Delta t)^3}{6} u'''(t) + \cdots \qquad (2.7.5)$$

$$= u_n + \Delta t f(t, u(t)) + \frac{(\Delta t)^2}{2} u''(t) + O(h^3) \qquad (2.7.6)$$

Substituting the above expression into equation 2.7.4 yields

$$\epsilon^{(n+1)} = \frac{(\Delta t)^2}{2} u''(t) + O((\Delta t)^3) \qquad (2.7.7)$$

where we used the big O-notation to indicate the order of the remaining terms.

The first term dictates the order of the truncation error, and it is therefore said that the local truncation error of the forward Euler method is of second order.

The global truncation error, E, is the error at a time step due to all the previous errors and is proportional to one order lower than the local truncation error [22], i.e.

$$E = O((\Delta t)^{p-1}) \qquad (2.7.8)$$

where p denotes the order of the local truncation error.

The implicit version is known as the *backward Euler* method e.g.

$$\frac{u^{(n+1)} - u^{(n)}}{\Delta t} = f(t, u^{(n+1)}) \qquad (2.7.9)$$

and its local truncation error is

$$\epsilon^{(n+1)} = u^{(n+1)} - u^{(n)} - \Delta t f(t, u^{(n+1)}) \qquad (2.7.10)$$

Now we expand the term $u^{(n)}$ around $u(t)$

$$u^{(n)} = u^{(n+1)} - \Delta t f(t, u(t)) + \frac{(\Delta t)^2}{2} u''(t) - O((\Delta t)^3) \qquad (2.7.11)$$

upon substituting the above expression into equation 2.7.10 we get

$$\epsilon^{(n+1)} = -\frac{(\Delta t)^2}{2} u''(t) + O((\Delta t)^3) \qquad (2.7.12)$$

Moreover, the implicit and explicit Euler methods have the same local truncation error. The main advantage of the implicit method is that it is known to be unconditionally stable, that is to say, the time step can be made arbitrarily large. However, the drawback is that equation 2.7.9 leads to a nonlinear system of equations for the unknown $u^{(n+1)}$ when material properties are taken into account. In the next section we discuss two different methods of solving nonlinear systems, the *Picard*-iteration, and *Newton's method.*

2.7.1 *Picard Iteration*

Consider an implicit Euler problem formulated as follows

$$\frac{u^{(n+1)} - u^{(n)}}{\Delta t} = u^{(n+1)}(1 - u^{(n+1)}) \qquad (2.7.13)$$

where, again, u^n is the known solution, $u^{(n+1)}$ the desired solution and Δt the time interval.

This can be rewritten as

$$F(u) = \Delta t(u^{(n+1)})^2 + (1 - \Delta t)u^{(n+1)} - u^{(n)} = 0 \qquad (2.7.14)$$

Such a nonlinear equation can be solved by *linearization*. Let $\tilde{u}$ be a known approximation of $u^{(n+1)}$ then the quadratic term can be linearized by

$$F(u) \approx \tilde{F}(u) = \Delta t \tilde{u} u^{(n+1)} + (1 - \Delta t)u^{(n+1)} - u^{(n)} = 0 \qquad (2.7.15)$$

which is again a linear equation for the unknown u^n. The approximation can then be improved by repeatedly solving for u, where each iteration we set $\tilde{u} = u$. This is known as a *Picard* iteration. Since we have to iterate in time and in the nonlinearities, let n denote the time iteration and k the *Picard* iteration, we write

$$\Delta t u^{(n+1,k)} u^{(n+1,k+1)} + (1 - \Delta t)u^{(n+1,k+1)} - u^{(n)} = 0 \qquad (2.7.16)$$

Where the first Picard iteration can be taken as the solution from the previous time step, i.e. $u^{(n+1,0)} = u^{(n)}$. As the Picard iterations lead to ever better approximations, a stopping criterion is employed which has the form

$$|u^{(n+1,k+1)} - u^{(n+1,k)}| \leqslant \tau_u \qquad (2.7.17)$$

where τ_u is a set tolerance parameter, or when the residual is below a tolerance, τ_r

$$|F(u)| = |\Delta t \tilde{u} u + (1 - \Delta t)u^n - u^{n-1}| \leqslant \tau_r \qquad (2.7.18)$$

2.7.2 *Newton's method*

The second method to deal with non-linearities is known as *Newton's method*. This method linearizes the nonlinear problem by expanding $F(u)$ by its Taylor series and truncating higher-order terms.

Consider the Taylor series of $x = x_0 + \epsilon$

$$F(x_0 + \epsilon) = F(x_0) + F^{'}(x_0)\epsilon + \frac{1}{2}F^{''}(x_0)\epsilon^2 \qquad (2.7.19)$$

$$\approx F(x_0) + F^{'}(x_0)\epsilon \qquad (2.7.20)$$

The above expression can be used to iteratively obtain a better approximation of the root by considering an initial guess x_0. Solving for $\epsilon = \epsilon_0$

$$\epsilon_0 = \frac{F(x_0)}{F'(x_0)} \tag{2.7.21}$$

Subsequently we let $x_1 = x_0 + \epsilon_0$ to obtain a better estimation. Repeating this process we end up with

$$\epsilon_n = -\frac{F(x_n)}{F'(x_n)} \tag{2.7.22}$$

and

$$x_{n+1} = x_n - \frac{F(x_n)}{F'(x_n)} \tag{2.7.23}$$

To see the advantage of the Newton method consider that the Newton iteration $x^{(k+1)}$ converges to $\tilde{x}$ and $F'(\tilde{x}) \neq 0$ such that

$$x^{(k)} = \tilde{x} + \epsilon_k \tag{2.7.24}$$

where ϵ_k is the error after the kth iteration. Then using the Taylor series around $F(x^{(k)})$ around the point $\tilde{x}$ gives

$$F(x^{(k)}) = F(\tilde{x}) + F'(\tilde{x})\epsilon_k + \frac{1}{2}F''(\tilde{x})\epsilon_k^2 = 0 \tag{2.7.25}$$

Dividing by $F'(\tilde{x})$, rearranging the terms gives and using equation 2.7.23

$$\epsilon^{(k+1)} = \frac{-F''(\tilde{x})}{2F'(\tilde{x})}\epsilon_k^2 \tag{2.7.26}$$

Taking the absolute value on both sides gives

$$|\epsilon^{(k+1)}| = \frac{|F''(\tilde{x})|}{2|F'(\tilde{x})|}\epsilon_k^2 \tag{2.7.27}$$

Which shows that the Newton method has a quadratic convergence rate. The Newton method also adheres to the same stopping criteria as the Picard method, e.g., equation 2.7.17, and 2.7.18.

2.7.3 *Nonlinear System of equations*

Nonlinear systems of equations do not only arise from implicit time stepping schemes.

For example, consider the nonlinear model problem

$$-\nabla \cdot (k(u)\nabla u) = f(u), \quad \in \Omega \tag{2.7.28a}$$

$$u = 0, \quad \text{on} \quad \delta\Omega \tag{2.7.28b}$$

Multiplying by a test function, $v \in H_0^1$ and using Green's formula we arrive at the weak formulation which states: find $u \in H_0^1$ such that:

$$\int_\Omega k(u)\nabla u \cdot \nabla v dx = \int_\Omega f(u)v dx, \quad \forall v \in H_0^1 \qquad (2.7.29)$$

The nonlinear system of equations is obtained by replacing H_0^1 by the finite element subspace, $V_h \subset H_0^1$ i.e.

find $u_h \in V_h$ such that

$$\langle k(u_h)\nabla u_h, \nabla v \rangle = \langle f(u_h), v \rangle, \quad \forall v \in V_h \qquad (2.7.30)$$

and subsequently replacing u_h by the linear combination of its basis functions

$$u_h = \sum_{j=1}^n \varepsilon_j N_j \qquad (2.7.31)$$

we end up with

$$A(\varepsilon)\varepsilon = b(\varepsilon) \qquad (2.7.32)$$

A nonlinear system of equations.

We can solve this by linearization by the Picard method. Where we repeatedly solve for ε

$$A(\tilde{\varepsilon})\varepsilon = b(\tilde{\varepsilon}) \qquad (2.7.33)$$

Until a convergence criteria is met.

Alternatively, the second option, we use Newton's method where we first rewrite equation 2.7.32 to

$$F(\varepsilon) = A(\varepsilon)\varepsilon - b(\varepsilon) = 0 \qquad (2.7.34)$$

Then using the Taylor expansion on $F(\varepsilon)$ around a known $\tilde{\varepsilon}$ and truncating non-linear terms

$$F(\varepsilon) \approx F(\tilde{\varepsilon}) + J(\tilde{\varepsilon}) \cdot (\varepsilon - \tilde{\varepsilon}) \qquad (2.7.35)$$

Where J is the Jacobian-matrix. Which, can be written in as a linear system.

2.8   COMPUTATIONAL FRAMEWORK

Much of the previously discussed methods can be generalized and therefore automated. There exist many different software packages which handle many of the tedious work of setting up a FEM problem efficiently, such as efficient storage of matrices, efficient assembly of these matrices and even using different solving techniques. To this end, the *FEniCS* [23] project has been chosen as the framework. Fenics is an open source computing platform for solving PDEs. Thanks to its high-level Python interface combined with a C++ backbone, it allows

for ease of programming while keeping the speed of operations associated with C++. Furthermore, models written with Fenics are easily transformed in parallel executable programs, allowing for a decrease in computation time on modern desktops. Furthermore, Fenics strives to make written code to be as close as possible to the original mathematical formulation. For example, the problem described by 2.3.45 is implemented as follows:

```python
''' Implementation of the weak formulation of Poisson's
    equation. A mesh has been defined previously in the code and
    is denoted here as mesh.
'''

# Define a Lagrangian function space on the mesh of degree = 2.
    (CG stands for Continuous Galerkin)
V = FunctionSpace('CG', mesh, 2)

# Define weak formulation
u = TrialFunction(V)
v = TestFunction(V)
f = Constant(0.)

a = inner(grad(u), grad(v)) * dx
L = inner(f, v) * dx

u = Function(V)
solve(a == L, u)
```

MODELING OF RADIOFREQUENCY ABLATION

In general, the modeling of a finite element model follows the following steps:

1. Simplification of the physical situation

2. Generation of a suitable mesh

3. Determining the mathematical equations involved and determining the weak formulations

4. Determining of the boundary conditions

5. Determination of the physical material characteristics involved

3.1 SIMPLIFICATION OF THE MODEL

One of the first steps in constructing a model of a physical phenomenon is finding and applying adequate simplifications. In the present case, this includes finding axes of symmetry, which will, in turn, allow for the simplification of a three-dimensional model into a two-dimensional axisymmetric model. Further geometric simplifications are made when only considering tissues which are relevant for the treatment, in favor of microscopic structures as epithelia, basal laminas, glands, and nerves [24], but including the probe, tumor and surrounding tissues such as liver, cortical bone, trabecular bone or muscle. An axisymmetric model is then achieved by simplifying the tissues to be either spherical or cylindrical. An example of this can be seen in figure 11, where a three-dimensional cylindrical model is reduced to a two-dimensional model by exploiting its axis of symmetry. The creation and subsequent meshing of models which consists of simple geometric shapes, such as in figure 11, can be performed by various software packages. However, the creation of a patient-specific mesh is not straightforward. We will address this topic in section 5.3.1, where we will use patient-specific meshes for simulations.

3.2 EQUATIONS GOVERNING RADIO FREQUENCY ABLATION

Now that we have a mesh be it three- or two-dimensional, we solve the appropriate equations that model the RFA process. The RFA process is a transient one, meaning that the involved equations need to be solved in time-steps. During each time-step, model parameters are adjusted to reflect the current state of the model. For example,
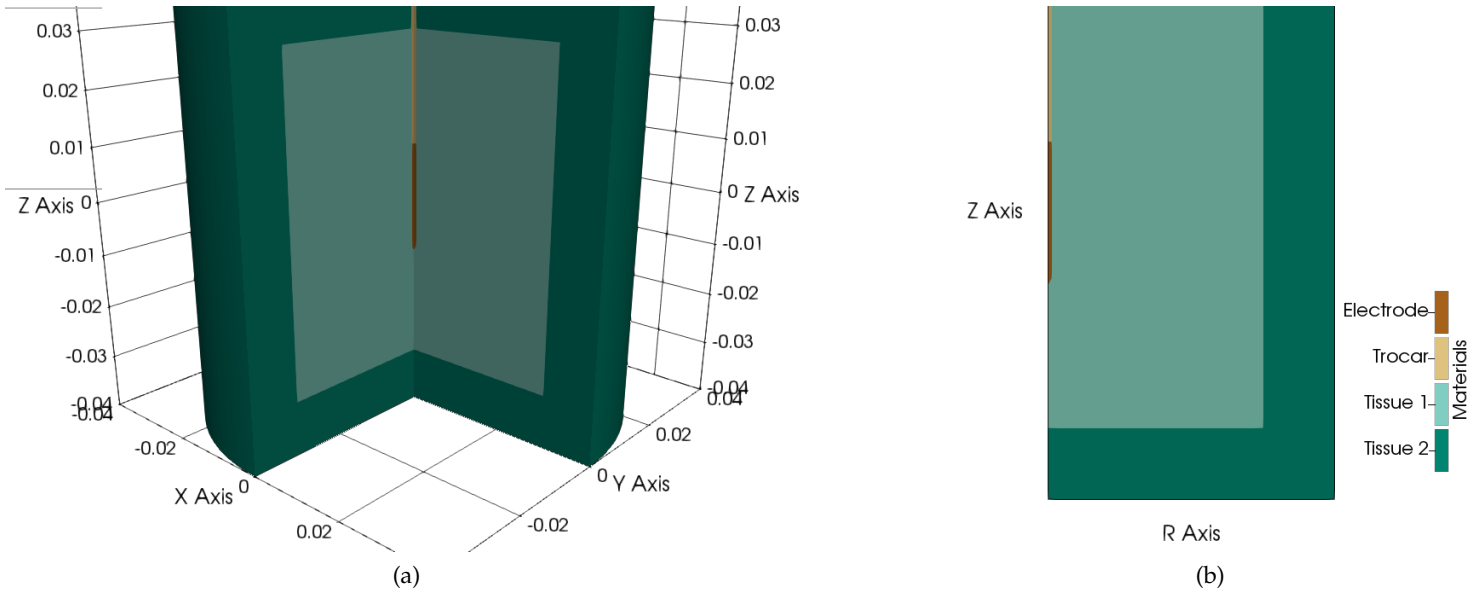
Figure 11: An example of a three-dimensional cylindrical volume which is reduced to a two-dimensional model by exploiting the symmetry axis (z-axis). (a) The three-dimensional model. (b) The axisymmetric model

the electrode-voltage can be adjusted during RFA to reach a certain temperature. Also, most material properties change as a function of temperature, so must be updated accordingly.

Programming-wise the equations are solved in a loop until the simulation has been run for the desired treatment time. This loop is the heart of the model and is schematically represented by figure 12.

The schematic can be roughly divided into four steps. First, the root mean square (r.m.s.) voltage must be calculated. This is done in the first section of *Power control*, where three types of control are listed. Second, in the *Electric potential* block the source-term can be calculated using the supplied voltage. However, the electric conductivity of tissue is temperature dependent [25] and must be updated accordingly. Further, if the voltage is regulated through an impedance-control, the power and resistance are calculated. Third, the *Pennes bioheat*-block is used to calculate the resulting temperature. This process also involves the density, specific heat and thermal conductivity of the involved materials which are temperature dependent Lastly, the tissue damage is calculated according to one of the *cell death* models. Furthermore, there is feedback from the cell death model to the Pennes' bioheat equation as the extent of tissue damage, or cell death, affects cooling abilities of the tissue [26]. In the next section we will go over these blocks in detail, using figure 12 as a reference.
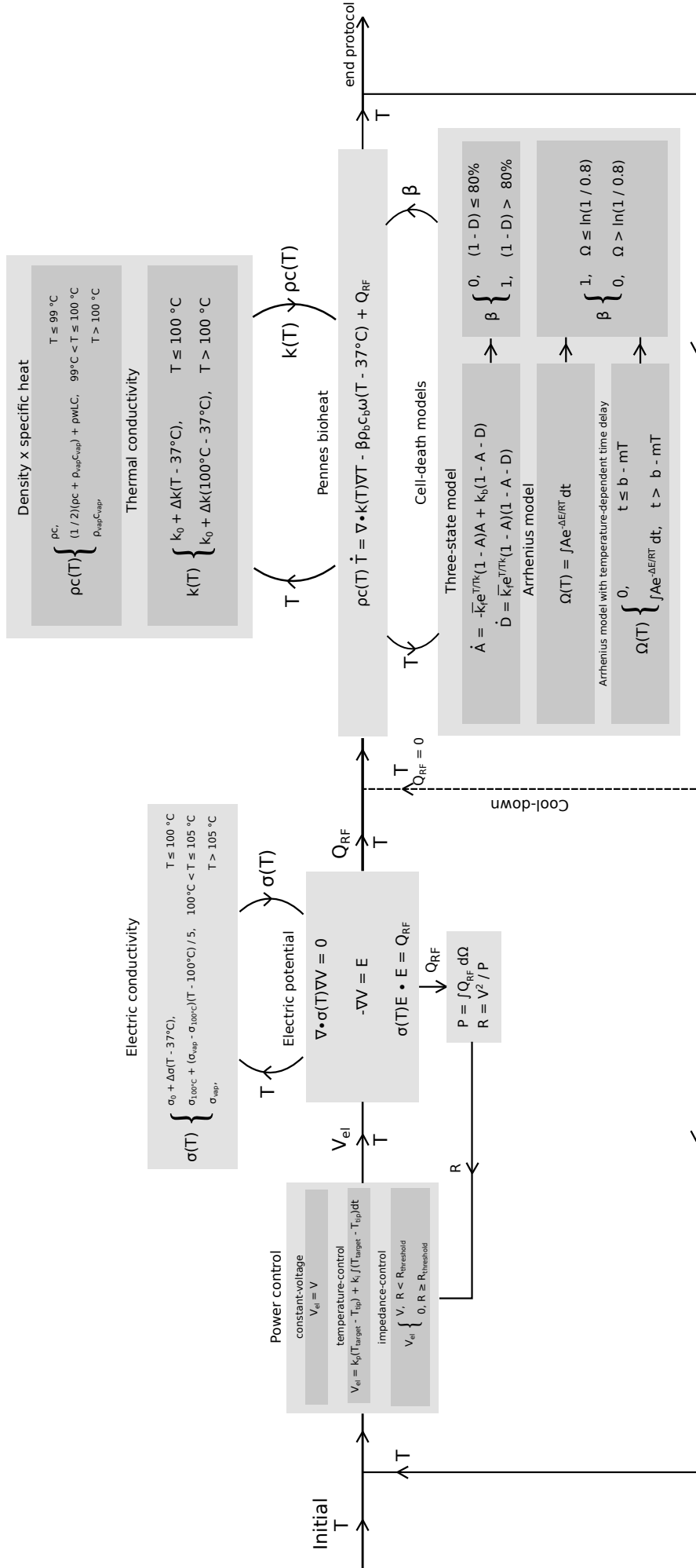
Figure 12: A simplified schematic of the core modules of the model.

3.3   POWER CONTROL

In RF ablation, the heat source arises from the current between the electrode and ground pad, known as *Joule-*, or *Resistive-*heating. The intensity of the source term can be regulated by adjusting the applied voltage to the electrode. By changing the r.m.s. voltage, one has control over the temperatures reached within the tissue. To this end, three types of control for the voltage have been implemented.

3.3.1   *Constant voltage*

The first is constant voltage control. The voltage is set to a constant value throughout the RF ablation. This method is not clinically relevant, as a method of control over the reached temperature within the tissue is always desired. However, this form of control has been included for testing purposes and completeness sake.

3.3.2   *PI-controller*

A second control is a temperature-based control, a type of control which is used in the clinical setting [11]. Here the voltage is regulated such that a pre-defined temperature at the tip of the electrode is reached, and subsequently maintained. The tip of the electrode contains a thermocouple through which the temperature can be measured. Although the internal workings of these devices are not publicly available, such a type of control can be modeled by utilizing a *PI-*controller [27]. This control forms a closed feedback loop, where the input is the temperature of the tip at time t and the output an r.m.s. voltage at time t of V. More specifically the output is given by

$$V(t) = k_p(T_{target} - T_t(t)) + k_i \int_0^t (T_{target} - T_t(t))dt \qquad (3.3.1)$$

where $V(t)$ the voltage output at time t, T_{target} is the desired target temperature (K), T_t is the tip temperature (K) at time t, k_p is the error, or difference, proportionality constant and k_i the integral proportionality constant. The first term of equation 3.3.1 ensures a voltage proportional to k_p when $T_{target} \neq T_t$. The second term is included to account for the differences in the past. When T_{target} is met, both term stops to grow. However, whereas the first term will be reduced to zero, the second, in general, will not. This ensures that the target temperature is maintained.

Values of k_p and k_i must then be found such that similar behavior is found to the *in-vivo* situation. Although this is model dependent, a good agreement has been found by setting $k_p = 1.15$ and $k_i = 0.06$ [28]. The effect of adjusting these PI-parameters can be seen in figure
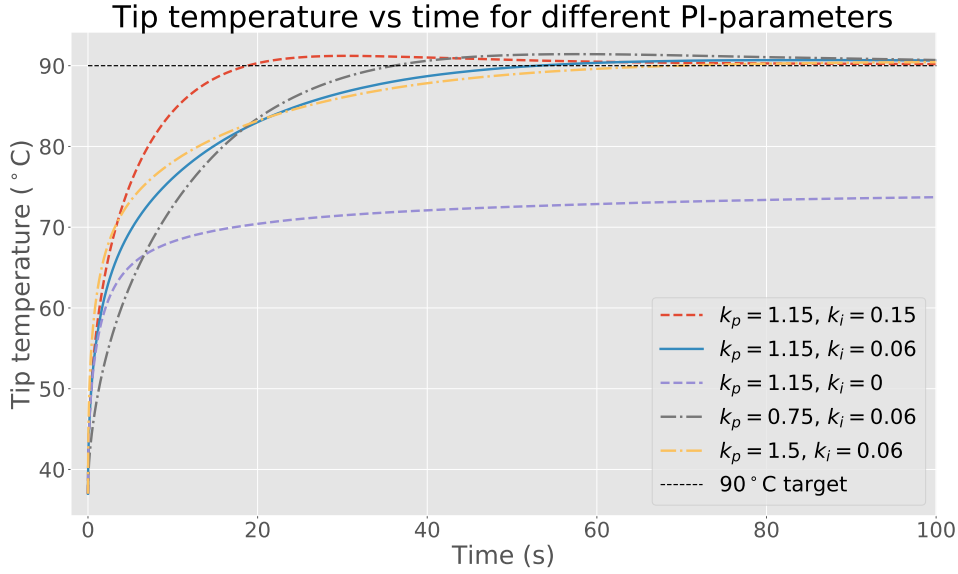
Figure 13: Temperature at the tip of an electrode controlled by a PI-controller, for different values of the PI parameters k_p and k_i. The target temperature was set to be 90°C

13, where the tip temperature over time has been plotted for different values of k_p and k_i with a set target of $T_{target} = 90°C$.

Focusing on this figure we see that the blue line represents the parameters mentioned above. These values for k_p and k_i result in a tip temperature that, after a quick initial jump, gradually reaches its target temperature.

On the other hand, the red line represents an increase in k_i. Due to this increase, the contribution of the integral of all previous voltages over time is increased, which, in turn, leads to an increased applied voltage. This results in the controller reaching its target temperature quicker, but also overshooting the target. After overshooting the target, the $T_{target} - T_t(t)$ term will be negative, and the integral contribution will decrease over time until the target temperature is reached.

The opposite is true for the purple line, which shows a decrease in k_i, meaning that the integral term is lower and the controller reaches its target slower. Low values of k_i can result in the target not being reached over the simulated time. In fact, an absence of the integral term, as pictured here, means that the target is never reached, as at one point the k_p term is not sufficient to drive the temperature further. The effect of changing the k_p-term is more easily understood, as it directly affects the applied voltage, and thus the temperature, as seen by the black and yellow line.

3.3.3 *Impedance-control*

The third type of control is the impedance-control. Here the voltage is either set constant or increasing in stages until a sudden rise in resistivity is measured. This effect is due to the evaporation of tissue which results in a sudden drop of the electrical conductivity. When this rise is measured, the power to the electrode is cut off, and the tissue is allowed to cool down. Then after a certain period, usually 15 seconds, the power is reapplied to continue the process. The reason for this type of control is that the power delivery is sub-optimal when tissue vapor is formed, as it induces tissue charring, which results in a smaller treated ablation volume [29].

The power (W) dissipated in the system can be calculated by

$$P = \int_\Omega Q_{RF} d\Omega \qquad (3.3.2)$$

where Q_{RF} is the heat source due to resistive heating. Using the above, the resistance (Ω) is calculated as

$$R = \frac{V^2}{P} \qquad (3.3.3)$$

Then, the power to the electrode is cut off when the resistance reaches a certain threshold.

3.4 ELECTRIC POTENTIAL

In each simulation, one of the power controls mentioned in the previous section is used. Such a control provides us with an r.m.s voltage, (V_{el}), which is passed on to the next block *Electric potential* (see figure 12). In this block the heat source due to the resistive heating is calculated using a quasi-static approach, meaning that the electric field is assumed to be constant over one time-step, but allowed to change at each time-step iteration of the simulation.

3.4.1 *Equations of the quasi-static approach*

At frequencies used in RF ablation ($\approx$ 500kHz), tissues can be considered totally resistive as displacement currents are negligible. Then, the distribution of the heat source, Q_{rf} is given by

$$Q_{rf} = J \cdot E \qquad (3.4.1)$$

where $E(V/m)$ is the magnitude of the electric field and $J(A/m^2)$ the current density defined as

$$J = \sigma \cdot E \qquad (3.4.2)$$

with $\sigma(S/m)$ being the electrical conductivity. The electric potential is evaluated using Laplace's equation

$$\nabla \cdot \sigma \nabla V = 0 \tag{3.4.3}$$

where V is the electric potential. From V, E is calculated as

$$E = -\nabla V \tag{3.4.4}$$

3.4.2 *Validity of the quasi-static approach*

The limits of this quasi-static approach can be investigated by considering a rectangular piece of tissue with an electrical conductivity σ and permittivity ϵ_r. Having electrodes on opposite faces. Let the area of the electrode faces be A and the distance between them d. Then the resistance, R is defined as

$$R = \frac{d}{\sigma a} \tag{3.4.5}$$

and the capacitance, C, as

$$C = \frac{\epsilon A}{d} \tag{3.4.6}$$

where $\epsilon = \epsilon_r \epsilon_0$, and ϵ_0 being the permettivity of vacuum. For the quasi-static approach to be valid, the capacitive current should be negligible compared to the resistive current, i.e., the phase angle should be small. For this to be true it requires that $R < 1/\omega C$. Substituting into equation 3.4.5 we end up with the following condition

$$\frac{\epsilon \omega}{\sigma} < 1 \tag{3.4.7}$$

For tissue, both σ and ϵ change with frequency. However, a prediction can be made due to various studies on the response of the dielectric properties of tissues over a range of frequencies. For example, the study of S. Gabriel et. al. [30] lists the dielectric properties of muscle at 500 KHz as, $\sigma = 0.446(S/m)$ and $\epsilon_r = 3.65 \cdot 10^3$. Substituting these values in equation 3.4.7 leads to a value on the left-hand side of 0.04 which is well within the limits of our condition.

3.4.3 *Electrical conductivity*

The electrical conductivity, σ, appears twice in the quasi-static approach (see eq. 3.4.3 and eq. 3.4.2) and is a tissue-dependent parameter. However, it is in general temperature dependent and is therefore updated every simulation loop in the *Electrical conductivity*-block (see figure 12). Foremost, it has been shown that the conductivity rises with temperature for the radio-frequency range [25]. To model this, a simple linear percentage increase per kelvin has been shown to be sufficient [31]. Secondly, due to the evaporation of water and formation
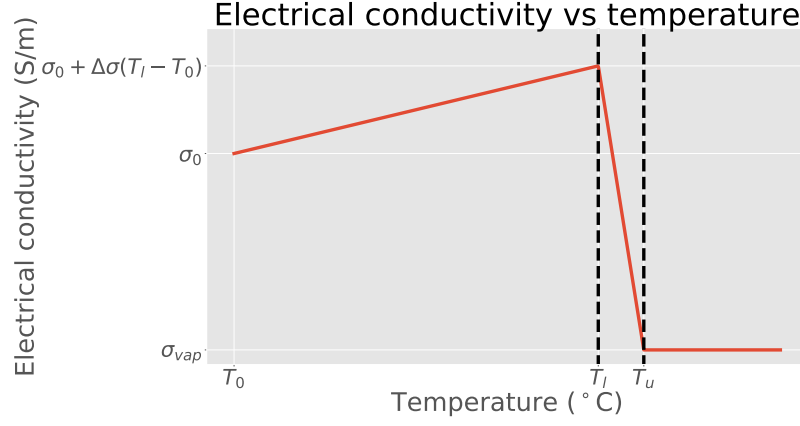
Figure 14: A graph of equation 3.4.8, showing the temperature dependence of the electrical conductivity. Three distinct regions can be seen. First, a linear percentile increase, proportional to $\Delta\sigma$, from its base value, σ_0, from the temperature at which it was measured, T_0, until the temperature at which evaporation occurs T_l. Second, the subsequent rapid linear decrease due to water evaporation. Third, the region above T_u at which the water content has fully vaporized and σ takes on a constant, σ_{vap}.

of gas bubbles around phase change temperatures, a sudden drop of a factor 100 to 10000 in the electrical conductivity appears. This can be modeled as a linear drop between 100°C and 105°C [31]. The electrical conductivity then takes on the form of

$$
\sigma(T) = \begin{cases} \sigma_0 + \Delta\sigma(T - T_0), & T \leqslant T_l \\ \sigma(T_l) + (\sigma_{vap} - (\sigma_0 + \Delta\sigma(T_l - T_0)))\frac{T-T_l}{T_u-T_l}, & T_l < T \leqslant T_u \\ \sigma_{vap}, & T > T_u \end{cases}
$$

$$(3.4.8)$$

where σ_0 is the baseline electrical conductivity (S/m) measured at T_0 (K), $\Delta\sigma$ is the change in conductivity per Kelvin (K^{-1}), σ_{vap} is the electrical conductivity of vaporized tissue (S/m) and T_l, T_u are the lower and upper range of transition respectively. The above expression has also been plotted in figure 14. Note the significant drop in σ between T_l and T_u. The impedance control scheme (section 3.3.3) is based on this phenomenon.

3.4.4 *Appropriate boundary conditions*

Now that we have defined the equations for the electrical conductivity and the resistive heating, we can solve for the source term. However, the equations of the quasi-static approach (section 3.4.1) cannot be applied directly. As seen in section 2.3.3 we must first transform these equations in their corresponding weak formulations. Furthermore, in section 2.4 it was shown that *Neumann* boundary conditions
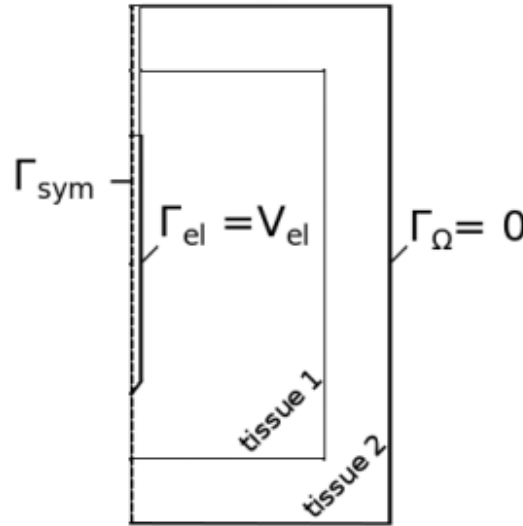
Figure 15: Electrical boundary conditions for an axisymmetric, two-dimensional, model. Γ_{sym} denotes the symmetry-axis. Γ_{el} is the electrode surface boundary, at which a r.m.s. voltage will be specified (V_{el}). Last, the outer boundaries are denoted by Γ_Ω which has a voltage of zero to mimic a dispersive electrode. Note that in the case of a three-dimensional model the symmetry boundary is not present.

are directly incorporated into the weak formulation. Therefore, before defining the weak formulation, we have to specify the appropriate boundary conditions.

A schematic for the boundary conditions in case of an axisymmetric (two-dimensional) case is shown in figure 15. In the case of a three-dimensional model, the boundary condition at the symmetry axis can be ignored.

First, a boundary condition must be set at the surface of the electrode, Γ_{el}. This is done by specifying a Dirichlet boundary condition, where the voltage applied is specified through the power control.

Second, a boundary condition is set at the outer boundaries, Γ_Ω, away from the electrode. This is a zero voltage Dirichlet boundary condition, to mimic the dispersive electrode, or ground-pad, applied to the patient. Last, if the model is an axisymmetric one, a symmetry condition must be imposed on the axis of symmetry, denoted by Γ_{sym}. The flux across a symmetry plane is zero; thus the appropriate symmetry boundary condition is an insulating Neumann condition.

3.4.5 *The weak formulation*

Now that we have defined the appropriate boundary conditions, we can set up the weak formulation of equation 3.4.3. In particular, we need to incorporate the symmetry condition of the axisymmetric case

directly into the weak formulation. However, different weak formulations arise whether one wants to solve an axisymmetric model or a three-dimensional model. Let the model be defined on a domain Ω with an electrode boundary, Γ_{el} and the outer boundary Γ_Ω.

To arrive at the weak-formulation for the three-dimensional case we multiply equation 3.4.3 by a test function, $v \in H^1$, and integrate over the domain Ω on both sides. Let u be the quantity of interest, then the problem reads, find $u \in H^1$ such that

$$\int_\Omega \langle \nabla \cdot \sigma \nabla u \rangle v \, dV = 0, \quad \forall v \in H^1 \tag{3.4.9}$$

Using integration by parts

$$\int_\Omega \sigma \nabla u \cdot \nabla v \, dV - \int_{\Gamma_\Omega} \frac{\delta u}{\delta n} v \, dA = 0 \quad \forall v \in H^1 \tag{3.4.10}$$

Where the second term can be set to zero, since we require the test function to vanish on the boundary, i.e, $v \in H^1_0$

$$\int_\Omega \sigma \nabla u \cdot \nabla v \, dV = 0 \quad \forall v \in H^1 \tag{3.4.11}$$

Replacing v by a test function constructed in a finite element space, $v_h \in V_h \subset H^1_0$ and searching for the finite element approximation u_h results in the finite element problem. Furthermore, to include the Dirichlet boundaries we restrict $u_h = V_{el}$ on Γ_{el} and $u_h = 0$ on Γ_Ω. Find $u_h \in V_h$ such that

$$\int_\Omega \sigma \nabla u_h \cdot \nabla v_h \, dV = 0 \quad \forall v_h \in V_h \tag{3.4.12}$$

For the axisymmetric case, let the model be cylindrically symmetric and defined in the (r, z)-plane. Furthermore, let the symmetry axis be the boundary Γ_{sym} (see figure 15). Now, deriving the weak formulation involves the same steps as for the three-dimensional case, but in cylindrical coordinates.

$$\nabla = \frac{\delta}{\delta r}\hat{r} + \frac{1}{r}\frac{\delta}{\delta \theta}\hat{\theta} + \frac{\delta}{\delta z}\hat{z} \tag{3.4.13}$$

and

$$dV = r dr d\theta dz \tag{3.4.14}$$

Furthermore, we have to include the Neumann boundary condition of zero flux on the symmetry axis

$$\int_\Omega \sigma \nabla u_h \nabla v_h \, r dr dz - \int_{\Gamma_{sym}} 0 v dr dz = 0, \quad \forall v \in V_h \tag{3.4.15}$$

However, as seen in section 2.3.3, the second term vanishes as it is naturally included in the the weak form. And we end up with

$$\int_\Omega \sigma \nabla u_h \nabla v_h \, r dr dz = 0, \quad \forall v_h \in V_h \qquad (3.4.16)$$

Both the three-dimensional as well as the axisymmetric formulation can be solved for the electric potential, and subsequently, the source-term, Q_{RF}, due to resistive heating.

3.5 PENNES' BIOHEAT EQUATION

Following figure 12, we arrive at the *Pennes' bioheat*-block, where we will calculate the temperature distribution. This will be a combination of the prior temperature distribution, plus the contribution due to the source-term, Q_{RF}. Furthermore, because of blood-flow, or *perfusion*, of tissue, a heat-sink is present, as blood at physiological temperatures removes heat. Therefore, the heat transfer during RF ablation is described by a modification of the standard heat equation, known as the *Pennes' bioheat* equation

$$\rho c(T) \frac{\delta T}{\delta t} = \nabla \cdot k(T) \nabla T + Q_{rf} - Q_{perf}(T) + Q_{meta} \qquad (3.5.1)$$

where ρ is the mass density (kg/m^3), c is the specific heat $(J/Kg \cdot K)$, k is the thermal conductivity $(W/m \cdot K)$, T is the temperature (K), Q_{rf} is the heat source (W/m^3), Q_{perf} is the heat loss due to perfusion $(W/m^3$ and Q_{meta} is the heat generated due to metabolic processes (W/m^3). The last term is negligible in the process of RF ablation and therefore ignored [24].

In the following sections, we will go over the material dependent properties, i.e., $k(T)$ and $\rho c(T)$, where the latter has been grouped, as it only appears together in equation 3.5.1.

After that, we further explain the perfusion term, as it is not only a tissue-dependent parameter but also a function of the cell viability, that is to say, the perfusion depends on the damage that has build up within a cell due to hyperthermia. Keeping track of, or modeling of, the cell damage is done by one of the cell death models listed in the *Cell death models*-block (see figure 12). Furthermore, the inclusion of a cell death model will allow for a direct prediction of the cell damage and thus the ablation zone.

Lastly, we derive the appropriate boundary conditions and the weak formulation of equation 3.5.1, similarly as done for the electric potential. However, in addition, the weak formulation has to include some discretization in time as the Pennes' bioheat equation is time-dependent.
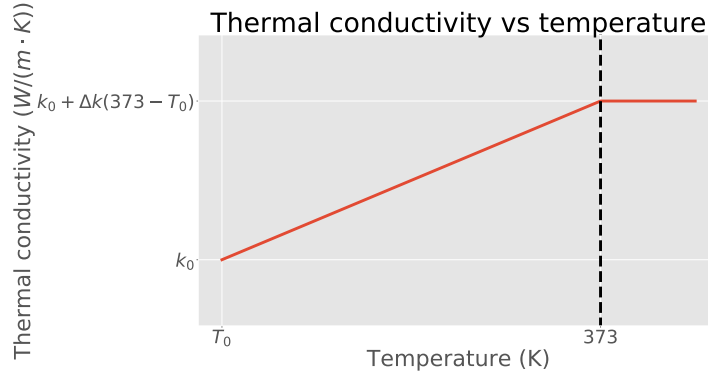
Figure 16: A graph of equation 3.5.2, showing the temperature dependence of the thermal conductivity. Two distinct regions can be seen. First, a linear increase, proportional to Δk, from its base value, k_0, from the temperature at which it was measured, T_0, until 373K. After reaching this temperature, the second region is seen where the thermal conductivity remains at a constant value.

3.5.1 *Thermal conductivity*

The thermal conductivity of is associated with having a linear dependence on the temperature, with a constant value for tissues above 100 °C (373 K) [31], and therefore modeled according to

$$k(T) = \begin{cases} k_0 + \Delta k(T - T_0), & T \leqslant 373K \\ k_0 + \Delta k(373 - T_0), & T > 373K \end{cases} \tag{3.5.2}$$

where k_0 is a baseline thermal conductivity in $(W/(m \cdot K)$, T_0 the temperature at which the baseline value is measured in (K) and Δk is a measure of change per kelvin in the thermal conductivity $(W/(m \cdot K^2))$.

The temperature dependence of the thermal conductivity is also shown in figure 17.

3.5.2 *Apparent heat capacity*

The water contents of tissue start to evaporate as temperatures during RF ablation reach upwards of 100 °C. This leads to a discontinuous jump in the heat capacity during the phase-change. One method of solving such a phase-change problem is by the *apparent heat capacity* method [32].

$$\rho c_{app}(T)\frac{\delta T}{\delta t} = \nabla \cdot k(T)\nabla T - Q_{perf}(T) + Q_{rf} \tag{3.5.3}$$

Densitiy x specific heat vs temperature
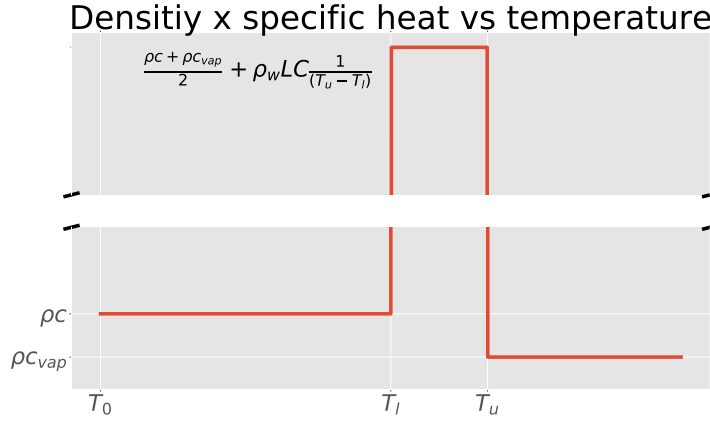
Figure 17: A graph of equation 3.5.4, showing the temperature dependence of the apparent heat capacity. The phase change is modeled by a discontinuous jump in the specific heat of the material.

with

$$
\rho c_{app} = \begin{cases} \rho c, & T \leqslant T_l \\ \frac{\rho c + \rho_{vap} c_{vap}}{2} + \rho_w LC \frac{1}{T_u - T_l}, & T_l \leqslant T \leqslant T_u \\ \rho_{vap} c_{vap}, & T > T_u \end{cases} \tag{3.5.4}
$$

where ρ_{vap} and c_{vap} are the density (J/Kg^3) and specific heat $(J/Kg \cdot K)$ of vaporized tissue respectively, ρ_w is the density (J/Kg^3) of water, L is the latent heat of vaporization (J/Kg) and C is the percentage of water in the tissue. The range over which the phase change takes place is taken to be $T \in [T_l, T_u]$ where T_l and T_u are respectively the lower and upper temperature.

3.5.3   Perfusion and cell death models

The perfusion is modelled as

$$
Q_{perf} = \beta \rho_b c_b \omega (T - T_b) \tag{3.5.5}
$$

where ρ_b is the density of blood (Kg/m^3), c_b is the specific heat of blood $(J/Kg \cdot K)$, and omega is the tissue specific blood perfusion rate s^{-1}. However, tissue perfusion is not constant during ablation as tissue necrosis induces coagulation and stops the perfusion to the tissue. In other words, the tissue perfusion of a cell is halted when its viability drops below a certain threshold. This effect is regulated through the β-term

$$
\beta = \begin{cases} 1, & D > D_0 \\ 0, & D < D_0 \end{cases} \tag{3.5.6}
$$

where D is the cell viability and D_0 the cell death viability threshold.
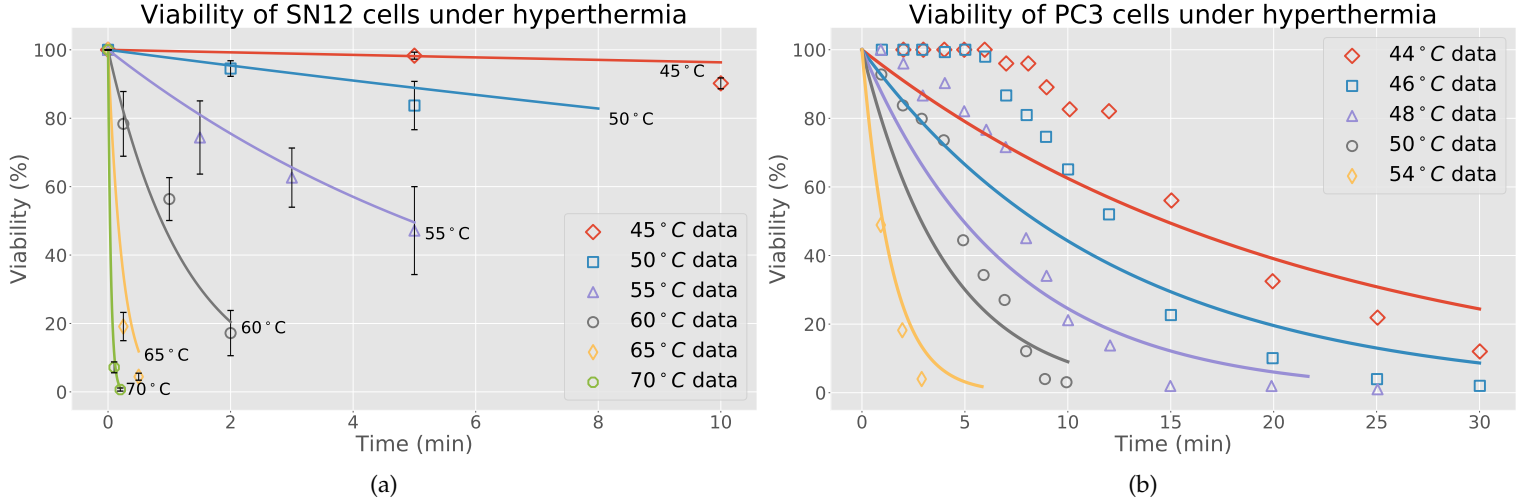
Figure 18: Arrhenius fits of experimental cell viability data under hyperthermia. (a) shows SN12 cells by He and Bischof [33] with fit parameters of $A = 3.153 \cdot 10^{47}$ and $\Delta E = 3.1489 \cdot 10^5$. (b) shows PC3 cells by Feng et al. [34] with fit parameters of $A = 1.19 \cdot 10^{35}$ and $\Delta E = 2.318 \cdot 10^5$. Note that while the SN12 data shows a proper fit, the Arrhenius fit of PC3 cells grossly overestimates the damage at lower temperatures and heating times. The initial period at which no damage occurs under low heating temperatures is known as the *shoulder*-region and is present in the case of PC3 cells.

The cell viability, or better yet, cell damage is calculated through one of the cell death models and is updated each iteration (see figure 12). These models calculate the cell damage due to hyperthermia throughout the simulation. The cell viability can then simply be defined as a lack of cell damage. In the following sections, we go over each of the cell death models. All of them are based on experimental data where the cell viability has been measured as a function of temperature, using cell clonogenicity or fluorescence as a marker of cell viability. However, they differ in the mathematical equations and the types of cells on which the experiments were performed.

3.5.3.1 *The Arrhenius model*

The simplest included model is the *Arrhenius* model, an Arrhenius fit with a single rate constant [35], i.e.

$$\Omega(t) = \int_0^t A e^{\frac{-\Delta E}{RT}} \, dt \tag{3.5.7}$$

where T is the temperature (K), R is the gas constant ($8.3134 \, \mathrm{J/mol \cdot K}$), ΔE the activation energy ($\mathrm{J/mol}$) and A the frequency factor ($\mathrm{s^{-1}}$).

The value of A and ΔE are both experimentally determined for different cell lines. Furthermore, these coefficients are normalized such that

$$\Omega_t = \ln(\frac{1}{D}) \tag{3.5.8}$$

where D the cell viability.

This normalization is used to calculate the cell viability and regulate the perfusion cut-off through equation 3.5.6. For example, commonly encountered values in literature are a threshold of $\Omega = 1$, which yields a viability rate of 36% or $\Omega = 4.6$, a viability rate of 1%[36] [37].

An example of an Arrhenius fit can be seen in figure 18(a). In this figure, adapted from He and Bischof [33], the experimental data and the corresponding Arrhenius fit for the cell viability of SN12 cells (a human kidney cancer cell line) under different heating temperatures is shown. The corresponding fit-parameters were $A = 3.153 \cdot 10^{47}$ and $\Delta E = 3.1489 \cdot 10^5$. It can be seen from this figure that, the Arrhenius fits the experimental data rather well over the range of temperatures.

However, the simple Arrhenius model often fails to provide an adequate fit when a *"shoulder"* region is present. This effect arises when cells show thermal robustness under lower heating temperatures, meaning that, cells can retain their integrity before accumulating damage. This effect can be seen in figure 18(b), which shows the Arrhenius fit to experimental data of the PC3 cell line (a human prostate cancer cell line) under hyperthermia by Feng et al. [34]. Note how the damage is overestimated for lower heating temperatures and heating periods, where in reality no damage occurs due to the shoulder region. This is due to the fitting process over a range of temperatures and heating times, and as such, the Arrhenius model often fails to accurately model the initial shoulder region, in favor of accuracy at longer heating periods and higher temperatures [36]. This is also true for the current example, as the 54 °C line shows an acceptable fit.

The Arrhenius fit parameters used in this section are also summarized in table 3, in addition to parameters for the HepG2 (Human liver cancer) and CHO (Chinese Hamster Ovary) cell lines.

3.5.3.2 *The Arrhenius model with a temperature-dependent time delay*

A method introduced by Pearce improves upon the Arrhenius model by introducing a temperature-dependent time delay [38]. This method sacrifices information in the slowly developing shoulder region in order to obtain a more accurate estimate of the later, constant region. However, in treatment planning, the goal is to obtain a final prediction of the ablation-zone without overestimating its extent. In that case, as reasoned by Pearce, the shoulder region can be ignored as
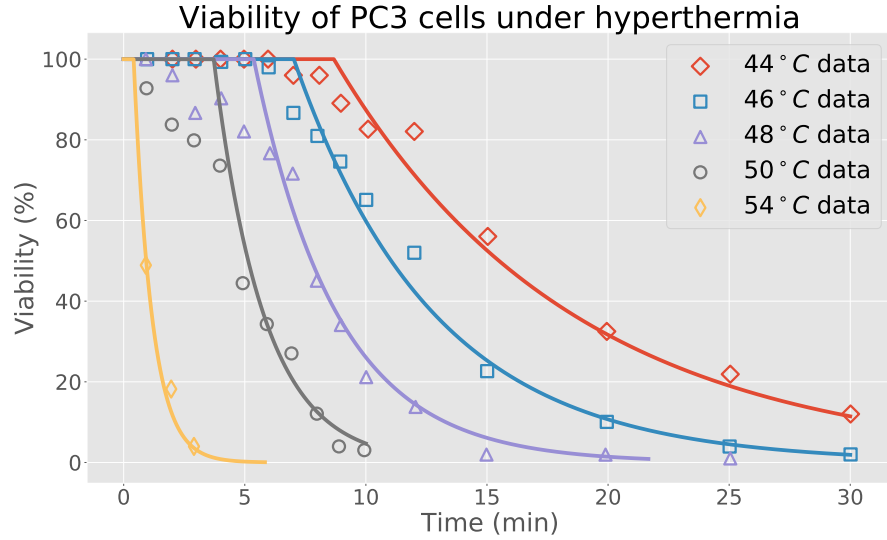
Figure 19: Arrhenius fit with a temperature-dependent time delay of PC3 cells, adapted from Pearce[38]. Corresponding fit parameters were $A = 6.75 \cdot 10^{33}$, $\Delta E = 222.2 \cdot 10^3$, $b = 2703$ and $m = 49.6$. Note the improved fit over the original Arrhenius fit in figure 18(b).

long as it is accounted for within the calculation. And this is what the time delay does.

Referring back to figure 3.5.7(b) as an example. Instead of the exponential fit being performed on the whole data-set, one only includes data points at which the cell accumulates damage. After which a temperature-dependent linear time delay is fitted to the data at which no damage is measured. The time delay is of the form of

$$t_d = b - mT \qquad (3.5.9)$$

where t_d is the time delay before the damage accumulation starts (s), b an offset (s), m an offset factor ($s°C^{-1}$), and T the heating temperature (°C).

For example, the original Arrhenius fit of PC3-cells in figure 18(b) benefits greatly from this time delay, as demonstrated by Pearce[38]. In this case, the revised parameters become $A = 6.75 \cdot 10^{33}$, $\Delta E = 222.2 \cdot 10^3$, $b = 2703$ and $m = 49.6$. The resulting fit is shown in figure 19.

The above time delay means that at a constant heating temperature of 44°C, the damage accumulation is delayed by 520 seconds. Alternatively, looking at it the other way around, a constant heating temperature of 54.5 °C is required for there to be no time delay at all.

As with the Arrhenius model, the cell viability can be calculated according to equation 3.5.8. Moreover, a cell viability threshold can be set to regulate the perfusion according to equation 3.5.6.

The improved fit parameters used in this section, as well as improved fit parameters for the CHO cell line are given in table 3.

3.5.3.3   *Three-state cell death model*

Another model is the *three-state* model of hyperthermic cell death by O'Neill et al. [39]. Instead of a single reaction rate, this model is based on three states in which a cell can reside, an alive state, A, a vulnerable intermediate state, V, and a dead state, D. Cells in a vulnerable state represent a state where the cell's function is impaired, but not fully dead, and has a chance to return to the alive state. The dead state consists of cells which have undergone irreversible thermal damage. The following rate reaction can describe these processes

$$A \underset{k_b}{\overset{k_f}{\rightleftharpoons}} V \xrightarrow{k_f} D \tag{3.5.10}$$

The underlying progression of cell death is modeled by a single damage mechanics. Thus the process from alive to dead is taken to be two stages of a single process and therefore modeled by a single forward rate constant k_f. The backward rate k_b is associated with the healing of a cell and is therefore modeled by a different rate. Since all cells are either in the alive, vulnerable or dead state we have

$$A + V + D = 1 \tag{3.5.11}$$

Thus the system can be reduced to two coupled differential equations

$$\frac{dA}{dt} = -k_f A + k_b(1 - A - D) \tag{3.5.12a}$$

$$\frac{dD}{dt} = k_f(1 - A - D) \tag{3.5.12b}$$

To account for the fact that there is practically no thermal damage at normothermia, the forward rate at 37°C must be small and after that increasing with temperature. O'Neill et al. chose an exponential dependence to mimic this behavior. Furthermore, already damaged tissue will be most susceptible to further damage and will have a nonlinear influence on the cell viability. Therefore, the forward reaction rate is multiplied by the term $(1 - A)$, the fraction of vulnerable and dead cells, which will increase as the fraction of alive cells decreases. The combination of the above leads to a forward rate of

$$k_f = \bar{k}_f e^{\frac{T}{T_k}}(1 - A) \tag{3.5.13}$$

where $\bar{k}_f$ is a scaling rate (s^{-1}) and T_k a rate that sets the exponential increase (°C). Thus the process is governed by three variables $\bar{k}_f$, k_b, T_k.

  Because of the term $(1 - A)$ in equation 3.5.13, a fully alive cell, e.g. $A = 1$, leads to a static solution. This has been remedied by setting the initial conditions to $A = 0.99, V = 0.01$ which had a negligible effect on the system.

  O'Neill et al. performed experiments to which these parameters were fitted. The different make-up of co-cultures of human liver hepatocellular carcinoma, HepG2, and human lung fibroblast, MRC-5,

	Co-culture cell line make-up (% content of MRC-5)					
Parameter	0%	25%	50%	75%	100%	Average
$\bar{k}_f$	$0.80 \times 10^{-3} s^{-1}$	$2.62 \times 10^{-3} s^{-1}$	$3.52 \times 10^{-3} s^{-1}$	$4.54 \times 10^{-3} s^{-1}$	$9.07 \times 10^{-3} s^{-1}$	$3.33 \times 10^{-3} s^{-1}$
k_b	$0.25 \times 10^{-3} s^{-1}$	$5.74 \times 10^{-3} s^{-1}$	$8.46 \times 10^{-3} s^{-1}$	$10.8 \times 10^{-3} s^{-1}$	$19.2 \times 10^{-3} s^{-1}$	$7.77 \times 10^{-3} s^{-1}$
T_k	24.6 °C	36.7 °C	41.6 °C	46.3 °C	63.5 °C	40.5 °C

Table 2: List of optimized cell death model parameters for the three-state cell death model of O'Neill et al. for different co-cultures of MRC-5 and HepG2, and for an average over all co-culture make-ups. All data taken from [39]

were heated for different periods for different heating constants. Then the cell viability was measured as a function of the fluorescence, which signifies the metabolic activity of the living cells. Furthermore, a fit has been performed where the co-culture data has been averaged. The results are given in table 2.

While this model accounts for cell death processes during the timescale of RF ablation, it is known from the experimental data that the cell viability continues to decrease up to 50 hours after the ablation. Therefore, a secondary slower mechanism is implemented, the so-called *slow* cell death model. In this model, cells can transition from the alive and the vulnerable state to the dead state, but there is no opportunity for healing. This can be modeled by a single reaction rate

$$(1 - D) \xrightarrow{k\_s} D \qquad (3.5.14)$$

and the resulting partial differential equation

$$\frac{dD}{dt} = k_s(1 - D) \qquad (3.5.15)$$

with

$$k_s = \bar{k}_s D(1 - D)(D - D_t)^2 \qquad (3.5.16)$$

where k_s is a scaling rate (s^{-1}) and D_t a threshold for maximum cell death for cells which have undergone minimal damage. This form of k_s was chosen as it is a positive value, indicating that no dead cells return to the alive state, $k_s = 0$ at $D = 0$, and thus no cells die when tissue is 100% alive, and lastly, $k_s = 0$ at D_t such that there is a maximum value of cell death for tissues which have undergone minimal damage. The slow cell death model is governed by two parameters $\bar{k}_s$ and D_t. These parameters have been fit to experimental data of the cell viability after a post-heating incubation time. Optimized values for these parameters were found by O'Neill et al.

$$\bar{k}_s = 0.316 \times 10^{-3} s^{-1} \qquad (3.5.17a)$$

$$D_t = 0.208 \qquad (3.5.17b)$$

Further, it was found that once cells pass the 80% viability threshold, they would progress to an entirely dead state. Thus making it an indicator for cell death and after that perfusion is stopped. The appropriate form of the β-term for regulation of the perfusion in equation 3.5.5 for the three-state model can be written as

$$\beta = \begin{cases} 1, & (1-D) > 0.8 \\ 0, & (1-D) \leqslant 0.8 \end{cases} \tag{3.5.18}$$

As for the other cell death models, a summary of the parameters used in the three-state model regarding different cell lines is given in table 3. Furthermore, due to the coupled equations of A (eq. 3.5.12a) and D (eq. 3.5.12b), the implementation of the three-state cell death model is more complicated than the Arrhenius model. Therefore, the implementation of this model has been tested by retrieving the original fits to the experimental data found in O'Neill et al. The cell viability data is therefore shown in the next chapter, which entails the model validation, in figure 31.

3.6 APPROPRIATE BOUNDARY CONDITIONS

Now that we have a grasp of the involved terms of the Pennes' bioheat equation (eq. 3.5.1), we can start to solve the resulting temperature distribution. However, as for the electric potential, we need to derive the weak formulation of the Pennes' bioheat equation, and before that, define all the appropriate boundary conditions.

As it turns out, the same boundaries as for the electric potential in figure 15 are used. First, Dirichlet boundaries of constant initial temperature are set at the outer model boundaries, Γ_Ω, as it is assumed the temperature at the boundary remains unchanged, provided that the domain is large enough.

Second, an optional cooled tip can be modeled through a convective Neumann condition on the electrode surface, Γ_{el}. These types of electrode provide an extra cooling element in the procedure, extending the depth at which the maximum temperature arises within the tissue, and helps to prevent tissue charring [11].

Last, for the axisymmetric case, an insulating Neumann condition must be set at the symmetry axis, Γ_{sym}, to ensure zero-flux across this boundary.

Model			Coeficcients			
Three-state			$\bar{k}_f$	k_b	T_k	
cell line	Type	range (°C)	$(\times 10^{-3}s^{-1})$	$(\times 10^{-3}s^{-1})$	(°C)	ref
HepG2	Human liver cancer	37-100	0.8	0.25	24.6	[39]
MRC-5	Human lung	37-100	9.07	19.2	63.5	[39]
Arrhenius			A		ΔE	
			(s^{-1})		$(Jmol^{-1})$	
HepG2	Human liver cancer	50-70	5.396×10^{36}		2.486×10^5	[40]
CHO	Chinese hamster ovary	42.5-46	6.355×10^{97}		6.102×10^5	[41]
PC3	Human prostate cancer	44-60	1.19×10^{35}		2.318×10^5	[34]
SN12	Human kidney cancer	45-70	3.153×10^{47}		3.1489×10^5	[33]
Arrhenius with delay			A	ΔE	$t_d = b - mT$	
			(s^{-1})	$(Jmol^{-1})$	b(s))	m(sC^{-1}))
PC3	Human prostate cancer	44-60	6.75×10^{33}	2.222×10^5	2703	49.6	[38]
CHO	Chinese hamster ovary	42.5-46	7.254×10^{100}	6.275×10^5	26062	555.9	[38]

Table 3: Summary of cell death models and its parameters for various cell lines.

One more step must be taken before the weak formulation can be derived. The time derivative of the Pennes' bioheat equation must be approximated discretizing in time.

Two different time stepping schemes have been implemented, the implicit Euler method and a three-level explicit scheme known as *Lees'* method.

3.7.1 *The implicit Euler Method*

The implicit Euler method, as discussed in section 2.7, is relatively straight-forward to implement, formulation and programming-wise. The premise of this method is based on the assumption that the temperature varies linearly in time. Then, the Pennes' bioheat equation (eq. 3.5.1) can be rewritten as

$$\rho c_{app}(T^{(n+1)})\frac{T^{(n+1)} - T^{(n)}}{\Delta t} = \nabla \cdot k(T^{(n+1)})\nabla T^{(n+1)} - \beta c_b \rho_b \omega(T^{(n+1)} - T_b) + Q_{rf}$$

(3.7.1)

where $T^{(n)}$ is the known temperature at the current time step, $T^{(n+1)}$ is the temperature at the next time step, and Δt is the time step size.

The next step is transforming the above expression into its corresponding weak formulation for use in the finite element method. The weak formulation for the three-dimensional case is obtained by multiplying equation 3.7.1 with a test function, $v \in H_0^1$ and integrating over the domain.

For this let $T^{(n+1)}$ be a square integrable function, Ω the domain of interest and Γ_Ω the outer boundary. After integration by parts and bringing all the terms to one side, the weak formulation reads:

find $T^{(n+1)} \in H_0^1$ such that

$$0 = \int_\Omega \rho c_{app}(T^{(n+1)})T^{(n+1)}v \, d\Omega + \Delta t \int_\Omega k(T^{(n+1)})(\nabla T^{(n+1)} \cdot \nabla v) \, d\Omega$$

$$- \Delta t \int_\Omega Q_{rf}v \, d\Omega + \Delta t \int_\Omega \beta \rho_b c_b \omega(T^{(n+1)} - T_b)v \, d\Omega$$

$$- \int_\Omega T^{(n)}v \, d\Omega, \quad \forall v \in H_0^1$$

(3.7.2)

The axisymmetric weak formulation is obtained by following the same steps as we did for the axisymmetric electric potential solver.

Using figure 15 as a reference, let Ω be a cylindrically symmetric domain, Γ_{sym} denote the line of symmetry and Γ_Ω the boundaries away from the axis of symmetry. Then the weak formulation reads:

find $T^{(n+1)} \in H_0^1$ such that

$$
\begin{aligned}
0 = &\int_\Omega \rho c_{app}(T^{(n+1)})T^{(n+1)}rv\,d\Omega + \Delta t \int_\Omega k(T^{(n+1)})(\nabla T^{(n+1)} \cdot \nabla v)r\,d\Omega \\
&- \Delta t \int_\Omega Q_{rf}rv\,d\Omega + \Delta t \int_\Omega \beta \rho_b c_b \omega(T^{(n+1)} - T_b)rv\,d\Omega \\
&- \int_\Omega T^{(n)}rv\,d\Omega, \quad \forall v \in H_0^1
\end{aligned}
$$

(3.7.3)

Where the symmetry Neumann condition vanishes as it is naturally included in the weak formulation.

The drawback of this method is that any temperature dependence of the material properties leads to a non-linear system of equations, which has to be linearized first using methods such as the Picard iteration (see section 2.7.1), or Newton's method (see section 2.7.2). Still, this method shows accurate results when a small model is considered. Furthermore, this implementation can act as a benchmark for more complicated schemes.

3.7.1.1 *The explicit Lees method*

Lees' method [42] is a *three-level* time stepping scheme as described in [43]. The main advantage is that the algorithm evaluates the non-linear material-properties at a known time-step, and thus, do not need to be evaluated through linearization. Furthermore, since it is a three-level scheme, we will show that the local truncation error is of order three, an improvement over the Euler method (see section 2.7).

Further, an additional benefit comes in the form of an automated time step control. After each iteration, the difference in temperature at the mesh nodes is calculated between the new temperature and the previous temperature. If this measure is below a certain lower tolerance, τ_l, the time step (Δt) is increased. On the other hand, if the measure is above an upper tolerance, τ_u, the time step is decreased. This ensures that small enough time-steps are taken when the temperature-field changes rapidly between iterations, but it allows for greater time-steps when the temperature changes are smaller.

First let the unknown temperature, T be approximated by a linear combination of shape functions, i.e.

$$
T = \sum_{i=1}^n N_i(x, y, z)T_i(t)
$$

(3.7.4)

Then the weak formulation of equation 3.5.3 can be written in matrix form as

$$
C\dot{T} + KT + F = 0
$$

(3.7.5)

with

$$C_{ij} = \sum \int_{\Omega_e} \rho c_{app} N_j N_i \, d\Omega \tag{3.7.6a}$$

$$K_{ij} = \sum \int_{\Omega_e} k(T)(\nabla N_j \cdot \nabla N_i) + \beta \rho_b c_b w N_j N_i \, d\Omega \tag{3.7.6b}$$

$$F_i = -\sum \int_{\Omega_e} N_i Q_{rf} + \beta \rho_b c_b w T_b N_i \, d\Omega \tag{3.7.6c}$$

Let the temperature be linear over the interval $2\Delta t$, then we can use the approximations

$$T^{(n)} = \frac{1}{3}(T^{(n+1)} + T^{(n)} + T^{(n-1)}) \tag{3.7.7}$$

and

$$\dot{T}^{(n)} = \frac{T^{(n+1)} - T^{(n-1)}}{2\Delta t} \tag{3.7.8}$$

where $T^{(n)}$ is the known temperature at time t, $T^{(n-1)}$ is also known and is the temperature at the previous time $t - \Delta t$, and $T^{(n+1)}$ is the desired temperature at time $t + \Delta t$.

Substituting both approximations into equation 3.7.5 yields

$$C^{(n)} \frac{T^{(n+1)} - T^{(n-1)}}{2\Delta t} + K^{(n)} \frac{(T^{(n+1)} + T^{(n)} + T^{(n-1)})}{3} + F^{(n)} = 0 \tag{3.7.9}$$

Rearranging the terms lead to the following formula

$$-(K^{(n)} + \frac{3}{2\Delta t}C^{(n)})T^{(n+1)} = K^{(n)}T^{(n)} + K^{(n)}T^{(n-1)} - \frac{3}{2\Delta t}C^{(n)}T^{(n-1)} + 3F^{(n)} \tag{3.7.10}$$

In which only values C, K and F occur at the current time (n), which are known. Therefore, this scheme is fully explicit, however it is not self-starting, as two initial temperature profiles are needed. This can be solved by either taking initial time steps small enough for the temperature to remain constant, or using one Euler iteration to arrive at two starting conditions. This algorithm has been shown to be unconditionally stable [44] and has been successfully implemented in other simulations [43].

The local truncation error of Lees' method can be investigated by considering a general form of the time derivative discretization, i.e.

$$T^{(n+1)} = T^{(n-1)} + 2\Delta t f(t, T^{(n)}) \tag{3.7.11}$$

and thus

$$\epsilon^{(t)} = T^{(n+1)} - T^{(n-1)} - 2\Delta t f(t, T^{(n)}) \tag{3.7.12}$$

Now we expand both $T_{t+\Delta t}$ and $T_{t-\Delta t}$ in their Taylor series around $T(t)$

$$T^{(n+1)} = T^{(n)} + \Delta t T'(t) + \frac{(\Delta t)^2}{2}T''(t) + \frac{(\Delta t)^3}{6}T'''(t) + O((\Delta t)^3) \tag{3.7.13a}$$

$$T^{(n-1)} = T^{(n)} - \Delta t T'(t) + \frac{(\Delta t)^2}{2}T''(t) - \frac{(\Delta t)^3}{6}T'''(t) + O((\Delta t)^3)$$
$$(3.7.13b)$$

substituting the above expressions into 3.7.12 yields

$$\epsilon^{(n)} = \frac{(\Delta t)^3}{3}T(t) + O((\Delta t)^5) \qquad (3.7.14)$$

Thus, the local truncation is of order three, one higher than the result found for the implicit euler method (eq. 2.7.12).

3.7.2   *Cool-down*

Using either of the two time-stepping schemes allows for the calculation of the new temperature distribution. Then, looking back at figure 12, the new temperature distribution is passed back to the beginning to start the loop anew. This process is repeated until the simulation has run for the desired period.

However, as heat is not immediately dissipated when the procedure has finished, a cool-down part has been implemented. The cool-down can be seen as a dashed line in figure 12. Cool-down is the period after the ablation procedure, where the power has been shut-off, and the heat is allowed to dissipate. Therefore, during this period, the source-term is no longer updated and set to zero.

Since heat resides in the tissue, so does damage still take place during this cool-down period. The Pennes' bioheat and cell death blocks continue to get updated until the maximum temperature in the mesh is below a certain threshold at which the mesh is considered cooled-down.

After that, the simulation has finished, and a prediction of the final ablation-zone can be made using either the temperature distribution before the initiation of the cool-down phase, or the final cell viability distribution.

However, before we can start to simulate our models, it is of importance to validate the current implementation, which will be the subject of the next chapter.

VALIDATION OF THE MODEL

The validation of the finite element model is be performed in three different ways.

First, we use the *method of manufactured solutions*, to perform tests which can confirm that the implementation of the weak formulations is correct. These methods are not based on any physical phenomenon, but instead, we impose boundary conditions which correspond to a predefined solution and check if the solver arrives at this solution with the correct convergence rates.

Second, physical examples can be sought which have analytical solutions, usually exploiting some symmetry or considering semi-infinite models. These allow for more complex interactions in the model to be tested, while still having an exact solution.

Last, the model can be validated against experimental data, where the resulting simulations are shown to be within a specified tolerance of the experimental data.

4.1 METHOD OF MANUFACTURED SOLUTIONS

This method relies on the construction of boundary and initial conditions such that an exact analytical solution is retrieved, usually a polynomial, or an infinitely differentiable function. Since we know the solution ourselves, we can calculate the error. This error should be within machine precision when the function is a polynomial of degree p, and the FEM basis function are also of order p.

However, more interestingly, when the underlying basis functions are of a degree less than p the solver introduces some error w.r.t our function. However, we also know that refining the mesh, i.e., adding more elements, decreases the error of the solution. In section 2.5.4 it has been shown that the convergence of the error w.r.t. to mesh size should be proportional to the mesh size. It is the convergence rate which is used to determine if the solver implementation is correct.

To demonstrate this we refer back to the electrostatic problem (equation 3.4.3) but with an added source term,

$$\nabla \cdot \sigma \nabla V(x, y) = f(x, y) \tag{4.1.1}$$

The source term has been added such that we can test any function and just calculate the corresponding source term. Now suppose our imposed solution is a quadratic polynomial, e.g.

$$V(x, y) = \alpha x^2 + \beta y + c \tag{4.1.2}$$

If we want the solver to solve equation 4.1.1 and end up with equation 4.1.2, we have to provide the correct source term. Assuming σ constant for now, by manually differentiating we end up with

$$f = 2\alpha\sigma \tag{4.1.3}$$

Now the finite element solution of u can be retrieved by substituting the above source term, f, into equation 4.1.1. We also set the boundary to be equal to the values of the exact solution, u.

The only thing left is specifying the degree of the basis functions we use in the solver. If, in this case, we use basis functions of order two, the exact solution is retrieved, as second order basis functions can represent polynomials of the second order exactly. However, as said before, it is the convergence of the solution on lower order basis functions which is used in the manufactured solutions test. In particular, the convergence rates were determined in section 2.5.4 and given in equation 2.5.42, which is repeated here

$$|u - u_i|_{H^d} \leqslant Ch^{p-d+1}|u|_{H^{p+1}} \tag{4.1.4}$$

Where h^{p-d+1} is the relevant term with h the characteristic mesh size, p the degree of the basis functions and d the order of the semi-norm used to calculate the error.

For example, if we want to test the convergence rate of the solution of the case mentioned above, we can use at most basis functions of degree one, $p = 1$. Then, we can calculate the error in a H^d semi-norm, in particular the $\|e\|_{L^2} \equiv |e|_{H^0}$ (see eq. 2.3.15) and $|e|_{H^1}$ (see eq. 2.3.16) semi-norms. Using the appropriate values for p and d, according to equation 4.1.4, the error in these norms should converge proportional to h^2 and h respectively.

The convergence rate can be asserted by calculating two successive finite element solutions, and their errors, e_i, e_{i-1}, where the mesh size parameter, h, has halved. Then the convergence rate, r, can be calculated as

$$r = \frac{\ln(\frac{e_i}{e_{i-1}})}{\ln(\frac{h_i}{h_{i-1}})} \tag{4.1.5}$$

4.1.1   *The electric potential solver*

In this section, we validate the electric potential solver with the use of the manufactured solutions method as described above. Both the three-dimensional model as the axisymmetric model need to be validated independently, as they are formulated by different weak formulations.

4.1.1.1   *Three-dimensional convergence rates*

The error convergence rates have been investigated for different polynomials of the form

$$V(x, y, z) = (\alpha_x x + \alpha_y y + \alpha_z z + c)^p \qquad (4.1.6)$$

with a constant sigma.

As mentioned, we can use any arbitrary polynomial we desire. In practice, polynomials and basis functions of higher degrees consume more memory. Therefore, in order for the results to be reproducible, we use the following polynomial of order three

$$V_{(x, y, z)} = (6x + 2y + z + 19)^3 \qquad (4.1.7)$$

Substituting the above expression into equation 4.1.1 yields the corresponding source term

$$f(x, y, z) = -\sigma(1476x + 492y + 246z + 4674) \qquad (4.1.8)$$

Since the solution is a polynomial of order three, we can investigate the convergence rates using basis functions of order one and two.

Using equation 4.1.4 we expect that basis functions of order one ($p = 1$) should show a convergence rate of two and one for the $|e|_{H^0}$ and $|e|_{H^1}$ semi-norms respectively. Similarly, using second order basis functions we can expect a convergence rate of three and two for the $|e|_{H^0}$ and $|e|_{H^1}$ semi-norms respectively.

To calculate the convergence rate, the solutions are approximated on meshes of increasing resolution. In this particular case, a unit cubic mesh is chosen which is split into N elements in each direction, such that the mesh is uniform. Consequently, a uniform mesh parameter can be defined as $h = 1/N$. Then, using two subsequent solutions, we can calculate the order of convergence using equation 4.1.5.

The results are presented in table 4 with $\sigma = 1$. Where it is seen that all the convergence rates are as expected.

A second convergence test has been performed where, instead of a polynomial, the solution is of the form

$$V(x, y, z) = \sin(\pi\omega x)\sin(\pi\omega y)\sin(\pi\omega x) \qquad (4.1.9)$$

and again, using equation 4.1.1, we have a corresponding source term

$$f(x, y, z) = 3\sigma\pi^2\omega^2 V(x, y, z) \qquad (4.1.10)$$

This solution cannot be exactly retrieved by any polynomial basis function, and thus, has as benefit that we can investigate the order of convergence using any order of basis functions. However, as mentioned, higher order basis functions are more computationally expensive. Therefore, we limit ourselves to basis functions of order one and two, which should have the same convergence behavior as the basis

	p=1				p=2			
N	H^0	r_{H^0}	H^1	r_{H^1}	H^0	r_{H^0}	H^1	r_{H^1}
2	1.96×10^2	-	1.25×10^3	-	1.83×10^0	-	2.55×10^1	-
4	4.90×10^1	2.00	6.22×10^2	1.01	2.29×10^{-1}	3.00	6.37×10^0	2.00
8	1.22×10^1	2.00	3.10×10^2	1.00	2.86×10^{-2}	3.00	1.59×10^0	2.00
16	3.06×10^0	2.00	1.55×10^2	1.00	3.58×10^{-3}	3.00	3.98×10^{-1}	2.00
32	7.65×10^{-1}	2.00	7.75×10^1	1.00	4.47×10^{-4}	3.00	9.95×10^{-2}	2.00

Table 4: Three-dimensional electric potential convergence rates of the finite element solution of a polynomial of degree three (equation 4.1.7), by polynomials of degree $p = 1$ and $p = 2$ respectively. The errors are measured in the H^0 and H^1 semi-norms and their convergence are denoted r_{H^0} and r_{H^1} respectively. The number of elements in the mesh, N, is doubled every iteration.

	p=1				p=2			
N	H^0	r_{H^0}	H^1	r_{H^1}	H^0	r_{H^0}	H^1	r_{H^1}
2	2.64×10^{-1}	-	1.58×10^0	-	5.51×10^{-2}	-	5.84×10^{-1}	-
4	1.19×10^{-1}	1.15	9.45×10^{-1}	0.75	6.59×10^{-3}	3.06	1.69×10^{-1}	1.79
8	3.60×10^{-2}	1.72	4.86×10^{-1}	0.96	7.44×10^{-4}	3.15	4.50×10^{-2}	1.91
16	9.50×10^{-3}	1.92	2.44×10^{-1}	1.00	8.92×10^{-5}	3.06	1.15×10^{-2}	1.97
32	2.41×10^{-3}	1.98	1.22×10^{-1}	1.00	1.10×10^{-5}	3.02	2.89×10^{-3}	1.99

Table 5: Three-dimensional electric potential convergence rates of the finite element solution of a sine function (equation 4.1.9), by polynomials of degree $p = 1$ and $p = 2$ respectively. The errors are measured in the H^0 and H^1 semi-norms and their convergence are denoted r_{H^0} and r_{H^1} respectively. The number of elements in the mesh, N, is doubled every iteration.

functions in the previous test. The results are shown in table 5 with $\sigma = \omega = 1$.

Deviations from the convergence rate at a lower resolution can be attributed to errors due to the interpolation of the source term and the boundary terms on such a low-resolution mesh. However, when the mesh is refined, the expected convergence rates are retrieved.

4.1.2 *Axisymmetric convergence rates*

Convergence rate tests have also been performed for the axisymmetric model, as its weak formulation requires a different implementation than the three-dimensional case. Again, the first test was determining the convergence rate for a polynomial of the form

$$V(r, z) = (\alpha_r r + \alpha_z z + c)^p \qquad (4.1.11)$$

Where, again, we can choose the parameters as we see fit. The benefit of the axisymmetric, two-dimensional, model is the less restrictive

N	p=2				p=3			
	H^0	r_{H^0}	H^1	r_{H^1}	H^0	r_{H^0}	H^1	r_{H^1}
2	3.22×10^3	-	4.82×10^4	-	3.93×10^1	-	7.61×10^2	-
4	3.99×10^2	3.01	1.20×10^4	2.00	2.30×10^0	4.09	9.28×10^1	3.04
8	4.97×10^1	3.01	3.00×10^3	2.00	1.38×10^{-1}	4.06	1.14×10^1	3.02
16	6.20×10^0	3.00	7.52×10^2	2.00	8.42×10^{-3}	4.03	1.42×10^0	3.01
32	7.75×10^{-1}	3.00	1.88×10^2	2.00	5.19×10^{-4}	4.02	1.77×10^{-1}	3.01
64	9.68×10^{-2}	3.00	4.70×10^1	2.00	3.22×10^{-5}	4.01	2.20×10^{-1}	3.00

Table 6: Two-dimensional, axisymmetric, electric potential convergence rates of the finite element solution of a polynomial of degree five (equation 4.1.12), by polynomials of degree $p = 2$ and $p = 3$ respectively. The errors are measured in the H^0 and H^1 semi-norms and their convergence are denoted r_{H^0} and r_{H^1} respectively. The number of elements in the mesh, N, is doubled every iteration.

memory requirement allows us to test higher-order basis functions. Therefore, we have chosen a polynomial of degree 5

$$V(r, z) = (10r + 10z + 12)^5 \qquad (4.1.12)$$

And the corresponding source term is

$$f(r, z) = -\frac{1}{r}(11200r + 1600z + 1920)(5r + 5z + 6)^2 \qquad (4.1.13)$$

Where we will calculate the solution on basis functions of order two and three. The expected convergence rates, according to equation 4.1.4, for basis functions of order two, are three and two for the $|e|_{H^0}$ and $|e|_{H^1}$ semi-norms respectively. Whereas for the basis functions of order three, convergence rates of four and three for respectively the $|e|_{H^0}$ and $|e|_{H^1}$ semi-norms are expected.

The solutions are approximated on a uniform two-dimensional unit-square mesh, which is split into N elements in each direction. Again, we can define a uniform mesh parameter as $h = 1/N$. The convergence rates are then calculated according to equation 4.1.5 The results are given in table 6 and are in accordance with the expected rates of convergence.

A second convergence test is performed where the solution is of the form

$$V(r, z) = \sin(\omega \pi r)\sin(\omega \pi z) \qquad (4.1.14)$$

and consequently

$$f(r, z) = \frac{-\omega \pi}{r}\cos(\omega \pi r)\sin(\omega \pi z) + 2\omega^2 \pi^2 u(r, z) \qquad (4.1.15)$$

The results are shown in table 7. Where it is seen that the expected convergence results are retrieved as the mesh is refined.

	p=2				p=3			
N	H^0	r_{H^0}	H^1	r_{H^1}	H^0	r_{H^0}	H^1	r_{H^1}
2	4.12×10^{-2}	-	4.70×10^{-1}	-	5.40×10^{-3}	-	1.02×10^{-1}	-
4	4.80×10^{-3}	3.10	1.30×10^{-1}	1.86	3.55×10^{-4}	3.93	1.32×10^{-2}	2.94
8	5.66×10^{-4}	3.08	3.34×10^{-2}	1.96	2.20×10^{-5}	4.02	1.66×10^{-3}	3.00
16	6.93×10^{-5}	3.03	8.42×10^{-3}	1.99	1.35×10^{-6}	4.02	2.06×10^{-4}	3.01
32	8.62×10^{-6}	3.01	2.11×10^{-3}	2.00	8.40×10^{-8}	4.01	2.57×10^{-5}	3.00
64	1.08×10^{-6}	3.00	5.28×10^{-4}	2.00	5.23×10^{-9}	4.01	3.21×10^{-5}	3.00

Table 7: Two-dimensional, axisymmetric, electric potential convergence rates of the finite element solution of a sine function (equation 4.1.7), by polynomials of degree p = 2 and p = 3 respectively. The errors are measured in the H^0 and H^1 semi-norms and their convergence are denoted r_{H^0} and r_{H^1} respectively. The number of elements in the mesh, N, is doubled every iteration.

4.1.3 *Three-dimensional vs axisymmetric*

We have shown that the three-dimensional and axisymmetric solvers show their expected convergence rates. As a final test, it rests on showing that a three-dimensional representation of the axisymmetric model shows the same results. To this end, we choose the solution in the axisymmetric case, and the respective source term of the form

$$V_{axi}(r,z) = 2(r^2 - z^2) \tag{4.1.16}$$

$$f_{axi}(r,z) = -4\sigma \tag{4.1.17}$$

and for the three-dimensional case

$$V_{3D}(x,y,z) = 2(x^2 + y^2 - z^2) \tag{4.1.18}$$

$$f_{3D}(x,y,z) = -4\sigma \tag{4.1.19}$$

where we used $r^2 = x^2 + y^2$. The solutions are calculated on basis functions of degree 2, this way both solutions should be exact and can be compared. Then, the line $z = 1 - r$ from both results is compared, and a maximum difference is established. The result is shown in 20. In particular, figure 20(a) shows the solution of the three-dimensional solver. In this case, a cut has been made along the x and y-axis to expose the z, x-, and z, y-planes. Since the model is axisymmetric, these will have the same values as the z, r-plane. The dashed-line of both the z, y-plane (outlined in black) and the solution of the axisymmetric solver, in figure 20(b), are then compared. The resulting error-norms and maximum point-wise difference are given in table 8.

From this table, it is seen that in both cases the exact solution is retrieved and that the three-dimensional formulation of an axisymmetric model yields the same results, i.e., all error measures are less than 1×10^{-12}.

u_{axi}		u_{3D}		
H^0	H^1	H^0	H^1	$\max |u_{3D} - u_{2D}|$
$4.69\text{x}10^{-14}$	$7.66\text{x}10^{-13}$	$2.20\text{x}10^{-14}$	$1.66\text{x}10^{-13}$	$6.68\text{x}10^{-14}$

Table 8: H^0 and H^1 error-norm results of the finite element solution of V_{axi} (eq. 4.1.16) and V_{3D} (eq. 4.1.18) respectively. Both functions are polynomials of degree two. Furthermore, the three-dimensional function is axisymmetric, and thus, can be compared to the two-dimensional, axisymmetric result. Both solvers used basis functions of degree 2, and therefore, their individual errors should be within machine precision, e.g. $< 1\text{x}10^{-12}$. The last column denotes a maximum pointwise difference between the two solutions over the line $z = 1 - r$ (see dashed line in fig. 20).
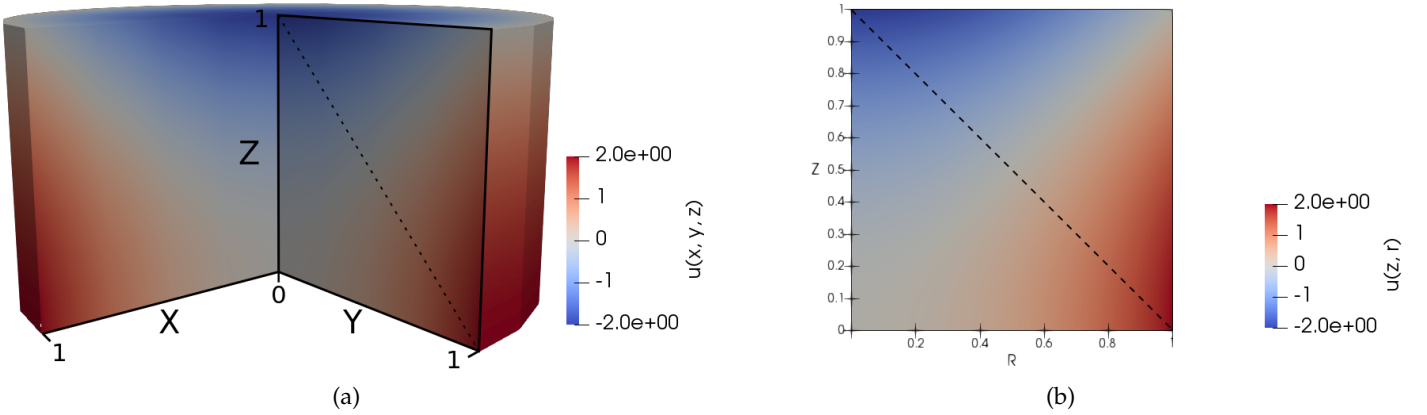
Figure 20: Results of a manufactured solutions test for the electric potential solver. (a) The three-dimensional solution (eq. 4.1.18). (b) The axisymmetric solution (eq. 4.1.16). The axisymmetric model solves the same problem as the three-dimensional model by exploiting the symmetry (z) axis. Therefore, (b) yields the same result as the z, y-plane (outlined in black) of (a). A point-wise difference is calculated between the two models over the dashed-line. Difference results are given in table 8.

4.1.4   *Pennes' bioheat solver*

Similar method of manufactured solution tests have been performed for the Pennes' bioheat solver. However, due to the time dependence, the time discretization must also be validated. An thus, in addition to the spatial convergence tests, temporal convergence tests have been performed.

4.1.4.1   *Three-dimensional spatial convergence*

Both Lees' method and the implicit Euler method are exact when the temperature depends at most linearly on time. Therefore, the spatial convergence of the solvers can be investigated by use of the manufactured solutions method, where we only use functions which are at most linearly dependent on time.

Again, we can impose any manufactured solution we want. For the results to be reproducible, we use the following polynomial of degree three.

$$T(x, y, z, t) = (x + 2y + 3z)^3 + t \tag{4.1.20}$$

However, the material properties ρ, c and k are in general temperature dependent. This gives rise to a system of non-linear equations, which require an extra step to solve (see sections 2.7.1 and 2.7.2). To test if the solver can adequately handle non-linearities, we use non-linear, manufactured functions for the material properties, e.g.

$$\rho c(T) = 1 + T^2 \tag{4.1.21}$$

$$k(T) = 1 + T^2 \tag{4.1.22}$$

Where the density, ρ, and specific heat c, are taken as one function, as they appear together in the Pennes' bioheat equation (eq. 3.5.1).

Since we are again interested in the convergence rate of the error, we will use basis functions of degree two, one degree less than the solution. Then, using equation 4.1.5, we know that the expected convergence rates are three and two for the $|e|_{H^0}$ and $|e|_{H^1}$ semi-norms respectively.

Further, since the Lees algorithm is a three-level scheme, we need two initial solutions. Therefore we test the convergence over two subsequent time steps. The convergence results for Lees' and Euler's implementation are shown in table 9 and 10 respectively. As seen in both tables, the expected convergence rates are retrieved.

4.1.4.2   *Axisymmetric spatial convergence*

The same convergence tests have been repeated for the axisymmetric implementation. In this case, we have taken a polynomial of degree three

$$T(r, z, t) = (r + 3z)^3 + t \tag{4.1.23}$$

	Linear,	t=$2\Delta t$			Non-linear,	t=$2\Delta t$		
N	H^0	r_{H^0}	H^1	r_{H^1}	H^0	r_{H^0}	H^1	r_{H^1}
2	4.26×10^{-1}	-	6.37×10^0	-	4.27×10^{-1}	-	6.37×10^0	-
4	5.33×10^{-2}	3.00	1.60×10^0	2.00	5.36×10^{-2}	2.99	1.60×10^0	2.00
8	6.66×10^{-3}	3.00	3.98×10^{-1}	2.00	6.78×10^{-3}	2.98	4.03×10^{-1}	1.99
16	8.43×10^{-4}	3.00	1.01×10^{-1}	1.98	8.64×10^{-4}	2.97	1.03×10^{-1}	1.97

Table 9: Three-dimensional Pennes' bioheat convergence rates of the finite element error of a polynomial of order three 4.1.20 using Lees' algorithm, by a polynomial of degree two after two subsequent timesteps of $\Delta t = 1$. Constant material properties lead to a linear model, whereas the non-linear variant is tested using equations 4.1.21 and 4.1.22

.

	Linear,	t=$2\Delta t$			Non-linear,	t=$2\Delta t$		
N	H^0	r_{H^0}	H^1	r_{H^1}	H^0	r_{H^0}	H^1	r_{H^1}
2	4.64×10^{-1}	-	6.37×10^0	-	4.27×10^{-1}	-	6.37×10^0	-
4	5.33×10^{-2}	3.00	1.59×10^0	2.00	5.34×10^{-2}	3.00	1.59×10^0	2.00
8	6.66×10^{-3}	3.00	3.98×10^{-1}	2.00	6.68×10^{-3}	3.00	3.99×10^{-1}	2.00
16	8.33×10^{-4}	3.00	9.95×10^{-2}	2.00	8.35×10^{-4}	3.00	9.97×10^{-2}	2.00

Table 10: Three-dimensional Pennes' bioheat convergence rates of the finite element error of a polynomial of order three 4.1.20 using the implicit Euler algorithm, by a polynomial of degree two after two subsequent time-steps of $\Delta t = 1$. Constant material properties lead to a linear model, whereas the non-linear variant is tested using equations 4.1.21 and 4.1.22

	Linear,	t=2Δt			Non-linear,	t=2Δt		
N	H^0	r_{H^0}	H^1	r_{H^1}	H^0	r_{H^0}	H^1	r_{H^1}
2	1.89×10^{-1}	-	2.61×10^0	-	2.00×10^{-1}	-	2.71×10^0	-
4	2.36×10^{-2}	3.00	6.53×10^{-1}	2.00	2.59×10^{-2}	2.95	6.91×10^{-1}	1.97
8	2.95×10^{-3}	3.00	1.63×10^{-1}	2.00	3.22×10^{-3}	3.01	1.69×10^{-1}	2.03
16	3.68×10^{-4}	3.00	4.07×10^{-2}	2.00	4.01×10^{-4}	3.00	4.14×10^{-2}	2.03
32	4.60×10^{-5}	3.00	1.02×10^{-2}	2.00	5.05×10^{-5}	2.99	1.03×10^{-2}	2.01
64	5.75×10^{-6}	3.00	2.54×10^{-3}	2.00	6.67×10^{-6}	2.92	2.56×10^{-3}	2.01

Table 11: Two-dimensional, axisymmetric, Pennes' bioheat convergence rates of the finite element error of a polynomial of order three 4.1.23 using Lees' algorithm, by a polynomial of degree two after two subsequent time-steps of $\Delta t = 1$. Constant material properties lead to a linear model, whereas the non-linear variant is tested using equations 4.1.21 and 4.1.22

.

	Linear,	t=2 Δt			Non-linear,	t=2 Δt		
N	H^0	r_{H^0}	H^1	r_{H^1}	H^0	r_{H^0}	H^1	r_{H^1}
2	1.89×10^{-1}	-	2.61×10^0	-	1.91×10^{-1}	-	2.63×10^0	-
4	2.36×10^{-2}	3.00	6.51×10^{-1}	2.00	2.38×10^{-2}	3.00	6.58×10^{-1}	2.00
8	2.95×10^{-3}	3.00	1.63×10^{-1}	2.00	2.96×10^{-3}	3.01	1.64×10^{-1}	2.01
16	3.68×10^{-4}	3.00	4.07×10^{-2}	2.00	3.69×10^{-4}	3.00	4.08×10^{-2}	2.00
32	4.60×10^{-5}	3.00	1.02×10^{-2}	2.00	4.60×10^{-5}	3.00	1.02×10^{-2}	2.00
64	5.75×10^{-6}	3.00	2.54×10^{-3}	2.00	5.75×10^{-6}	3.00	2.54×10^{-3}	2.00

Table 12: Two-dimensional, axisymmetric, Pennes' bioheat convergence rates of the finite element error of a polynomial of order three 4.1.23 using the implicit Euler algorithm, by a polynomial of degree two after two subsequent time-steps of $\Delta t = 1$. Constant material properties lead to a linear model, whereas the non-linear variant is tested using equations 4.1.21 and 4.1.22

.

And have taken the same form for the non-linear material properties as in equations 4.1.21 and 4.1.22. The results for Lees' and the implicit Euler implementation is shown in table 11 and 12 respectively.

Since the solution is of degree three, we take basis functions of degree two. The three-dimensional test also used basis functions of degree two, and as such, we expect the same convergence rates for this test. And indeed, the tables show the correct convergence rates, three and two for the $|e|_{H^0}$ and $|e|_{H^1}$ semi-norms respectively. Furthermore, we see that for the linear case, both implementations return the exact same result. Whereas for the non-linear case there is a slight difference. This is to be expected due to the difference in the evaluation of the non-linearities.

	Backwards Euler				Lees			
N	ϵ	r_ϵ	E	r_E	ϵ	r_ϵ	E	r_E
4	$2.96\mathrm{x}10^{-2}$	-	$1.41\mathrm{x}10^{-1}$	-	$1.73\mathrm{x}10^{-2}$	-	$3.80\mathrm{x}10^{-2}$	-
8	$7.55\mathrm{x}10^{-3}$	1.97	$7.20\mathrm{x}10^{-2}$	0.97	$2.05\mathrm{x}10^{-3}$	3.08	$9.34\mathrm{x}10^{-3}$	2.02
16	$1.92\mathrm{x}10^{-3}$	1.98	$3.64\mathrm{x}10^{-2}$	0.99	$2.50\mathrm{x}10^{-4}$	3.03	$2.32\mathrm{x}10^{-3}$	2.01
32	$4.83\mathrm{x}10^{-4}$	1.99	$1.83\mathrm{x}10^{-2}$	0.99	$3.08\mathrm{x}10^{-5}$	3.02	$5.76\mathrm{x}10^{-4}$	2.01
64	$1.21\mathrm{x}10^{-4}$	1.99	$9.16\mathrm{x}10^{-3}$	1.00	$3.83\mathrm{x}10^{-6}$	3.01	$1.44\mathrm{x}10^{-4}$	2.00
128	$3.04\mathrm{x}10^{-5}$	2.00	$4.58\mathrm{x}10^{-3}$	1.00	$4.78\mathrm{x}10^{-7}$	3.00	$3.59\mathrm{x}10^{-5}$	2.00
256	$7.62\mathrm{x}10^{-6}$	2.00	$2.29\mathrm{x}10^{-3}$	1.00	$5.97\mathrm{x}10^{-8}$	3.00	$8.97\mathrm{x}10^{-6}$	2.00
512	$1.91\mathrm{x}10^{-6}$	2.00	$1.15\mathrm{x}10^{-3}$	1.00	$7.46\mathrm{x}10^{-9}$	3.00	$2.24\mathrm{x}10^{-6}$	2.00

Table 13: Temporal convergence of the implicit Euler and Lees method w.r.t halving the time step size, i.e., $\Delta t = 1/N$. The local truncation error and its convergence is denoted by ϵ and r_ϵ respectively. Similar, the global error and its convergence is denoted by E and r_E respectively.

.

4.1.4.3 *Temporal convergence*

The temporal convergence of the backward Euler method and Lees' can be investigated by considering the manufactured solution to be time dependent. By considering a function that is solely dependent on time, we can use the same function for both the axisymmetric as the three-dimensional solver.

$$T(t) = e^t \tag{4.1.24}$$

Both the local, ϵ, as the global, E, convergence rates have been investigated. From equations 2.7.12, 2.7.8 and 3.7.14 we have

$$\epsilon_{\mathtt{Euler}} = O(\Delta t^2), \quad \epsilon_{\mathtt{Lees}} = O(\Delta t^3) \tag{4.1.25}$$

$$E_{\mathtt{Euler}} = O(\Delta t), \quad E_{\mathtt{Lees}} = O(\Delta t^2) \tag{4.1.26}$$

The convergence tests have been performed by doubling the number of steps, $N = 1/\Delta t$, each iteration. Then the error was determined at the first step, to determine the local truncation error and the last step for the global truncation error. The end time was set at $t = 1s$. The axisymmetric solver and thee dimensional solver results are shown in table 13. Again, the solvers show their expected convergence behavior.

4.2 ANALYTICAL SOLUTIONS TO SPECIFIC PROBLEMS

In this section, we validate the model implementation by solving physical problems for which we can derive an analytical solution.
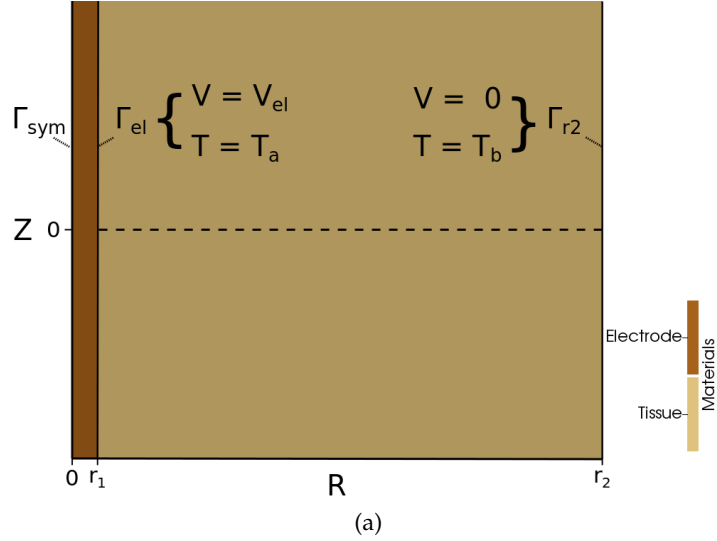
(a)

Figure 21: An axisymmetric two-dimensional model for the semi-infinite electrode test. The symmetry-axis is denoted by Γ_{sym}. Voltage and temperature boundary conditions are imposed on the electrode surface denoted by Γ_{el}. Likewise for the outer boundary Γ_{r2}. The dashed line represents the line (r, z=0), and will be used to plot the temperature distribution (see figure 22).

4.2.1 *The semi-infinite electrode*

For this problem we consider the model presented in figure 21. It is an axisymmetric model, which has a semi-infinite electrode, that is to say, the electrode will be long enough such that the effect of the top and bottom boundaries will be negligible.

The electric potential, subsequent source term, and heat equation will all only depend on r. Since we can find an analytical solution for all of these terms, we can test the interaction between the electric potential solver and Pennes' bioheat solver. The simulation should, in the end, produce a temperature distribution equal to the analytical solution.

We can solve the electric potential (equation 3.4.3) equation exactly if one applies a voltage $V = V_{el}$ to the semi-infinite long electrode at $\Gamma_{el}(r = r_1)$, and a ground $V = 0$ at $\Gamma_{r_2}(r = r_2)$. Furthermore, we take σ as being constant. Then

$$\frac{\sigma}{r}\frac{d}{dr}r\frac{d}{dr}V(r) = 0 \qquad (4.2.1)$$

Which, after moving the constants around and integrating leads to

$$V(r) = C_1 \ln(r) + C_2 \qquad (4.2.2)$$

using our boundary conditions, i.e.

$$V(r_1) = V_{el}, \quad V(r_2) = 0 \qquad (4.2.3)$$

we can solve for C_1 and C_2. Doing so yields

$$C_1 = \frac{V_{el}}{\ln(\frac{r_1}{r_2})} \tag{4.2.4a}$$

$$C_2 = -\frac{V_{el}}{\ln(\frac{r_1}{r_2})}\ln(r_2) \tag{4.2.4b}$$

substituting the above into equation 4.2.2 we end up with

$$V(r) = \frac{V_{el}}{\ln(\frac{r_1}{r_2})}\ln(\frac{r}{r_2}) \tag{4.2.5}$$

Further, we have

$$Q_{RF} = \sigma E \cdot E \tag{4.2.6a}$$

$$E = -\nabla V \tag{4.2.6b}$$

Using the above we find an expression for the generated heat source

$$Q_{RF} = \frac{\sigma V_{el}^2}{(\ln(\frac{r_1}{r_2}))^2}\frac{1}{r^2} \tag{4.2.7}$$

Now we want to find the temperature distribution due to the above source term. For this, we consider the steady state of the Pennes' bio-heat equation (equation 3.5.1), i.e. $\frac{dT}{dt} = 0$, were we take the thermal conductivity k as a constant and ignore the perfusion term, i.e $w = 0$. Due to symmetry, there is only a r dependence.

$$-Q_{RF} = \frac{k}{r}\frac{d}{dr}r\frac{d}{dr}T(r) \tag{4.2.8}$$

Substituting equation 4.2.7 in the above expression, rearranging the terms and performing integration yields

$$T(r) = \frac{A}{2}\ln^2(r) + C_1\ln(r) + C_2 \tag{4.2.9}$$

where we used

$$A = -\frac{V_{el}^2}{\ln^2(\frac{r_1}{r_2})}\frac{k}{\sigma} \tag{4.2.10}$$

We can solve equation 4.2.9 for its constants C_1, C_2 by setting temperature boundary conditions at Γ_{el} where we set $T(r_1) = T_a$, and Γ_{r_2} where $T(r_2) = T_b$. We then find

$$C_1 = \frac{1}{\ln(\frac{r_2}{r_1})}(T_b - T_a - \frac{A}{2}\ln(\frac{r_2^2}{r_1^2})) \tag{4.2.11}$$

$$C_2 = T_a - \frac{A}{2}\ln(r_1^2) - C_1\ln(r_1) \tag{4.2.12}$$

Substituting the above coefficients into equation 4.2.9 yields the analytical solution for the steady state problem.
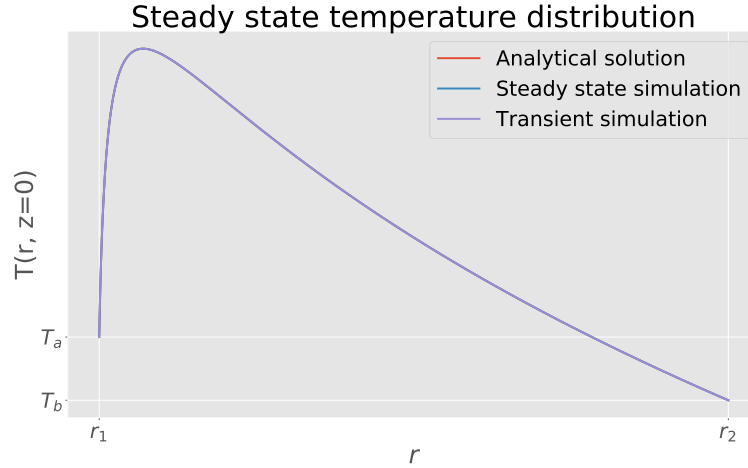
Figure 22: The analytical (equation 4.2.9), steady state and transient to steady state solutions of the infinite electrode problem over the line $z = 0$ (see dashed line in figure 21). With $r_1 = 0.75mm$, $r_2 = 100mm$, $T_a = 6K$, $T_b = 5K$. Tissue parameters were $\sigma = 0.21(S/m)$ and $k = 0.52(W/(m \cdot K))$, corresponding to the average reported values for liver tissue [45]. Values for the difference between solution and simulation are given in table 14.

The convergence of the analytical solution has been investigated in two ways. First, a variational form of the steady-state equation has been set up, and the solution should be found after a single calculation. Second, the time-dependent equations were set to solve the equations indefinitely until the difference between succeeding solutions was less than a predefined tolerance, e.g., $1x10^{-12}$, as the temperature distribution does not change anymore and is considered to be steady-state. The line $z = 0$ was compared (see dashed line in figure 21, as it was furthest away from the opposite boundaries, and thus their effect should be negligible.

The parameters were set to $r_1 = 0.75mm$, a typical electrode thickness, $r_2 = 100mm$, $T(r_1) = 6$, $T(r_2) = 5$. The material values for the tissue were set to $\sigma = 0.21(S/m)$ and $k = 0.52(W/(m \cdot K))$, which are average reported values for liver tissue [45]. The transient to steady state solution was stopped when $|u_{n+1} - u_n| \leqslant 1x10^{-12}\Delta t$. The results are shown in table 14 and figure 22. Furthermore, a summary of the simulation parameters is given in appendix A.1.

The solutions show excellent agreement with the analytical solution, with the maximum error being 0.123%. Furthermore, as expected, we see that the transient solution converges to the same result as the steady-state problem.

Steady state		Transient	
$e_{max}(\%)$	$\bar{e}(\%)$	$e_{max}(\%)$	$\bar{e}(\%)$
$1.23\text{x}10^{-1}$	$1.01\text{x}10^{-3}$	$1.23\text{x}10^{-1}$	$1.01\text{x}10^{-3}$

Table 14: The maximum and average errors of steady state and transient to steady state solution. Both solutions converge to the same result.
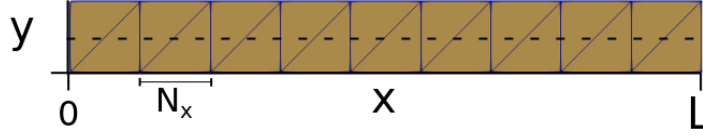

Figure 23: Geometry of the one-dimensional solidification test. N_x denotes the element length. The dashed line represents the line over which the temperature profile (see figure 24) and interface position has been calculated (see figure 26).

4.2.2 One-dimensional solidification

Since a phase change can occur throughout RF ablation, we modeled the specific heat according to the apparent heat capacity (see equation 3.5.3). To test the validity of this method, a one-dimensional *Stefan* problem has been implemented. These are phase change problems which can be solved analytically and can be used as a test case for discontinuous properties of the thermal conductivity, specific heat and density. Here we consider the freezing of water with the following material properties

$$k_l = 0.556 Wm^{-1}K^{-1}, \quad \rho_l = 1000 Kgm^{-3}, \quad c_l = 4426 JK^{-1} \quad (4.2.13)$$

$$k_s = 2.224 Wm^{-1}K^{-1}, \quad \rho_s = 1000 Kgm^{-3}, \quad c_s = 1762 JK^{-1} \quad (4.2.14)$$

where the subscript l and s denotes liquid and solid respectively.

Now consider the problem geometry seen in figure 23. It contains a slab of length L created from elements with a characteristic length of N_x. The slab is filled with water at an initial temperature, T_i above the melting point T_m, i.e. $T_i > T_m$. At time $t = 0$ we set the left boundary ($x = 0$) at a temperature, T_0, below the melting temperature, i.e. $T_0 < T_m$. Since the model is considered one-dimensional, the temperature is only dependent on t and r.

The derivation of the analytical solution is beyond the scope of this thesis. However, it can be shown, e.g. in *Heat Conduction* by Hahn

and Özisik [46], that the temperature profiles can be expressed as a function of the solidification interface position, $s(t)$.

$$T(x,t) = \begin{cases} T_0 + (T_m + T_0)\dfrac{\text{erf}(\frac{x}{2\sqrt{\alpha_s t}})}{\text{erf}(\chi)}, & x \leqslant s(t) \\[4mm] T_i + (T_m - T_i)\dfrac{\text{erfc}(\frac{x}{2\sqrt{\alpha_l t}})}{\text{erfc}(\chi\sqrt{\frac{\alpha_s}{\alpha_l}})}, & x > s(t) \end{cases}$$

(4.2.15)

where

$$\alpha_s = \frac{k_s}{\rho_s + c_s}, \quad \alpha_l = \frac{k_l}{\rho_l + c_l}$$

(4.2.16)

and

$$s(t) = 2\chi\sqrt{\alpha_s t}$$

(4.2.17)

And χ is the root of the following transcendental equation

$$\frac{e^{-(\chi^2)}}{\text{erf}(\chi)} + \frac{k_l}{k_s}\sqrt{\frac{\alpha_s}{\alpha_l}}\frac{T_m - T_i}{T_m - T_0}\frac{e^{-(\chi^2)\frac{\alpha_s}{\alpha_l}}}{\text{erfc}(\chi\sqrt{\frac{\alpha_s}{\alpha_l}})} - \frac{\chi\sqrt{\pi}}{c_s(T_m - T_0)}L_{\text{fusion}} = 0$$

(4.2.18)

Where L_{fusion} is the latent heat of fusion. For water $L_{\text{fusion}} = 333\text{x}10^3 \text{JKg}^{-1}$. Using the above expressions, the temperature profile at a time, t, can be analytically determined.

Three parameters are checked for convergence. First, the error in the temperature profile at $t = 10, 30\,50$h of the simulation has been calculated by taking the profile along the dashed line in figure 23. The maximum of these errors is denoted ϵ_T. Second, the maximum error of the position of the phase-change front during the simulation, ϵ_s. This parameter is calculated by finding the distance from $x = 0$ to the point where $T = T_m$, along the dashed line in figure 21. Last, the error in the temperature profile over time at a fixed-point in the mesh during the simulation was calculated and denoted ϵ_r.

Solidification is a rather slow process. To see interesting effects, the simulation has to simulate on the order of hours. To cut down on the computation time, Lees' algorithm has an automated time-stepping method. At each iteration, the difference between u_{n+1} and u_n is evaluated. If it is lower than a certain threshold τ_l, the time step size is doubled. On the other hand, if it is it higher than another threshold τ_u, u_{n+1} is disregarded, and the step size is halved. The two tolerances have to be different to prevent the algorithm from indefinitely changing its step size.

The convergence has been investigated by changing τ_u, τ_t and ΔT, the temperature-interval over which the phase change occurs (see equation 3.5.4), i.e. $2\Delta T = T_u - T_l$ where T_u and T_l are the upper and lower temperatures over which phase change occurs. Specific to this problem, the thermal conductivity has been defined as also changing linearly over ΔT as in equation 3.5.3.

τ_l	$\Delta T = 1$			$\Delta T = 0.5$		
	$\max|\epsilon_T|$ (°C)	$\max|\epsilon_s|$ (m)	$\max|\epsilon_r|$ (°C)	$\max|\epsilon_T|$ (°C)	$\max|\epsilon_s|$ (m)	$\max|\epsilon_r|$ (°C)
ΔT	$3.57\text{x}10^{-1}$	$4.20\text{x}10^{-3}$	$4.99\text{x}10^{-1}$	$1.22\text{x}10^{-1}$	$2.05\text{x}10^{-3}$	$3.52\text{x}10^{-1}$
$\frac{1}{2}\Delta T$	$1.13\text{x}10^{-1}$	$1.62\text{x}10^{-3}$	$2.71\text{x}10^{-1}$	$8.67\text{x}10^{-2}$	$1.09\text{x}10^{-3}$	$3.22\text{x}10^{-1}$
$\frac{1}{4}\Delta T$	$7.94\text{x}10^{-2}$	$8.87\text{x}10^{-4}$	$2.91\text{x}10^{-1}$	$8.13\text{x}10^{-2}$	$5.35\text{x}10^{-4}$	$2.24\text{x}10^{-1}$
$\frac{1}{8}\Delta T$	$9.25\text{x}10^{-2}$	$6.73\text{x}10^{-4}$	$1.98\text{x}10^{-1}$	$8.26\text{x}10^{-2}$	$2.69\text{x}10^{-4}$	$7.35\text{x}10^{-2}$
$\frac{1}{16}\Delta T$	$9.33\text{x}10^{-2}$	$5.91\text{x}10^{-4}$	$1.35\text{x}10^{-1}$	$3.41\text{x}10^{-2}$	$3.93\text{x}10^{-4}$	$5.09\text{x}10^{-2}$

Table 15: Error dependence of decreasing tolerance level and different phase change intervals.

The tests have been performed on a two-dimensional rectangular mesh of L = 1 meter, consisting of 1024 nodes, i.e. $N_x = 1/1024$. The size of this domain was large enough for there to be no effect from the boundary at $x = L$, over a simulated time of t = 50h. The range of phase change was considered to be from $T_m - \Delta T$ to $T_m + \Delta T$. The initial temperature was set to be $T_i = 20$ and the temperature at L = 0 was $T_0 = -10$. The probe was set at r = 0.05. Further, the upper tolerance was set to be $\epsilon_u = 2\epsilon_l$. The results are shown in table 15 and figures 24, 25, 26. Furthermore, a summary of simulation parameters is given in appendix A.2.

The results are in excellent agreement with theory, with all errors being less than 1% at all times. Further, it appears that the error is not very sensitive to the phase change interval ΔT, achieving similar results for $\Delta T = 1$ as $\Delta T = 0.5$, as long as a time step size is taken which is smaller than the interval. In particular, setting the lower time step tolerance to $1/4\Delta T$, yield acceptable results. Since the phase change interval was defined as $2\Delta T = T_u - T_l$, the step size was allowed to increase when at least eight steps are taken in the phase change regime.

4.3 VERIFICATION BY EXPERIMENTS

In this section, we verify the implementation of our model by comparing simulation results against experimental data and simulations performed by other groups. This final group of tests allows us to compare the use of the whole model against other results.

4.3.1 *RF ablation of Osteoma Osteoide*

RF ablation has been successfully applied to the treatment of osteoid osteoma (OO), a small benign tumor found within the bone [47] [48]. However, extra care must be taken when the tumor is located close to critical tissue such as nerves and joints.
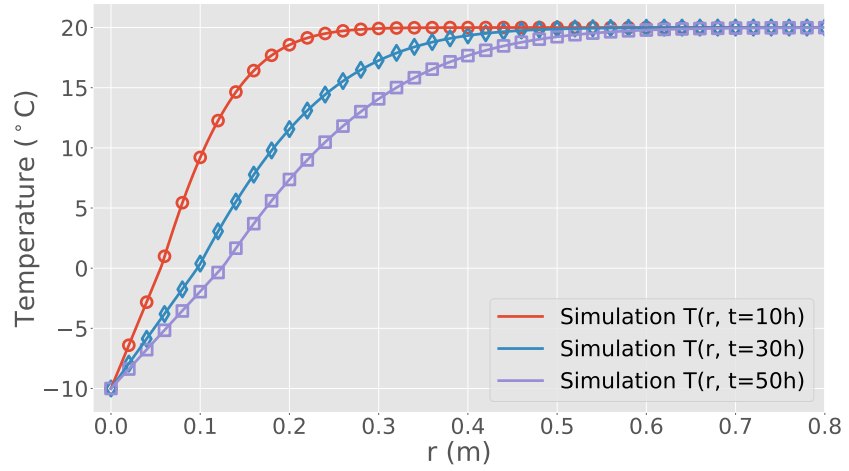
Figure 24: Analytical and simulated solution of the temperature profile at $t = 10, 30\,50\text{h}$ in red, blue and purple respectively. The similar colored markers along each line denote the analytical solution. $\Delta T = 0.5$, $\tau_l = (1/4)\Delta T$

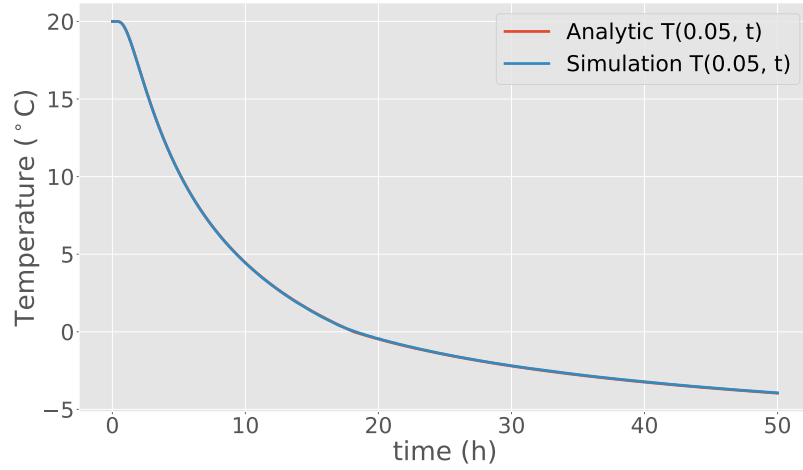

Figure 25: Analytical and simulated solution of the temperature at $r = 0.05$ over time. $\Delta T = 0.5$, $\tau_l = (1/4)\Delta T$
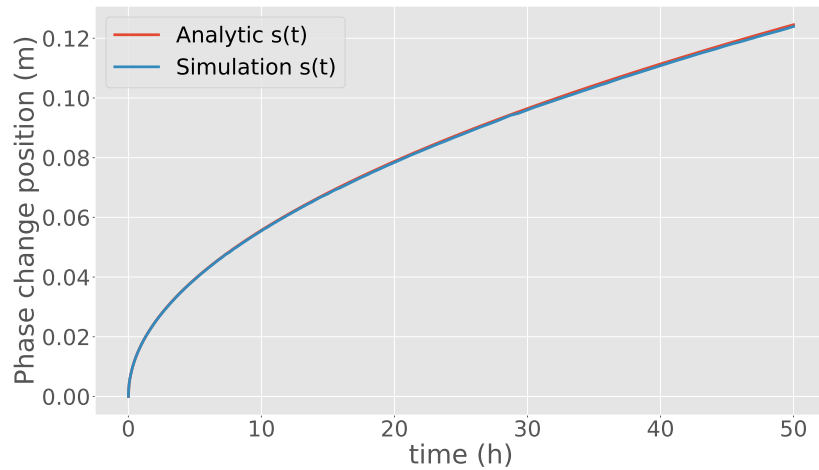

Figure 26: Analytical and simulated solution of the distance of the phase change front over time. $\Delta T = 0.5$, $\tau_l = (1/4)\Delta T$
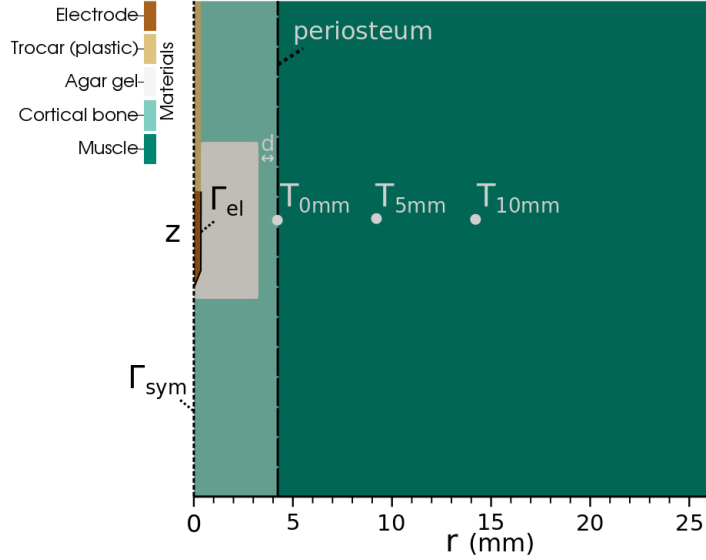
Figure 27: Theoretical model of the experimental setup found in Bitsch et al.[49]. The model is a two-dimensional axisymmetric model. The symmetry-axis is denoted by Γ_{sym} and the electrode surface by Γ_{el}. In this model the width of the periosteum, d, is changed to 1, 3, and 5 mm. Then, the temperature is measured at T_{0mm}, T_{5mm} and T_{10mm}, which are located 0, 5 and 10mm from the periosteum respectively. The same model was also simulated by Irastorza et al.[28].

To asses the temperature distribution of RF ablation during treatment of OO, Bitsch et al. [49] performed ablation on bovine tibial bones. Frozen specimens were taken where the tumor was modeled by drilling a cavity in the bone of 8mm in height and 6.6mm in diameter. Then, the hole was filled with 0.8% agarose gel, a spongy-like substance, to model the histology associated with these kinds of tumors. The cavity was either placed $d = 1, 3, 5$mm from the periosteum (see figure 27). Subsequently, the specimen was placed in a controlled bath with a physiologic NaCl solution at 37°C. The ablation was performed when the internal temperature reached 35 °C. Thermocouples were placed at the periosteum, and 5 and 10 millimeters away from the periosteum respectively.

Further, the group of Irastorza et al. [28] performed simulations of this experimental setup, providing us benchmarks against other simulation software as well as experimental values. To this end, we replicated the theoretical model of Irastorza et al. as an axisymmetric, two-dimensional model as shown in figure 27.

Considering the uncertainties in the material parameters, Irastorza et al. performed multiple simulations to determine a best fit to the experimental data of Bitsch et al. Here we only consider these best fit parameters, which are shown in table 16.

	Extracted from [28]				
	Cortical bone	Muscle	Agar gel	Electrode	Trocar (plastic)
$\rho\,(\mathrm{Kgm^{-3}})$	1500	1000	1000	6450	70
$\sigma\,(\mathrm{Sm^{-1}})$	0.022	0.446	0.4	$1.2\mathrm{x}10^{6}$	$1\mathrm{x}10^{-5}$
$c\,(\mathrm{Jkg^{-1}K^{-1}})$	1026	2824	4107	840	1045
$k\,(\mathrm{Wm^{-1}K^{-1}})$	0.3	0.52	Eq. 4.3.1	18	0.026

Table 16: Optimal material parameters for the model of Bisch et al. (fig. 27).

Furthermore, a change in the electrical conductivity of $1.5\%{}^{\circ}\mathrm{C}^{-1}$ was considered. The following polynomial modeled the thermal conductivity of agar gel

$$k_{agar} = -8\mathrm{x}10^{-1}C + 1.5\mathrm{x}10^{-3}T + 1.63\mathrm{x}10^{-1} \qquad (4.3.1)$$

where T is the temperature (K) and C is the concentration of the agar gel (0.8%).

The thermal conductivity of the other biological tissues was assumed to change with $0.003\mathrm{K}^{-1}$. Perfusion was excluded from the simulations, as the experiments were performed in an ex-vivo environment.

Electrode and trocar properties were not mentioned in Irastorza et al. Bitsch et al. used a conventional monopolar needle electrode (TCM 101; Stryker Leibinger, Freiburg, Germany)[49], which produces Nitinol electrodes, a nickel-titanium alloy, of 18, 20 and 22 gauge[50]. Simulations were performed with all three sizes, and the 22 gauge electrode was determined to be the best fit.

Bitsch et al. followed an ablation protocol of 400 seconds using a set target temperature of 95 °C. Here, and in Irastorza et al., we used a PI control as described in section 3.3.2 to mimic the automated temperature control. The PI parameters were set to $k_p = 1.15$, $k_i = 0.06$. Subsequently, the electrical boundary conditions were a voltage, V_{el}, provided by the PI control on the electrode boundary (Γ_{el} in figure 27), zero current density on the axis of symmetry (Γ_{sym} in figure 27), and zero voltage on the lower limit of the domain to mimic the ground-pad. The initial temperature and temperature at the boundaries away from the symmetry-axis were set to be 35 °C to model the procedure of Bitsch et al.

Convergence tests were performed to determine adequate domain and element size. The tests were similar to the ones described in Irastorza et al. However, the method of domain size convergence was not mentioned in Irastorza et al. Here we increased the domain size until the temperature at T_{0mm}, T_{5mm} and T_{10mm} was less than 0.5% between iterations. Spatial convergence was reached by refining the mesh until the difference in temperature at T_{0mm} between iterations was less than 0.5%.
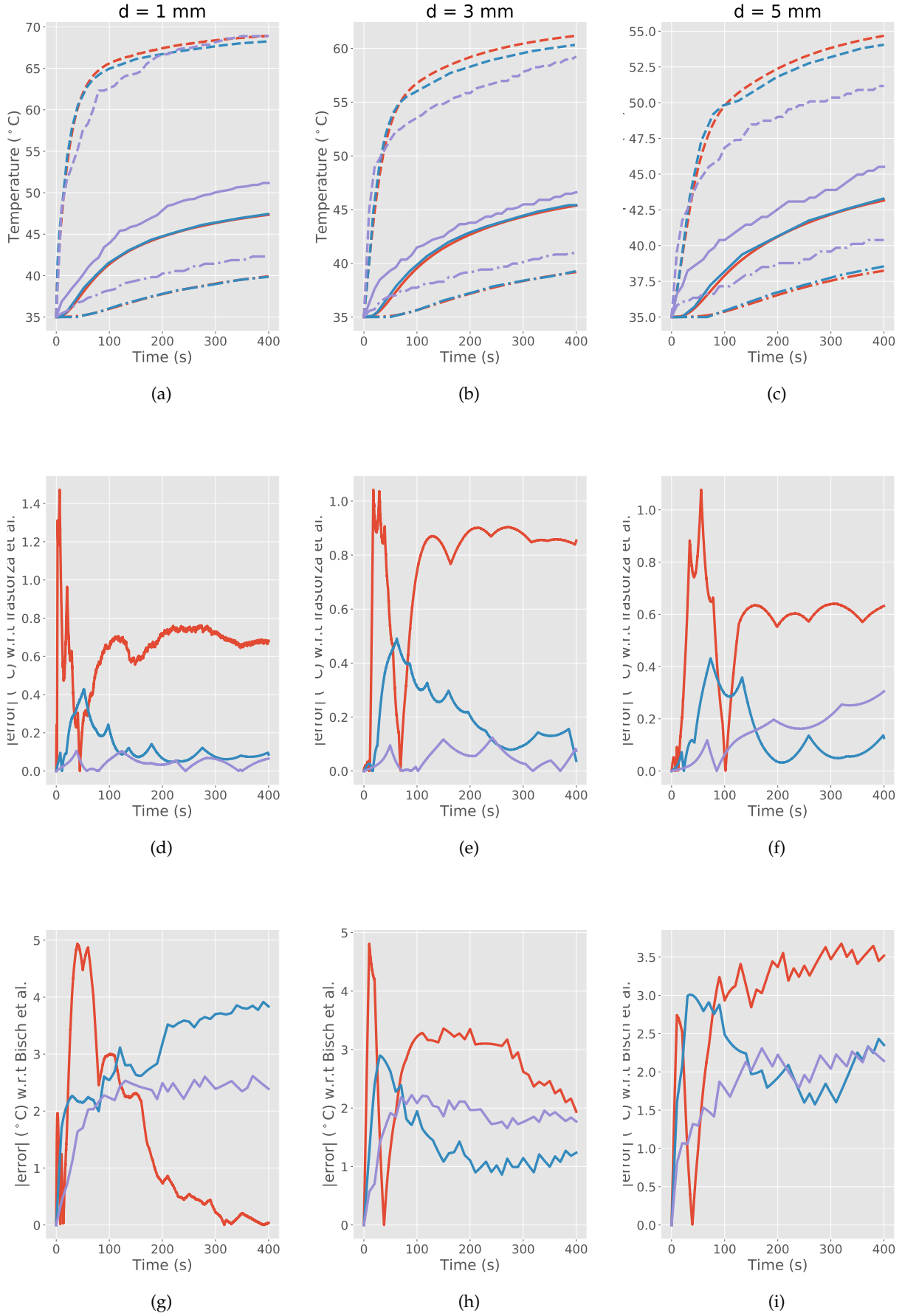
Figure 28: Temperature comparison of T_{0mm}, T_{5mm} and T_{10mm}. (a), (b), (c), shows the temperature profiles in red for our own simulation, blue from Irastorza et al.[28] and purple Bitsch et al.[49]. The dashed, full and alternating dash-dot line represent the T_{0mm}, T_{5mm} and T_{10mm} respectively. (d), (e), (f) show the absolute error in °C between our simulations and those of Irastorza et al. with in red, blue and purple the error in T_{0mm}, T_{5mm} and T_{10mm} respectively. Likewise (g), (h), (i), show the absolute error in °C between our simulations and the experimental data of Bitsch et al.

Temporal convergence was reached by changing the tolerances of the automatic time step, τ_u, τ_l, until the temperature at T_{0mm} between iterations was less than 0.5%. Since performing one convergence test considers the other parameters as constant, all three convergence tests were performed once more.

Simulations were performed by for $d = 1, 3$ and $5mm$. The results are shown in figure 28. Furthermore, a summary of simulation parameters is given in appendix A.3.

We obtain similar results to Irastorza et al., especially for the probes T_{5mm} and T_{10mm} which are within 0.5 °C at all times.

Higher differences in the T_{0mm} probe were expected as the models are different due to the limited information of the model presented in Irastorza et al. Still, the T_{0mm} probe is within 1 °C for most of the simulation, differing only in the initial heating period $t \leqslant 50s$.

Further, compared to the experimental data of Bitsch et al. we found that the maximum error achieved was around 5 °C, one degree less than reported in Irastorza et al. This error only occurred during the principle heating part, $t \leqslant 50s$. At all other times, we found the same level of accuracy as Irastorza et al. with the error being between 5 and 8%.

4.3.2 *RF ablation in cortical osteoid osteoma*

Most OOs consist of a nidus of active bone surrounded by a reactive zone which is histologically similar to dense reactive sclerotic bone. Further, the reactive zone is surrounded by cancellous or trabecular bone, which in turn has a cortical outer layer. The bone is surrounded by muscle. The reactive zone has been hypothesized to play an essential part in RF ablation as it acts as a thermal insulator. Irastorza et al. performed various simulations of OOs containing such a reactive zone [7]. The geometry of this model has been replicated for model verification purposes, see figure 29.

Among other things, Irastorza et al. investigated the temperature profile at the end of the simulation along the r-axis from the middle of the electrode surface for varying thicknesses of the reactive zone. The thickness of the reactive zone took on values of $t = 2.5, 5$ and 7.5 mm. The material properties are summarized in table 17.

The nidus is associated with having a high perfusion rate as is apparent from table 17. Irastorza et al. modeled the perfusion with a temperature cut-off of 50 °C, i.e., the β-term of the perfusion equation (see eq. 3.5.5) is modeled as

$$\beta = \begin{cases} 1, & T \leqslant 50°C \\ 0, & T > 50°C \end{cases} \tag{4.3.2}$$

A PI control scheme regulated the temperature in the simulation. In particular, the protocol entailed an ablation period of 300s by a
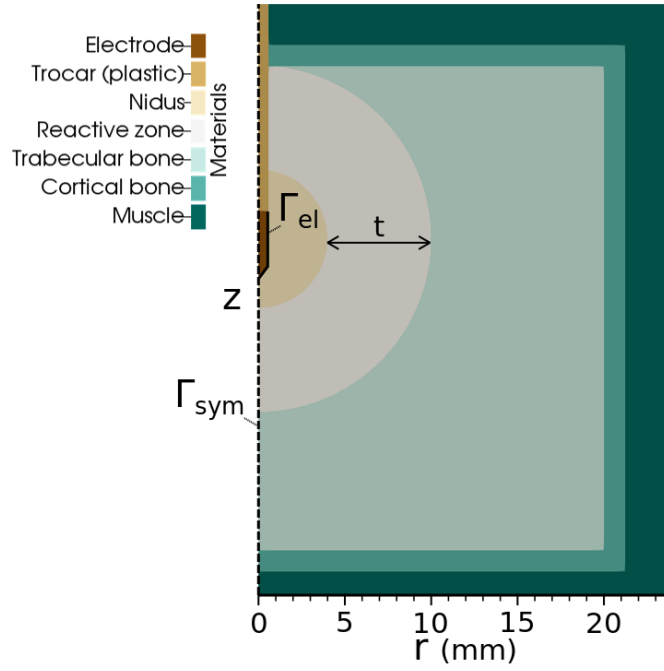
Figure 29: Two-dimensional, axisymmetric model of cortical osteoid osteoma adapted from Irastorza et al.[7]. Γ_{sym} and Γ_{el} denote the symmetry boundary (z axis) and electrode boundary respectively. t denotes the thickness of the reactive zone, which in this study, took on the values of t = 2.5, 5 and 7.5 mm.

monopolar 17-gauge electrode with a set target temperature of 90 °C. The internal parameters K_p, K_i of the PI controller were set to 1.15 and 0.06 respectively.

Convergence tests were performed to determine adequate domain and element size. The convergence was tested by measuring the temperature profile at the end of ablation along the $r - axis$ from the middle of the electrodes surface.

The boundary conditions were a voltage set by the PI control on the electrode surface and zero voltage at the lower boundary to mimic the ground pad. The initial temperature and temperature at boundaries away from the symmetry-axis was set to be 37 °C. An insulating Neumann condition was set at the symmetry-axis.

Convergence tests have been performed to determine adequate domain, spatial and temporal parameters. Domain size convergence was reached by increasing the domain size until the temperature profile differed less than 0.5% between iterations. Spatial convergence was reached by refining the mesh until the temperature profile between iterations differed less than 0.5%. Temporal convergence was reached by changing the tolerances of the automatic time step, τ_u, τ_l, until the temperature profile between iterations differed less than 0.5%. Since performing one convergence test considers the other parameters as constant, all three convergence tests were performed once more.

	$\rho(\mathrm{Kg m^{-3}})$	$\sigma(\mathrm{S m^{-1}})$	$c\ (\mathrm{Jkg^{-1}K^{-1}})$	$k\ (\mathrm{W\ m^{-1}K^{-1}})$	$\omega(\mathrm{x10^{-4}s^{-1}})$
Cortical bone	1908	0.022	1026	0.30	0
Trabecular bone	1178	0.087	2274	0.31	5.9
Nidus	1046	0.29	2726	0.56	48
Reactive zone	1908	0.0535	1026	0.3	2.95
Muscle	1090	0.446	2824	0.52	6.7
Electrode	6450	10^8	840	18	0
Trocar	70	10^{-5}	1045	0.026	0
Blood	1046	-	3639	-	-

Table 17: Material properties measured at 37 °C. All data extracted from Irastorza et al.[7]
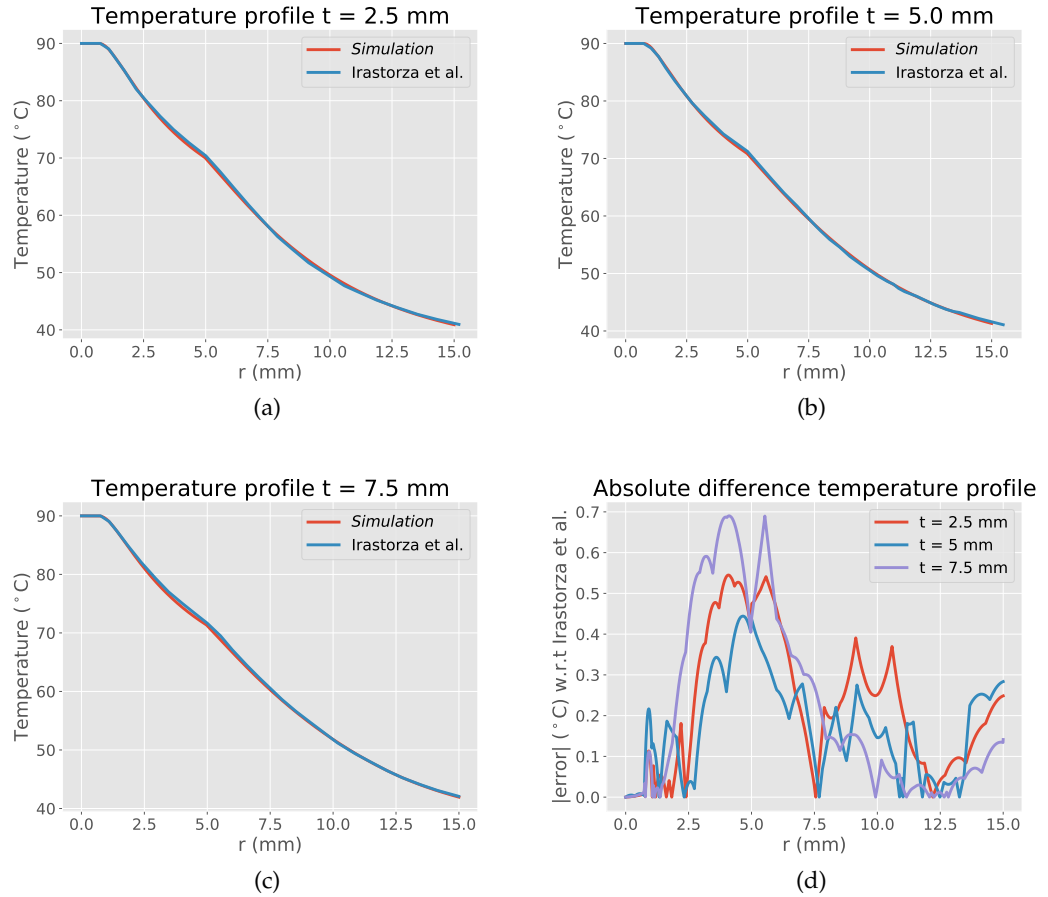

Figure 30: Temperature profile comparison for various reactive zone thicknesses.(a), (b), (c) shows temperature profiles of a reactive zone of thickness t = 2.5, 5 and 7.5 respectively. In (d) the absolute difference between our simulation and Irastorza et al. is shown.

The results are shown in figure 30. Furthermore, a summary of simulation parameters is given in appendix A.4. The differences in temperature profiles can be attributed to the limited information of the actual geometry provided by Irastorza et al., a different time-step algorithm used and different convergence criteria. Nevertheless, excellent agreement is reached between our simulations and those of Irastorza et al. with the temperature profiles being within 0.7 °C or 1% at all times.

4.3.3   *Verification of the three-state cell death model*

The three-state cell death required the implementation of nonlinear coupled PDE's. As such, the model has been verified by replicating the fits to the data of the original paper of O'Neill et al. [39]. O'Neill et al. heated cell-cultures at $55, 65, 75, 85$ and 100°C with heating times of $300, 600$ and, 900 seconds. Subsequently, the heating medium was replaced with a medium at 37 °C. Then fluorescence was measured at $2, 26$ and 50 hours after incubation, which is taken as a direct correlation of cell viability. The experimental data of O'Neill et al. is shown in table 18.

The cell death model parameters have been found by performing an optimal fit to the two hours post-heating cell viability data. The results for different cell co-cultures have been previously stated in table 2 and in particular, parameters for an average culture fit were determined to be

$$\bar{k}_f = 3.33 \times 10^{-3} s^{-1}, \quad k_b = 7.77 \times 10^{-3} s^{-1}, \quad T_k = 40.5°C \quad (4.3.3)$$

with a root mean square (RMS) error of 1.40% [39].

Further, the slow cell death model parameters, equation 3.5.17, have been found by performing an optimal fit to all the experimental data points, where the RMS error was found to be 2.80%

Simulations have been performed on a unit square mesh for the different heating times and temperatures. To validate the cell death model, the RMS error of the cell viability at the end of ablation w.r.t the 2h post-heating viability was calculated. The results are shown in figure 31. Furthermore, a summary of simulation parameters is given in appendix A.5. The RMS error was calculated to be 1.40%, as in O'Neill et al.

After ablation, the model switched over to the slow cell death model. To validate the slow cell death model, the RMS error of the cell viability at all the experimental data points has been calculated. The results are shown in figure 32. The RMS error was calculated to be 2.80%, as in O'Neill et al.

Heating time (s)	Heating temperature (°C)	Post-heating incubation (h)		
		2	26	50
300	37	100.0	100.0	100.0
	55	100.0	98.02	98.02
	65	100.0	98.02	98.02
	75	89.66	89.00	86.82
	85	52.89	25.48	9.56
	100	4.23	1.00	0.00
600	37	100.0	100.0	100.0
	55	94.71	83.75	83.75
	65	56.94	22.33	13.38
	75	7.89	1.47	1.47
	85	2.45	0.00	0.00
	100	1.19	0.00	0.00
900	37	100.0	100.0	100.0
	55	66.99	53.80	10.61
	65	10.75	1.33	1.65
	75	2.56	0.00	0.00
	85	2.51	0.00	0.00
	100	0.00	0.00	0.00

Table 18: Experimental cell viability data for the three-state model. Extracted from O'Neill et al. [39].
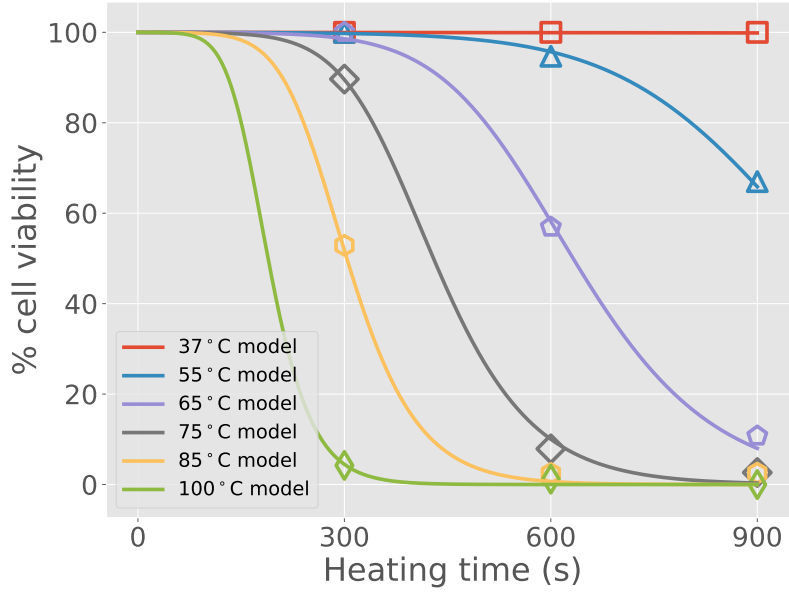
Figure 31: Validation of the cell death model with parameters shown in equation 4.3.3. The continuous lines represent the model prediction whereas the experimental data are discrete points. The RMS error was found to be 1.40% as in [39]
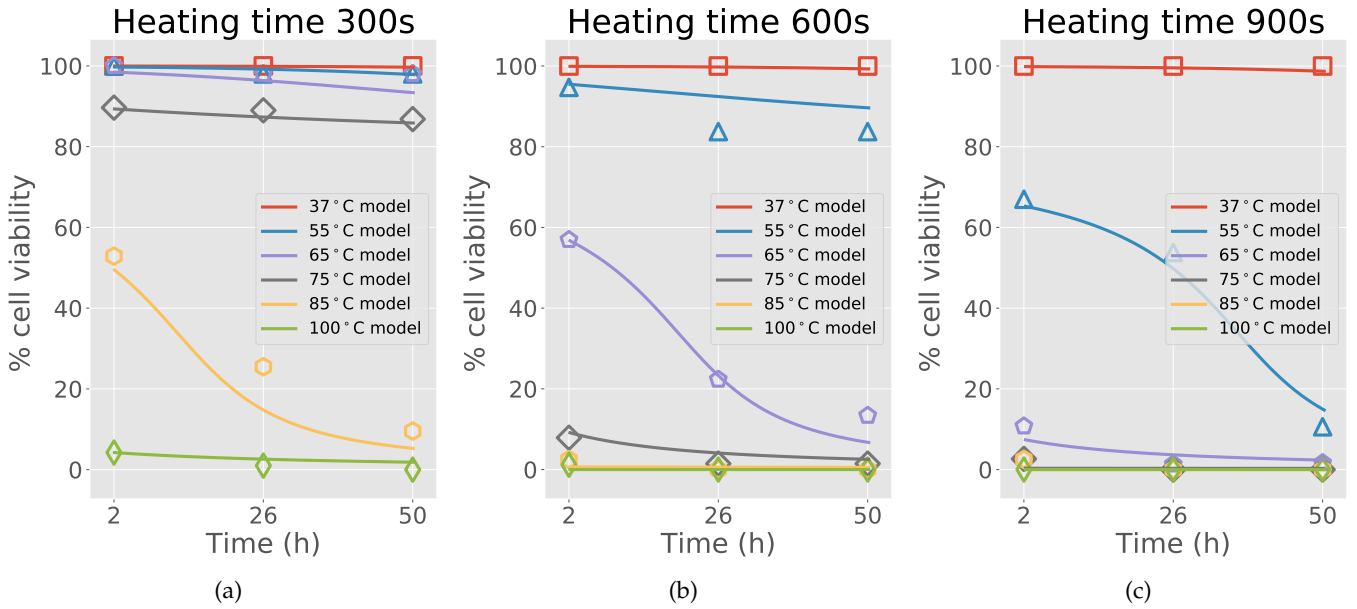

Figure 32: Validation of the slow cell death model. Continuous lines represent the model prediction whereas the experimental data is represented by discrete points. (a) heating time of 300s. (b) heating time of 600s. (c) heating time of 900s. The RMS error was found to be 2.80% as in [39]

4.3.4   *Sensitivity analysis of RF ablation parameters*

Simulations of Hall et al. [45] have been replicated, as it includes the same cell death model of O'Neill et al., and uses the impedance control technique described in 3.3.3.

In the paper of Hall et al. a sensitivity analysis has been performed on RF ablation of a liver to determine the most critical parameters in the model. To this end, the authors chose the *Morris*-method for parameter screening. A global one-at-a-time sensitivity analysis where the number of runs is linear with respect to the number of parameters was investigated.

In the Morris-method, each of the k model parameters are scaled such that $x_i \in [0, 1]$. Then the parameter space is spanned by the k-dimensional hypercube over which the parameters are varied. Subsequently, the parameter space is discretized to a grid with equally spaced points $\Delta x = 1/(l-1)$ where l is the number of grid points from which random sets of parameters can be sampled.

The method works by choosing a random starting point, x, in the parameter space with simulation output of $y(x)$. Then a random step is taken with $\pm \Delta x$, by changing a random parameter. This results in a new set of parameters x_ϵ with simulation output $y(x_\epsilon)$. Then an elementary effect due to the change of this parameter can be computed by

$$E_\epsilon = \frac{y(x) - y(x_\epsilon)}{\Delta x} \qquad (4.3.4)$$

This is repeated by changing one of the remaining parameters, until an effect can be calculated for each parameter. This results in a total of $k + 1$ simulations, which form a single trajectory trough the parameter space. Multiple trajectories through the parameter space are simulated by choosing different starting locations and repeating the process as described above.

Then for each parameter, the mean and standard deviation of the elementary effect is computed. These are the sensitivity measures of the Morris-method.

The mean of the effect is a measure of the change in output by varying that parameter, whereas the standard deviation is a measure of the non-linear effects of the parameter, e.g., when a change of Δx in the parameter for each trajectory results in the same difference in the output, the standard deviation will be zero. Furthermore, it means that the change in output is unaffected by the global position, x, in the parameter space, i.e., by the values of the other parameters. On the other hand, when a change in the parameter gives rise to different elementary effects for different trajectories, the standard deviation will be non-zero, and the effect will be dependent on the global position in the parameter space. Thus it is a measure of non-linear interaction.
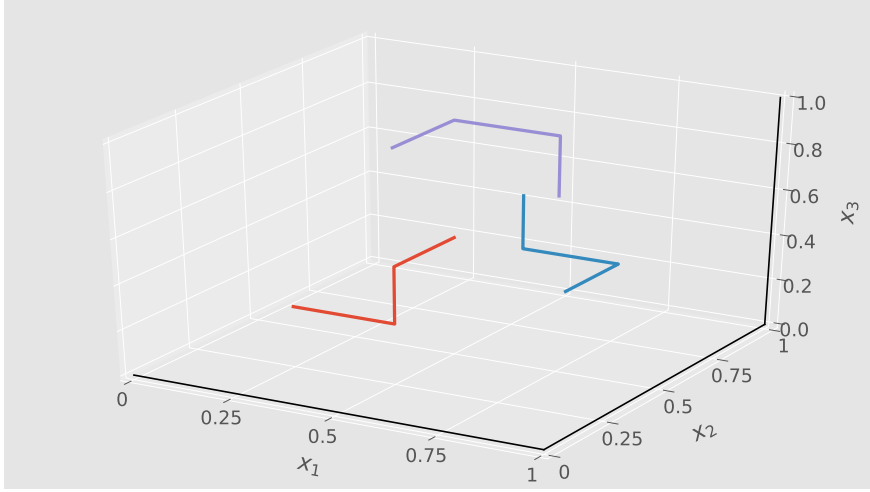
Figure 33: Parameter space of the Morris method for a model with three parameters (k=3). Three trajectories are shown in red, blue and purple respectively. Note that every trajectory has $k + 1$ points.

The model consisted of a round piece of liver, in which a 30mm long probe with a thickness of 1.5mm was placed. The electrical boundary conditions were zero voltage on the outer boundary, to mimic the ground pad and a voltage of $V_{el} = 60V$ set on the probe boundary, regulated by the impedance control. The probe was shut down for 15 seconds whenever the resistance in the mesh exceeded $R = 120\Omega$, which can be calculated according to equation 3.3.3.

Initial temperature and temperature at boundaries away from the axis of symmetry were set at 37 °C. Further, a *Cool-tip*-electrode was modeled by applying a convective heat transfer condition $h(T - 37°C)$ to the active tip. The value of h was set to $3366W/K/m^2$.

Hall et al. gathered lower and upper parameter values of twelve different parameters for the Morris method. The parameters and their values are shown in table 19.

ρc and $\rho_{vap}c_{vap}$ are the density and specific heat of normal and vaporized liver tissue respectively. The density and specific heat are grouped into one parameter as they only appear together in the Pennes' bioheat equation.

k_0 is the baseline thermal conductivity of liver and Δk the absolute increase per kelvin. The model implemented a cut-off of 100 °C above which the thermal conductivity does not increase further, as in equation 3.5.2.

σ_0 is the baseline electrical conductivity of liver and $\Delta\sigma$ a percentile increase per kelvin. To account for the sudden drop in thermal conductivity, σ_{vap}, after phase-change, the electrical conductivity has been modeled according to equation 3.4.8, where $T_l = 100$ °C and $T_u = 105$ °C.

Parameter	Units	Lower	Upper
ρc	$Jm^{-3}K^{-1}$	3.7×10^6	4.3×10^6
$\rho_{vap}c_{vap}$	$Jm^{-3}K^{-1}$	0.44×10^6	0.8×10^6
k_0	$Wm^{-1}K^{-1}$	0.47	0.57
Δk	$Wm^{-1}K^{-2}$	0	0.0033
σ_0	Sm^{-1}	0.14	0.28
$\Delta\sigma$	$\%K^{-1}$	1.0	2.0
ω_b	$Jm^{-3}K^{-1}s^{-1}$	34020	68040
C		0.71	0.76
ΔT	K	1	10
ϵ		0	1
σ_{vap}/σ		0.01	0.0001
G_0	%	70	90

Table 19: Changing parameters for the Morris method. Extracted from Hall et al. [45].

$\omega_b = \rho_{blood}c_{blood}\omega$ where ω is the liver perfusion rate. These parameters have been grouped together into one parameter as the uncertainty in ω dominates those of ρ_{blood}, c_{blood}.

C is the fraction of water content of the liver, which appears in the equation of apparent heat 3.5.3.

$\Delta T = T_u - T_l$ is the range over which the phase-change takes place. Hall et al. set $T_u = 100°C$ and varied T_l through ΔT.

ϵ determines the co-culture cell make-up by interpolating on the values found in table 2, and returning intermediate values. A value of $\epsilon = 0$ corresponds to a pure HepG2 culture. Similarly, a value of 1 corresponds to a pure MIRC-5 culture.

G_0 determines the cut-off value for cell viability below which a cell is considered dead. This threshold is also used to determine the area of cell death as well as the perfusion cut-off value.

The parameter space has been discretized into an evenly spaced grid of $l = 4$ points. Six trajectories have been simulated in this parameter space resulting in 78 simulations. A summary of simulation parameters is given in appendix A.6. The results are shown in figure 34 on a 2D scatter plot with their mean values on the x-axis and the standard deviation on the y-axis. The line $y = \pm x$ has been plotted as well. This shows whether the main effect is bigger than the standard deviation and the main effect is likely to be non-zero.

Due to the statistical nature of the Morris method, exact replication of the results of Hall et al. is not expected. Nevertheless, very similar

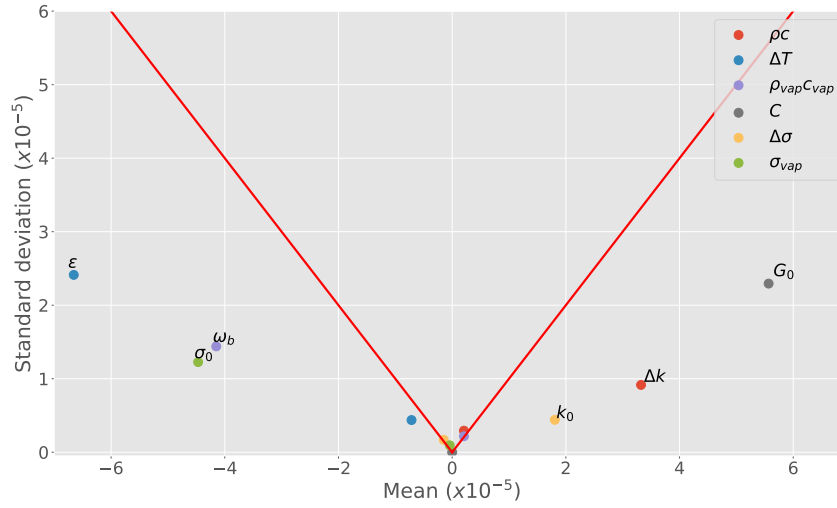Figure 34: Sensitivity analysis of model parameters as in Hall et al. [45]. Parameters clustered near zero are represented in the upper right legend. The solid line $y = \pm x$ is plotted. Points below this line have a mean larger than its standard deviation and thus the expectation value of the mean is non-zero.

results are achieved. The order of importance of the parameters is preserved, i.e., their deviation from the origin.

ATYPICAL CARTILAGINOUS TUMORS

Atypical Cartilaginous Tumors (ACT), or chondrosarcoma grade I according to older nomenclature, are often located at the proximal humerus, or other long bones that grow rapidly during adolescence [51]. At the Universitair Medisch Centrum Groningen (UMCG) these type of tumors is treated with RF ablation when non-surgical candidates are concerned. RF ablation has been shown to be an effective treatment option for ACT [52]. However, for better treatment planning, predictability over the ablation zone is still desired, and therefore a simulation model of ACT is made.

ACT's are characterized by cartilage-like histology in addition to being vascularized [53]. While ACT's and OO are both bone tumors, ACT's often lack the periosteal bone formation that is associated with OO [54].

Four patient-specific cases of RF treatment of ACT contained in femur were investigated. Pre- and post-treatment images were available from which the models were constructed, and the post-treatment ablation zone was determined. Information of the needle placement was also available as the needle was placed under CT-image guidance before treatment. Cross-sections concerning the angle of entry of the needle of the different patient cases are shown in figure 35. The different cases are referred to as case 2, 7, 9 and 15 respectively. All tumors were treated using a 17-gauge electrode with a target of 90 °C, as i . Case-specific details are shown in table 20.

Case 2, 7 and 9 show a typical ACT, being round or oval and having a diameter of between $1.5 - 3$ cm. Case 15 shows an atypical case of a much smaller rectangular-like tumor. Furthermore, due to the surrounding critical tissue, the angle of entry was limited. This resulted in the electrode being placed next to, instead of located within, the tumor.

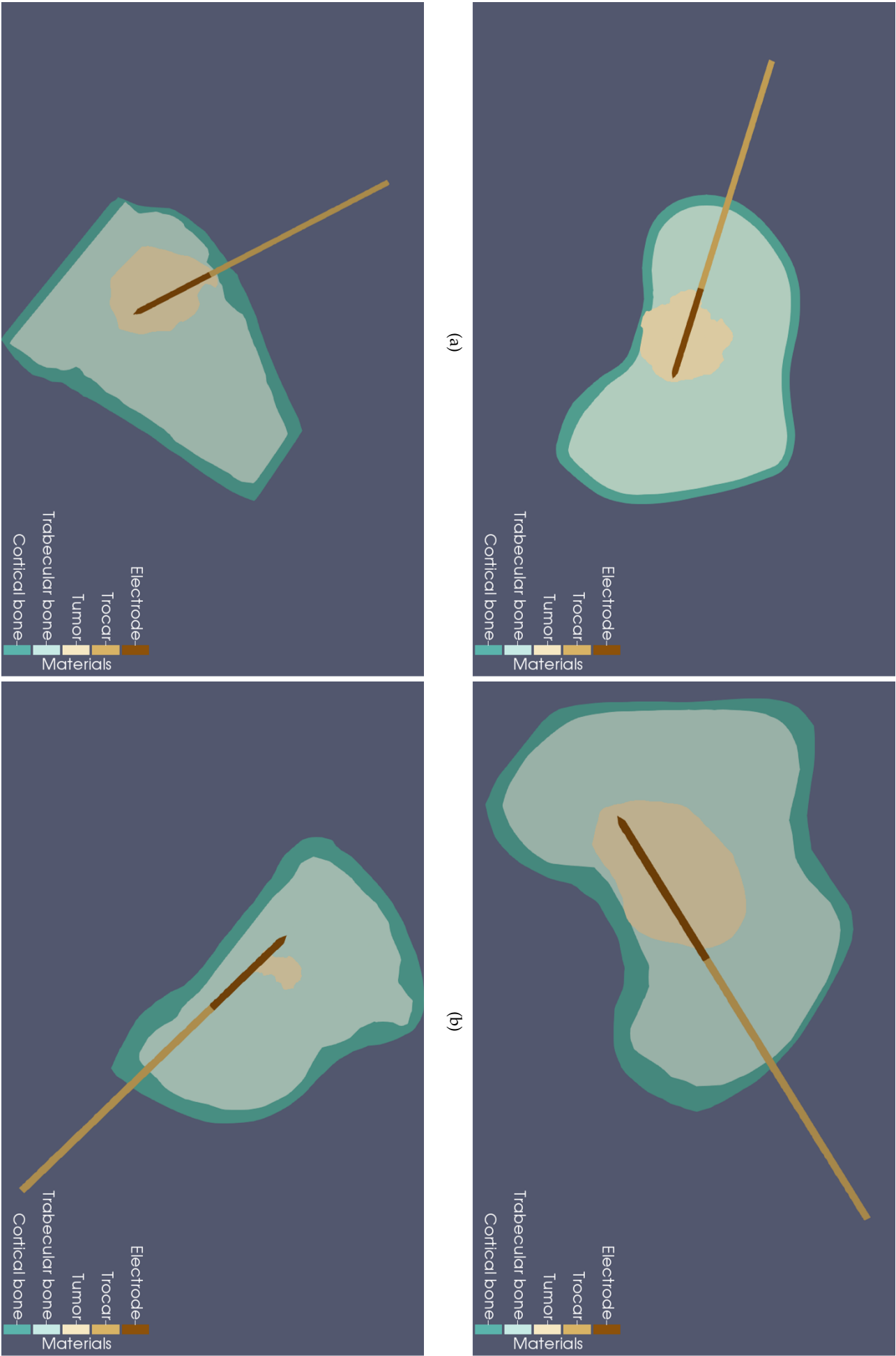| Case	Time at 90 °C (min)	Electrode length (mm)	Tumor shortest diameter (mm)	Tumor longest diameter (mm)
2	10	20	16	18
7	8	30	23	32
9	9	20	14	23
15	9	20	13	16

Table 20: Case-specific treatment parameters.

Figure 35: Cross sections of patient cases of ACT in femur: (a) case 2, (b) case 7, (c) case 9 and (d) case 15. Note that the cortical layer is surrounded by muscle, which is not pictured here.

5.1 CELL DEATH MODELS

We are interested in the extent of the ablation zone. Therefore, we want to simulate the cell viability throughout the procedure. This can be done by one of the cell death models presented in section 3.5.3. However, the different models give rise to different equations as they are based on different assumptions. Furthermore, most models are based on experimental data of different cell lines. Some of these cell lines are more thermally robust than others. For example, compare the experimental data of the three-state model by O'Neill et al [39] (see figure 31) against the experimental data of SN12 cells in figure 18(a). The former cell remains undamaged for the order of minutes, even at 100°C, while the latter shows total cell death over the same period at a lower temperature of 70°C. The delay before damage accumulation, such as in the three-state model, is known as the shoulder-region.

Since not much is known of the cell viability kinetics of ACT under hyperthermia, we investigate the extent of predicted cell damage with the use of different cell death models and cell lines.

To this end, an axisymmetric, two-dimensional model has been made based on the characteristics of the geometry as seen in the patient cases 35 and is shown in figure 36. The model consisted of a 17-gauge electrode of 20mm in length with a sharp-part of 1mm. The tumor was modeled as an ellipse with a major (z) diameter of 25mm and a minor (r) diameter of 20mm. The cortical layer had a fixed thickness of 2mm. The distance, d, between tumor and muscle for the model was set to be $d = 4mm$.

Finding material properties of specific tumors, or even tissues can be challenging, as is the case for ACT tumors. Since not much is known about the tumor characteristics, we use the same properties as in Irastorza et al. [7] which lists a range of possible values for bone tumors. The corresponding values are summarized in table 17. An absolute increment in thermal conductivity $\Delta k = 0.003K^{-1}$ was considered. Further, an increase of $1.5\%K^{-1}$ was considered for the electrical conductivity. The cell death model of O'Neill et al. [39] has been used to determine a cell death area. The fit parameters were set to the average parameters from table 2. A cell was considered dead when its viability reached below 80%.

The protocol entailed an ablation period of 600 seconds with a target temperature of 90 °C. As a result, the maximum temperature at any point in time was 93 °C and phase-change could be neglected.

The temperature control was modeled by a set voltage on the electrode by a PI-control as described in section 3.3.2. The PI-parameters were set to $K_p = 0.06$, $K_i = 1.15$, the same as in Irastorza et al. These parameters led to the target temperature being reached after around one minute, as is found in the patient-specific cases. Zero voltage was
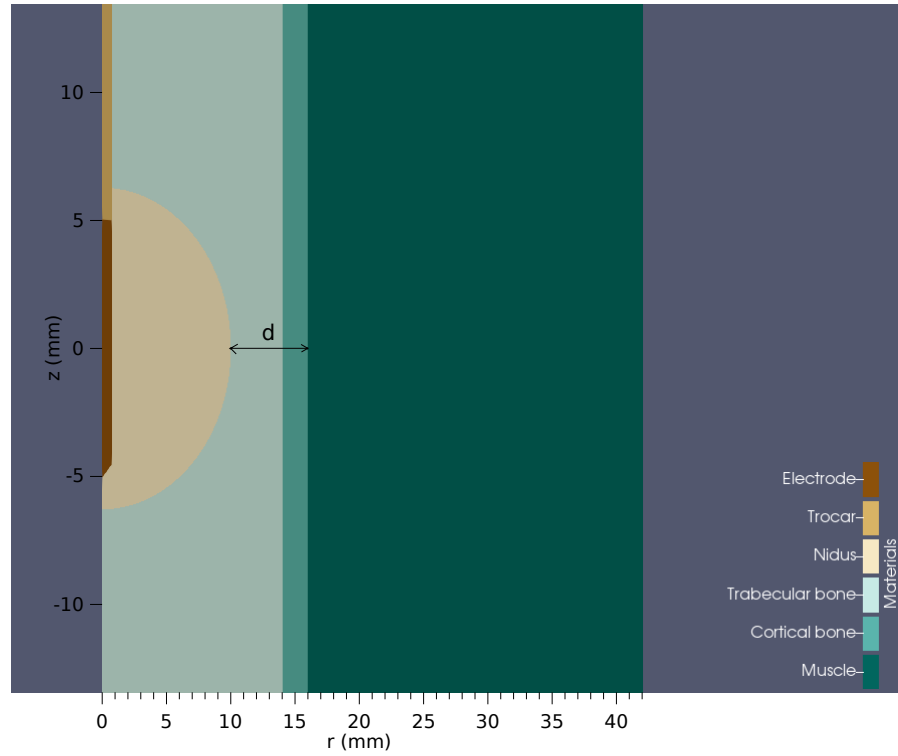
Figure 36: Two-dimensional, axisymmetric model of ACT. Here, d denotes the distance between the tumor and muscle region. The symmetry axis is the z-axis.

set on the boundaries away from the axis of symmetry to mimic the ground-pad. Initial temperature and temperature at the boundaries away from the axis of symmetry were set to 37 °C.

Convergence tests were performed to determine adequate domain size, spatial convergence, and temporal convergence. The domain size was increased, the mesh was refined, and the auto-time step tolerances lowered until the 50 °C- and cell death-area were within 0.5% of the previous iteration. After every test converged, they were repeated once more, as each convergence test requires constant values for the other parameters.

The final domain size was 42mm in width and 65mm in length. The domains consisted of approximately 9000 triangular elements. The lower and upper temporal tolerances were set to $\epsilon_l = 0.1$K, and $\epsilon_u = 0.5$K respectively.

For each simulation, the cell death profiles at the end of ablation are of interest. Further, as the heat trapped within the tissue does not suddenly disappear after ablation, the mesh is allowed to cool down. During this period there is no additional heat input, but the simulation steps are repeated until the maximum temperature in the mesh is under a certain threshold (see dashed line in the model schematic 12). The threshold was chosen to be 0.05 °C above normothermic conditions, i.e., 37.05 °C.

Figure 37: Ablation areas for different cell death models during ablation. (a) Area of cells above 50 °C. (b) Area of cells having less than 80% viability.
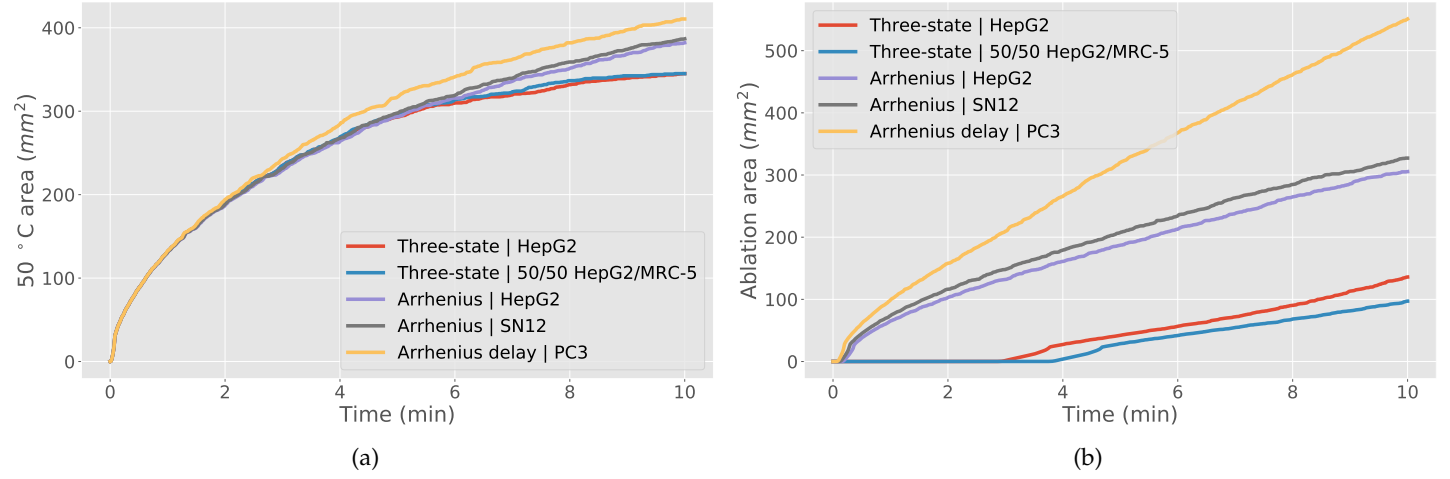
The parameters for the cell death models are shown in table 3. For the O'Neill et al. three-state model simulations, a cell was considered dead when the viability was less than 80%, as per suggestion of O'Neill et al [39]. Similarly, for the Arrhenius models a viability threshold of 80% corresponds to $\Omega = \ln(1/0.8) \approx 0.223$ (see eq. 3.5.8). This same threshold was used to determine the cut-off value below which perfusion was stopped. Results are shown in figure 37. Furthermore, a summary of simulation parameters is given in appendix A.7.

From figure 37 it can be seen that a higher area of 50 °C is reached with a higher area of cell death. This is as expected, as cell death means loss of perfusion and thus loss of cooling. Further, notice the discrepancy between the Arrhenius and three-state models of HepG2 cells. In the first, no shoulder region is observed, while in the latter no damage is observed due to the shoulder region until well into the ablation period ($\approx 3\text{min}$). The Arrhenius model of the SN12 cell line shows similar behavior as the HepG2 cells. However, the Arrhenius model of SN12 fits the original data very well [33] as it does not show a shoulder region (see figure 18(a)). The same conclusion was reached by Pearce [38] as the addition of a temperature-dependent delay did not improve the original fit. On the other hand, while both PC3 and SN12 cell experiments were performed under similar conditions, PC3 cells were found to have a significant shoulder region, and as such, benefit from a temperature-dependent time delay (see fig. 18(b) vs. fig. 19), indicating that different physical processes are at play for different cell lines under thermal stress [36]. Furthermore, as seen in figure 37(b), there is a noticeable difference in thermal robustness

between the two cell lines with SN12 cells being more robust than PC3.

However, most experiments are conducted on pure cell lines whereas tumors are known to be composite structures and sclerotic [55]. O'Neill et al. performed the experiments on co-cultures of HepG2 and MRC-5, a lung cell line, to model sclerotic tumor. The difference between the pure HepG2 and HepG2/MRC-5 mixture three-state model, also seen here, indicates a positive correlation between thermal robustness and tissue fibrosity (O'Neill et al.). This is supported by another experiment by Mayrhauser et al. [56] where hyperthermic treatment was performed on co-cultures of HepG2 and LX-1, a cell line associated with liver fibrosis, and thermal robustness increased with increasing percentages of LX-1.

Heat remains in the tissue after the ablation period. In extreme cases, temperatures as high as 40 °C remain 30 minutes after the procedure as seen in figure 38(a).However, extending the simulated time to include the cool-down period gives rise to a glaring limitation of the cell death models as is shown in figure 38(b). In this case, a-physical results are obtained in the form of exponential growth to total cell death for the three-state models and the PC3 Arrhenius model with a temperature-dependent time delay. In fact, what is seen is an artifact of the fit-parameters of both models. None of the models include a temperature-dependent threshold for damage accumulation, meaning that, even under normothermic conditions, i.e., 37°C, cells start to accumulate damage and the viability drops. The damage accumulation starts slowly for this temperature and is negligible for the periods over which the respective model was fitted. However, due to the exponential dependency (see eq. 3.5.13 and eq. 3.5.7), prolonging the simulated time will show total cell death at one point in time.

These are 24 and 61 minutes for the HepG2 and 50/50 HepG2/MRC-5 three-state cell death models respectively, 29 minutes for the PC3 cell line, 1277 minutes for SN12, and 517 minutes for the Arrhenius HepG2 model. It can be seen in figure 38(b), that the HepG2 three-state model and the PC3 Arrhenius model have surpassed their respective values, and as a consequence, show total cell death, whereas an exponential increase in ablation area can be seen for the 50/50 HepG2/MRC-5 three-state model, as it almost reaches its respective value.

However, the Arrhenius SN12 and Arrhenius HepG2 models do not show total cell death over the extended cool-down period. Further, they demonstrate that the ablation area grows quite substantially after ablation, 22.5% and 13.3% for HepG2 and SN12 cells respectively. The experimental data of SN12 cells of He and Bischof further support this significance, where damage accumulation during the non-isothermal portions of the thermal history (heat-up and cool-down) was found to be significant ($> 10\%$) when peak temperatures were
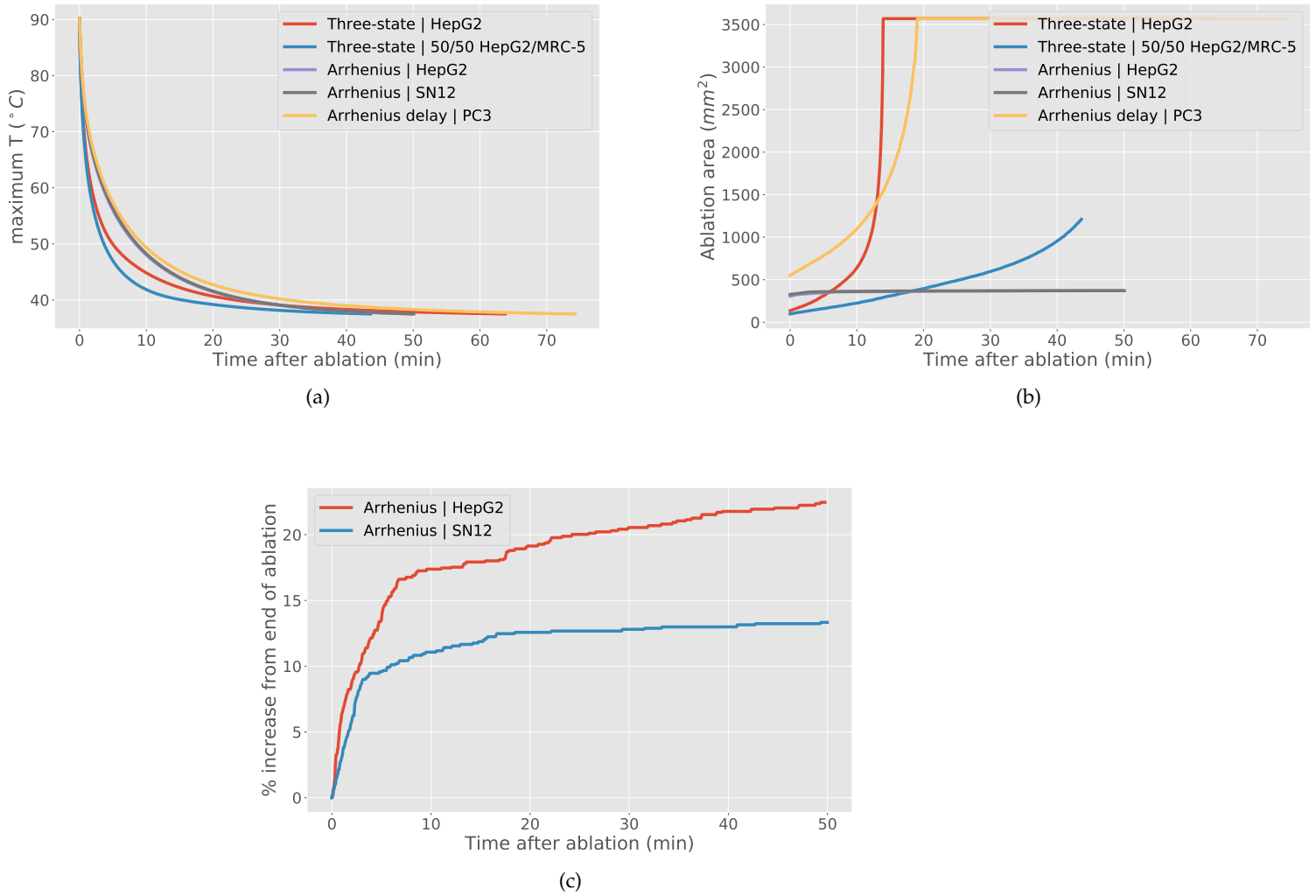
Figure 38: Minutes after ablation. (a) Maximum temperature in °C. (b) Area of cells having less than 80% viability. (c) Percentage increase in ablation area after ablation.

above 60 °C [33]. Another simulation study by Irastorza et al. draws the same conclusion, stating that the coagulation zone in computer modeling of RF ablation is underestimated by ignoring the cooling phase just after RF power is switched off [57].

5.2   PARAMETER SENSITIVITY OF THE ACT MODEL

Lack of accurate parameter values is one of the shortcomings of RF ablation simulation. Material parameters are usually derived from ex-vivo experiments or non-human tissue. Furthermore, parameters are likely to vary throughout the population and as such taking a single value is not accurate [45]. Here we investigate the sensitivity of the ACT model to its parameters through the Morris method as described in section 4.3.4.

The model used was the same as in the previous section (seen in figure 36). The protocol entailed an ablation period of 600s with a constant-temperature control set to 90 °C. From the previous section we can conclude that the cool-down period has a significant effect on the ablation zone and cannot be ignored. Therefore the sensitivity screening has been performed twice, once with the three-state model, ignoring cool-down, and with an Arrhenius model of SN12 cells, including cool-down. This way the parameter sensitivity during ablation can be investigated for two opposite cases. The three-state model showcases a cell line showing a shoulder region whereas the SN12 cell line does not. The latter is then also used to screen the sensitivity of parameters during the cool-down phase as it does not show a-physical behavior over the extended simulated time.

5.2.1   *Parameter uncertainty*

A wide range of tissue parameters is used in literature. The IT'IS foundation aims to provide an up-to-date database for tissue material parameters and statistical information about the spread and standard deviation per tissue [58]. Parameter values for density, heat capacity, thermal conductivity, and perfusion rates are found in this database. A range of electrical conductivities of tissues is retrieved from a database of dielectric properties of human tissue at RF and microwave frequencies [59].

The lower and upper values for the rate of change in electrical conductivity have been set to $\Delta\sigma \in [1\%, 2\%]$ to capture the range of values cited in the literature. Likewise, the values for the rate of change in thermal conductivity were taken to be $\Delta k \in [0, 0.0033]$ [7][57]. A value of zero for the Δk has been included as other studies remarked that RF ablation is non-sensitive to this parameter and can be ignored [31][45]. Maximum temperatures in the mesh did not exceed 95 °C, and thus, phase-change phenomena were ignored.

Tissue / Parameter	Lower	Upper
Density x heat capacity, $\rho C (\times 10^3 Jm^{-3}K^{-1})$		
Tumor	3847	4030
Trabecular bone	2225	3407
Cortical bone	1487	3465
Muscle	2732	4475
Thermal conductivity, k (W m^{-1}K^{-1})		
Tumor	0.47	0.518
Trabecular bone	0.29	0.36
Cortical bone	0.3	0.36
Muscle	0.4225	0.56
Electrical conductivity, $\sigma (Sm^{-1})$		
Tumor	0.08[a]	0.5[a]
Trabecular bone	0.030[b]	0.088[b]
Cortical bone	0.3[b]	0.36[b]
Muscle	0.4225[b]	0.56[b]
Perfusion rate, $\omega (\times 10^{-4}s^{-1})$		
Tumor	26[a]	70[a]
Trabecular bone	1.96	9.82
Cortical bone	0	3.18
Muscle	3.45	17.08
General parameters		
Electrical conductivity increase, $\Delta\sigma (\%K^{-1})$	0.01	0.02
Thermal conductivity increase, $\Delta k (Wm^{-1}K^{-2})$	0	0.0033
Cell viability threshold, $G_0 (\%)$	0.7	0.9
Cell culture make-up (three-state only), ϵ	0	1

Table 21: Lower and upper values of tissue parameters. All values extracted from [58] except, (a) [7] and (b) [59]

Values for the cell death threshold parameter have been set to $G_0 \in [70\%, 90\%]$, as it should cover the range over which thermal damage $(10\%, 30\%)$ should be reliably detectable amid biological tissue [36]. This threshold has also been used to determine the blood-perfusion cutoff as it is assumed that it marks the lower bound of the unperfused region [45]. For the Arrhenius model, using equation 3.5.8, the same cell viability threshold leads to $G_0 \in [0.105, 0.357]$. The three-state model has an extra parameter, $\epsilon \in [0, 1]$. As in Hall et al.[45], this parameter is used to interpolate over the values found in table 2. This way the effect of different co-cultures of HepG2 and MRC-5 can be investigated. A value of $\epsilon = 0$ corresponds to a homogeneous culture of HepG2.

All parameters which are used to construct the parameter space are summarized in table 21. For the three-state model, eight different trajectories are simulated with $k = 20$ parameters resulting in 168 simulations. Similarly, for the Arrhenius model 160 simulations are performed. A summary of the simulation parameters is given in in appendix A.8.

5.2.2 *The three-state model*

Results of the three-state model sensitivity analysis are shown in figure 40. The main outcome of the sensitivity analysis is the scatter plot shown in figure 40(a), where the mean elementary effect of the ablation area is plotted against its standard deviation. The line $y = \pm x$ has been plotted as a visual aid. Values below this line have a mean effect which is bigger than its standard deviation, and thus the main effect is likely to be non-zero. It is clear from this graph that the cell culture-makeup, ϵ, the cell death threshold, G_0, and the electrical conductivity parameters σ_{tum} and σ_{tra} dominate the uncertainty in the ablation area.

An increase in G_0 leads to a more significant ablation area. This is logical; the cell dead condition is sooner met with an increase in viability threshold, e.g., cells are considered dead at 90% viability instead of 85%.

Further, an increase in ϵ leads to a decrease in the ablation area. This can be explained by the increase in the percentage of MRC-5 in the co-culture make-up. As seen in figure 37(b) and concluded by O'Neill et al., an increase in MRC-5 leads a more thermally robust cell line due to the presence of fibrosis [39].

Interestingly, the electrical conductivity parameters, σ_{tum} and σ_{tra}, show an opposite behavior of the uncertainty in ablation area. An increase in the electrical conductivity of the tumor, σ_{tum} shows an increase in ablation area whereas an increase in the electrical conductivity of the immediately surrounding tissue, σ_{tra}, shows an expected decrease. The first is expected as the Joule heating term is roughly
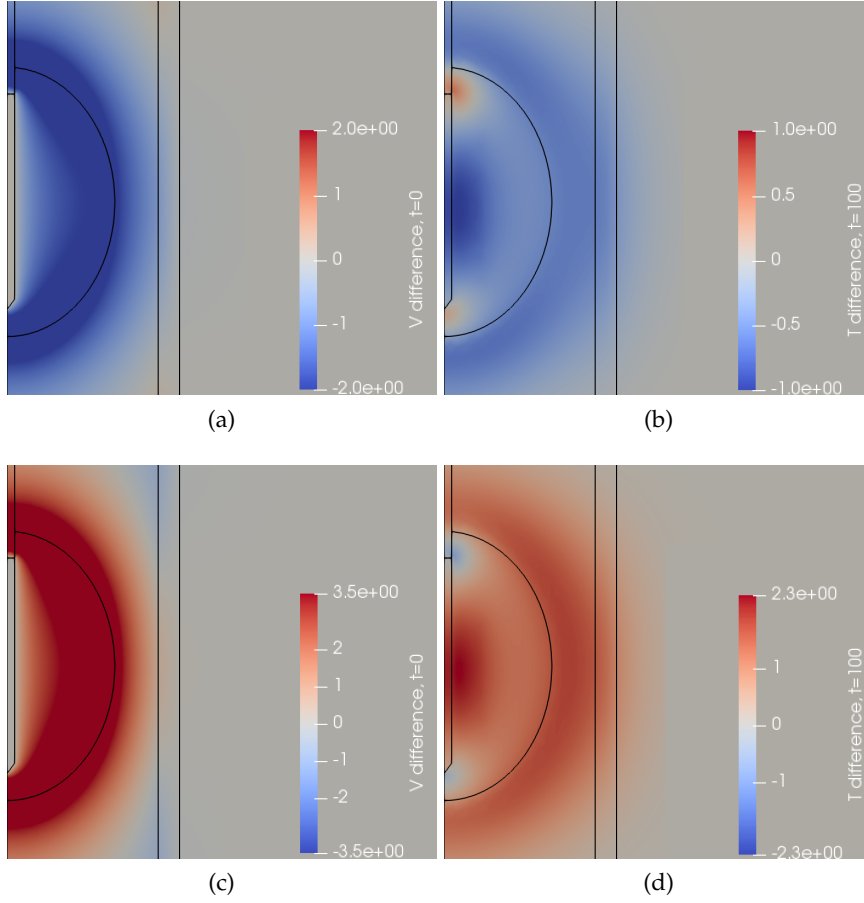
Figure 39: Difference in initial electric potential, ΔV, and temperature profiles, ΔT, at t=100s due to a $\Delta\sigma_{tra} \pm 0.1$. (a) ΔV due to an increase in σ_{tra}. (b) ΔT due to an increase in σ_{tra}. (c) ΔV due to a decrease in σ_{tra}. (d) ΔT due to a decrease in σ_{tra}

proportional to σV^2. An increase in σ would, therefore, lead to more heat being deposited into the tissue and a higher amount of damage. The latter effect is not as easily explained.

This effect has been further investigated by considering three simulations with all average parameters except σ_{tra}, which was set to $0.1, 0.2$ and 0.3 respectively. Then the difference in electrical potential and temperature was calculated by subtracting results of the mean simulation with $\sigma_{tra} = 0.2$ from the extremes. Results are shown in figure 39.

An increase in σ_{tra} leads to a decrease in the electrical potential at the tumor-trabecular interface (fig. 39(a)). As a consequence, the gradient of the electric potential over the electrode-tumor interface is higher. This, in turn, leads to higher resistive heating around the electrode and the temperature at the tip of the electrode rises faster. As a consequence of the PI-control scheme, the applied voltage throughout the ablation period is lower than before. The effect on the temperature

is then seen in figure 39(b) where the temperature remains lower at the tumor-trabecular interface.

The opposite effect is seen when σ_{tra} is decreased. Higher resistive heating at the tumor-trabecular interface is seen due to the increase in electrical potential at the interface. This, in turn, leads to an increase in the temperature at the tumor-trabecular interface and center of the electrode (fig. 39(d)).

The effect is a by-product of the PI-controller, which regulates the temperature through the temperature measured at the tip. This effect was therefore not seen in a repeat of the simulation where the PI-controller was replaced by a constant-voltage electrode. In this case, an increase of either σ_{tum} or σ_{tra} led to an increase in temperature and ablation zone.

The mean effect and standard deviation of the four most important parameters during ablation are plotted in figure 40(b) and 40(c) respectively. Due to the shoulder region, damage does not accumulate until after roughly three minutes. Furthermore, it can be seen that the cell death parameters, G_0 and ϵ, are the dominant effect until the last 100 seconds where the electrical parameters become important. This last period corresponds to the cell death extending beyond the tumor and accumulating within the trabecular bone.

In 40(d) the mean and standard deviation of the ablation zone area of all simulations is shown. Similarly, the mean and standard deviation of the area of cells above 50 °C has been plotted in 40(e) as The 50 °C isotherm is often used as a cell death indicator [24]. Here it can be seen that taking the 50 °C isoline as a cell death indicator over-predicts the ablation area compared to the three-state cell death model. The mean ablation area was $A_{abl} = 179 \pm 79 \text{mm}^2$ and the mean 50 °C area was $A_{50°C} = 481 \pm 101 \text{mm}^2$.

5.2.3 *The Arrhenius model*

The experiment has been repeated with the Arrhenius model of SN12 cells. As this model does not show a-physical results over an extended period, it can be used to investigate the sensitivity of parameters during ablation as well as the cool-down period for cells which do not show a shoulder-region. The cool-down period was considered completed when the maximum temperature was no more than 0.05 °C above the baseline value of 37 °C.

The sensitivity parameters used to construct the parameter space for the Morris method are the same as for the three-state model and summarized in table 21, except for ϵ, which has been excluded from this model. The results are shown in figure 41.
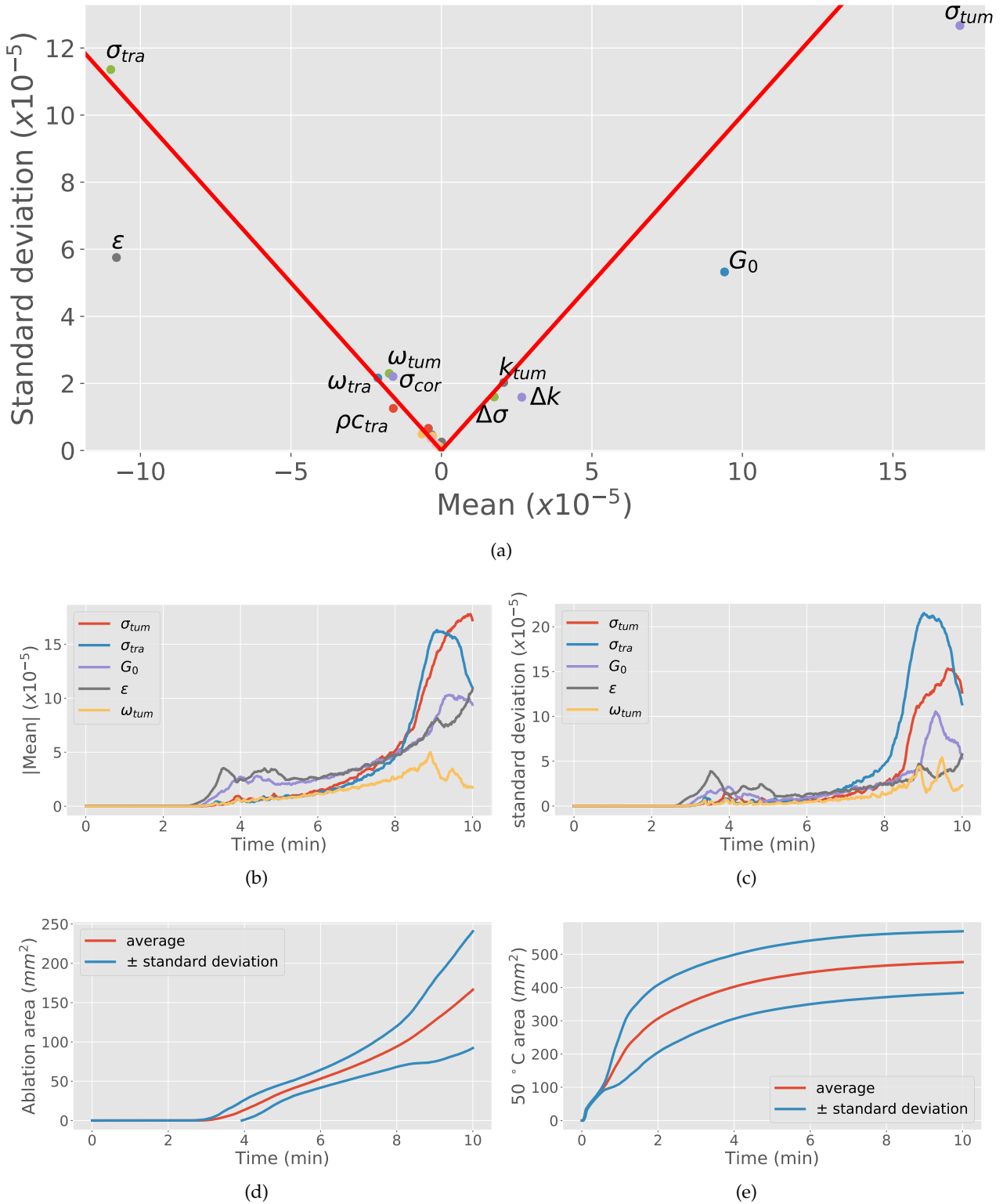
Figure 40: Results of three-state model sensitivity analysis of the ACT model. (a) The sensitivity scatter plot of the parameters presented in table 21. The line $y = \pm x$ (in red) is a visual guide, below the line, the mean effect is bigger than its standard deviation. Annotation of parameters clustered near zero has been left out for clarity. (b) the mean sensitivity of the four parameters with the largest effect with respect to time. (c) the standard deviation of the four sensitivity parameters with respect to time. (d) The mean ablation area of all 168 simulations with its respective standard deviation. (e) the mean area of cells above 50 °C and its standard deviation.

In figure 41(a) the sensitivity of the ablation zone to the parameters at the end of the simulation, that is, including ablation and cooldown-period, is plotted on a scatter plot, where again, the red line $y = \pm x$ is shown as a visual guide. Again, the electrical- and cell death parameters show the most substantial effect on the ablation zone. Also, as in the three-state model, the electrical conductivity of the tumor and trabecular bone show an opposite effect on the expected size of the ablation zone.

After these, the perfusion of muscle shows the most significant effect, a parameter that showed no effect during the three-state model. The damage accumulated within the three-state model never reached the muscle boundary. Here, whenever the damage is extended to the muscle region, the perfusion of this tissue had a significant effect. However, when the damage was contained within the bone, the effect of muscle perfusion was negligible, explaining that its standard deviation is higher than its mean.

The sensitivity of ablation zone growth during cool-down has also been investigated and is shown in figure 41(b). The growth during cool-down was defined by the final size of the ablation volume minus the volume at $t = 600s$. In this plot we can see that while G_0 and σ_{tum} remain important parameters, ω_{mus} becomes more dominant than σ_{tra}. Also, ρc_{tra} which has not shown any effect during ablation of either Arrhenius or three-state models affects the cool-down portion. This parameter dictates the ability of trabecular bone to absorb heat, and thus an increase leads to an increase in the ablation zone.

The mean sensitivity and standard deviation dependence during the simulation of the four most important parameters is shown in figure 41(c) and 41(d) respectively. The electrical parameters show a peak in the first minutes of the procedure; this coincides with the period where the ablation zone is within the respective tissue. This same effect was seen in the three-state model, only later as the damage accumulates later due to the shoulder region. The standard deviation of these parameters also shows a peak during this period. A change in electrical conductivity affects when its respective tissue is entirely damaged. A decrease in the standard deviation is then seen due to the tissue being damaged over the whole of the procedure. It is also clear from these figures that the effect due to the perfusion of muscle is only significant during the cool-down period.

In figure 41(e) the mean and standard deviation of the ablation area of all simulations is shown. The vertical dashed-line signifies the end of ablation. Similarly in figure 41(f) the mean and standard deviation of the percentile increase from the ablation area to the end of cool-down is shown.
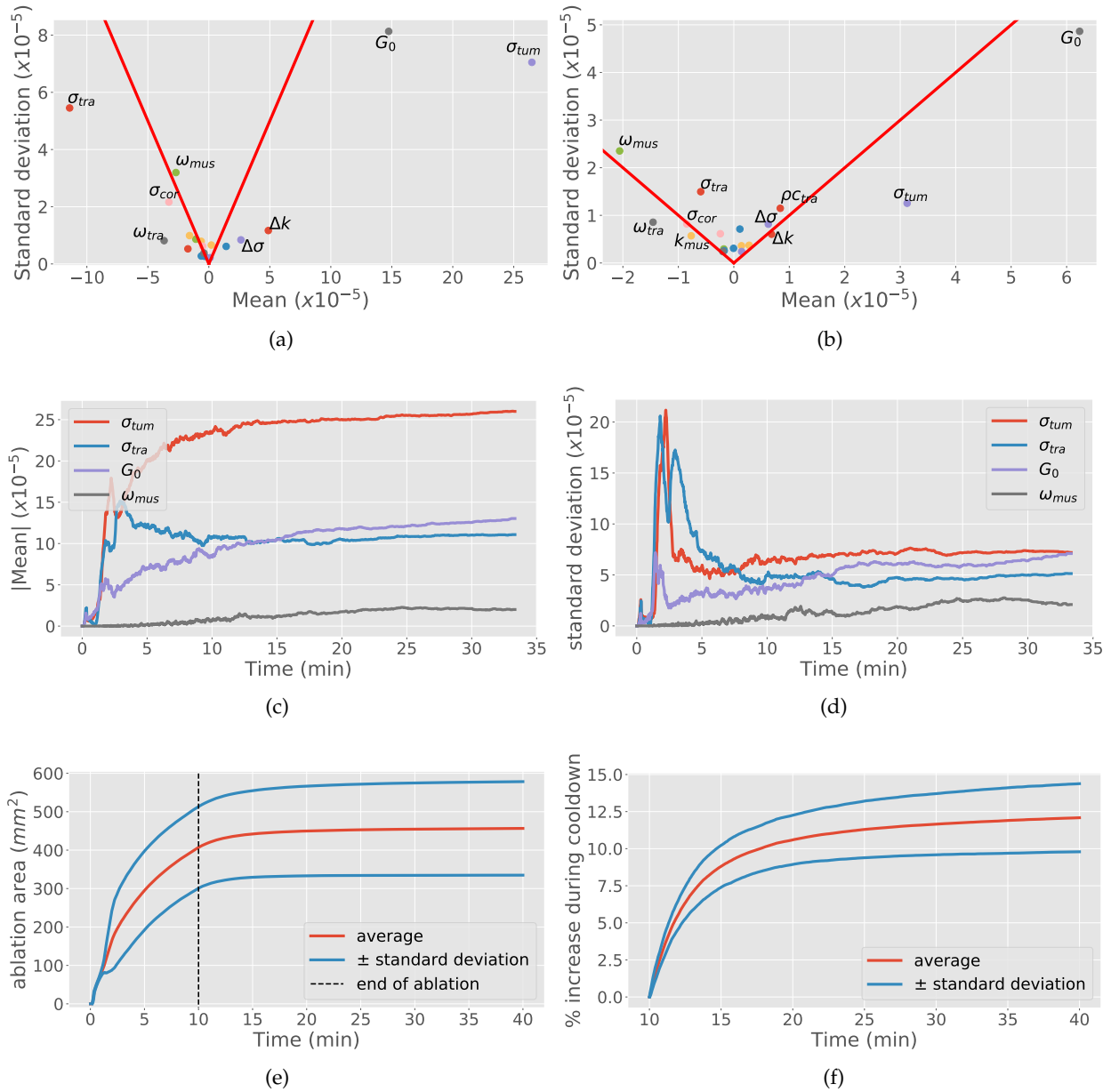
Figure 41: Results of SN12 cell Arrhenius model sensitivity analysis of the ACT model. (a) The sensitivity scatter plot of the final ablation zone due to the parameters presented in table 21. The line $y = \pm x$ (in red) is a visual guide, below the line, the mean effect is bigger than its standard deviation. Annotation of parameters clustered near zero has been left out for clarity. (b) the sensitivity scatter plot of increase in ablation size during cool down, i.e., the parameter of interest was the final ablation zone minus the ablation zone at $t = 600s$. (c) the mean sensitivity of the four parameters with the largest effect with respect to time. (d) the standard deviation of the four sensitivity parameters with respect to time. (e) The mean ablation area of all 168 simulations with its respective standard deviation. (f) the mean percentage increase in ablation area during cool down and its standard deviation.

The total ablation area was $A_{abl} = 457 \pm 122 \text{mm}^2$, a mean area which is 2.5 times the predicted area by the three-state model. The total increase in ablation area after cool-down was $\Delta A_{abl} = 12 \pm 2\%$, again signifying the importance of the inclusion of a cool-down period.

For both models, cell death, and electrical parameters of the tumor and trabecular bone, σ_{tum} and σ_{tra}, played the most significant part in determining the extent of the end ablation zone. As such, extra care should be taken for setting these parameters whereas constant values can be taken for other parameters.

The perfusion of muscle played an important part when the ablation zone extended within the muscle and cool-down was considered. The effect of muscle perfusion could have an even more significant impact as *in-vivo* blood perfusion initially increases with temperature. This initial increase is an attempt of the body to reduce the temperature to normothermic values. Research shows that this effect is most significant for muscle tissue, which can increase 9-fold until 45 °C, after which a constant value is retained [60]. Such a temperature-dependent perfusion term has not been included in the model and hence should be a reference for further investigation.

5.3   PATIENT-SPECIFIC SIMULATIONS

Simulations have been performed based on the patient-specific cases presented at the beginning of this chapter. Up to this point, most of the simulations were run on two-dimensional meshes made out of simple geometries. These kind of meshes are relatively easily made with sufficient quality to use within the finite element method. However, this is not the case for the three-dimensional meshing of complex-geometries such as patient-specific models, and as such, the method of creating these meshes is explained here.

5.3.1   *Patient-specific mesh*

Patient data is annotated into three different categories; tumor, trabecular bone, and cortical bone. A closed-surface representation of these tissues is then exported. These surface-representations are then used to construct volume meshes.

The difficulty lies in the making of a coherent and accurate three-dimensional mesh, containing the surgical needle. To this end, the creation of the mesh works from inwards to outwards, starting at the needle and after that adding the outer layers; tumor, trabecular bone, cortical bone and an outermost layer of muscle. In this way, the mesh can be made coherent, having no overlapping or missing layers.

The needle is based on CT-images made before the procedure. By extracting a tip-point, a point of entry and knowing the radius, the
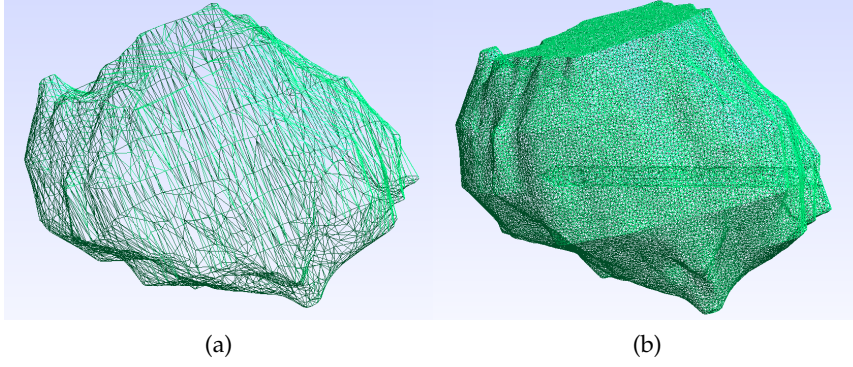
<div style="text-align:center">(a)   (b)</div>

Figure 42: Results of the refinement process of the tumor segmentation of case 9, prior to the creation of the patient-specific mesh. (a) non-refined. (b) refined surface-representation with a target tolerance of 5mm. Further, a silhouette of needle can be seen, this is a result of the applied boolean operations, ensuring there is no overlapping volumes.

needle can be constructed along the line spanned between the two points. This is done in *GMSH*, a three-dimensional finite element grid generator [61], where the needle is constructed from simple shapes: a cone for the tip of the needle and cylinders for the needle-shaft.

To create a coherent mesh, boolean mesh operations must be applied. These operations allow for creating the union or difference between two meshes. The latter is used here, as the inserted needle must be subtracted from the tissue. Before this can happen, the surface representations of the tissues are optimized. This optimization is performed in *Pymesh*, a python library which provides access to popular open-source mesh libraries such as *CGAL*, *Cork* and *Tetgen* [62]. With this library, common mesh-artifacts such as isolated vertices and self-intersections can be removed. Furthermore, a refinement loop is applied to make the mesh more uniform. All edges longer than a specified tolerance are split, while all edges shorter than a specified tolerance are elongated. This is repeated until all edges are bound, or a maximum number of loops is reached. The results of such a refinement-loop is shown in figure 42.

After refinement, the meshes are subtracted from one another to ensure no overlapping volumes are present (see fig. 42(b)). Lastly, the meshes are placed within a box which will act as muscle and can be increased to determine the domain size convergence.

Then all surface meshes are imported back within GMSH, where a three-dimensional mesh can be created now that all surfaces are coherent. The number of elements for the patient-specific meshes was in the range of $1-2x10^6$. To compute the simulations within a reasonable time, the model has been adjusted to allow for parallel solving. Furthermore, the model has been implemented on the Peregrine high performance computing cluster.

parameter	minimum	average	maximum
$G_0(\%)$	0.7	0.8	0.9
$\sigma_{tum}(Sm^{-1})$	0.08	0.29	0.5
$\sigma_{tra}(Sm^{-1})$	0.088	0.059	0.03

Table 22: Parameters which were changed to represent an expected minimum, average and maximum case respectively. Note that σ_{tra} is higher for the minimum case , and after that decreases. This is due to the aforementioned opposite effect with respect to σ_{tum}.

5.3.2 *Simulation parameters*

Simulations have been run on the patient-specific meshes to determine a predicted ablation zone.

Initial temperatures and temperatures at the outer-boundaries were assumed to be 37 °C. Temperature was controlled by a PI-controller with a target temperature of 90 °C. To mimic the original protocol, the simulations included a warming-up time. During this period, the tip-temperature was increased until it reached its target, then the ablation period was extended to their respective duration as summarized in table 20.

As concluded in the previous sections about parameter sensitivity, the ablation zone is most sensitive to only a few parameters. However, the range of these parameters represents an uncertainty; either due to a lack of experimental data or variations found within the data. Therefore, three simulations were performed for each case, representing an expected minimum, average, and maximum ablation zone.

Due to the increased computational costs of the patient-specific simulations, only the Arrhenius model of SN12 cells has been considered. This choice was made as the model does not show a-physical results throughout ablation and cool-down. Where the latter, as concluded previously, has a significant contribution to the ablation zone prediction. In this manner, a final expected ablation zone can be predicted for cells showing no shoulder region.

The most sensitive parameters for the Arrhenius model were the cell death viability threshold value ,G_0, and electrical conductivity parameters, σ_{tum} and σ_{tra}, for tumor and trabecular tissue respectively. These parameters were changed to represent the three simulation cases mentioned previously and are represented in table 22. For all other parameters, average values from table 21 were considered. A summary of the simulation parameters is given in appendix A.9.
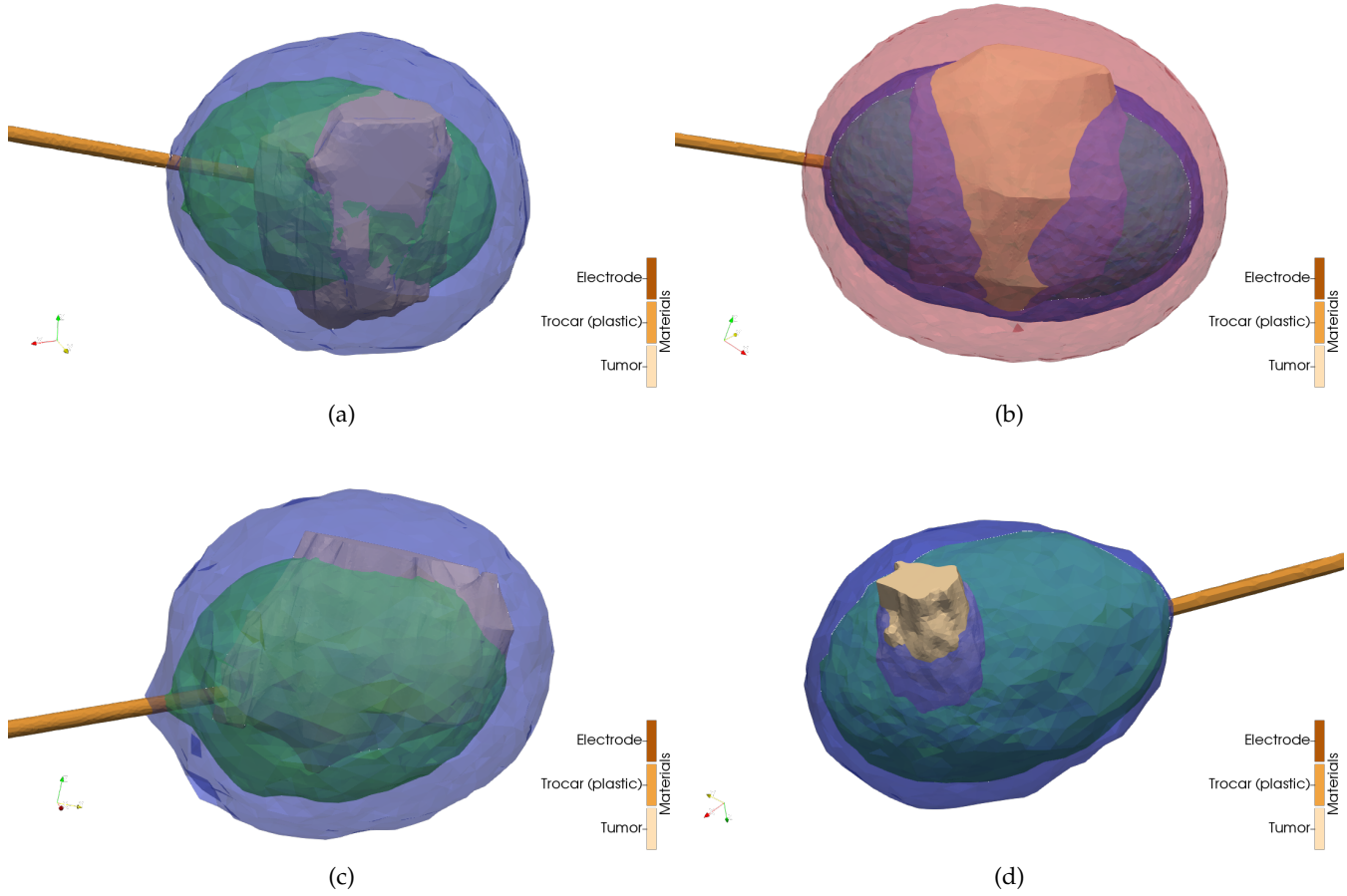
Figure 43: Three-dimensional representations of the predicted cell death. The green, blue and red contours represent a minimum, average and maximum case respectively. (a) Case 2, (b) case 7, (c), case 9 and (d) case 15. Note that a maximum size for case 2, 9 and 15 is not available as the simulations exceeded their requested time limit.

5.3.3   *Results*

Complications arose during some of the simulations. When a maximum case was considered for cases 2, 9, and 15, the temperature within the model exceeded 100 °C. Although the PI-controller regulates the temperature, which had a target below 100°C for all cases, the maximum temperature does not necessarily occur at the tip of the electrode. Despite the model being able to accurately handle phase-change phenomena, the adaptive time step reduced drastically. As a consequence, these simulations did not finish within the requested simulation time, i.e., these simulations took longer than 72 hours on the high-performance cluster, and have been excluded from the results.

Coverage of the expected ablation radius is shown in figure 43. From this figure, it is seen that using the simulation parameters for a

minimum expected ablation zone (in green) leads to a non-successful procedure in all of the patient cases. However, depending on the patient case, the average parameters can lead to a successfully predicted procedure. In particular, patient cases 2 and 9, figure 43(a) and 43(c) respectively, show that the tumor is fully located within the predicted cell death.

Case 7 (figure 43(b)) shows a successful procedure when a maximum case is considered. These results further demonstrate the need for accurate values of these parameters. In all cases, the predicted success of the procedure depends on these parameters.

From each simulation, a longest diameter, d_l, and shortest diameter, d_s, is determined. These diameters are compared to post-treatment MRI-images from which a visual ablation zone could be inferred. Slices from which these diameters are determined are shown in figure 44. The results are summarized in table 23.

While an ellipsoid can rather well approximate all simulated ablation zones, post-treatment MRI-data can show a clear-cut cutoff. This effect shows when the ablation zone extends to within the muscle-layer. This could be due to the increase of perfusion with increasing temperature, which is not included in this model, as explained in the previous section. Different cell death mechanisms for different tissue-types could also explain this effect. As previously seen in figures 18(a), 19, and 31, different cell types show different cell death rates under hyperthermic stress. If a certain type of tissue shows a significant higher thermal robustness, it will show as a clear-cut region as seen in the MRI-data. Lastly, since the MRI-data is not taken immediate after treatment, it is possible that the muscle has healed.

	Measured		Simulated			
Case	d_l (mm)	d_s (mm)	Simulation case	d_l (mm)	d_s (mm)	volume (cm^3)
2	43	26	min	32	22	8
			avg	37	33	20
7	65	32	min	44	23	15
			avg	45	29	22
			max	51	40	44
9	42	40	min	32	23	10
			avg	39	33	21
15	30	25	min	31	20	8
			avg	33	26	11

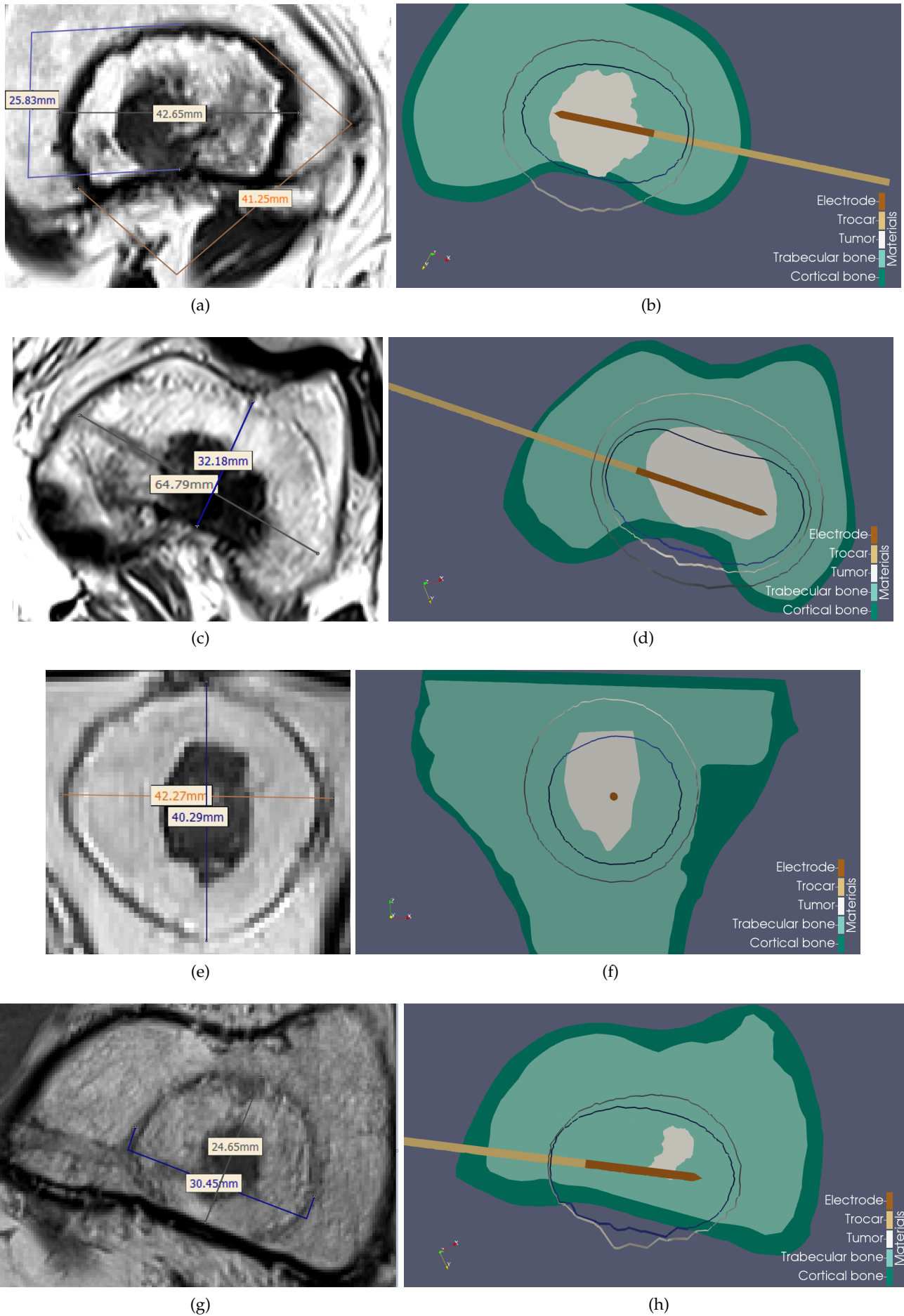Table 23: ablation zone dimensions from MRI-data (measured) and simulated data.

Figure 44: Measured ablation diameter and predicted ablation diameter on the left and right respectively. From smallest to largest the ablation radii are a minimum, average, and when present, maximum case. (a) and (b), (c) and (d), (e) and (f), (g) and (h) represent case 2, 7, 9 and 15 respectively. Each simulated case is surrounded by muscle (gray).

Inspecting case 2 (figure 44(a), 44(b)), we see that the model fails to accurately represent such a cut-off region, extending the ablation zone to well within the muscle layer. Regardless, the simulation considering a minimum expected case underestimates the actual ablation zone, where the longest and shortest diameter differ by 11 and 4 mm respectively. On the other hand, the average considered case differs by 6 and 8 mm for d_l and d_s, overestimating the shortest diameter. The latter, however, shows a significant increase in ablation damage in muscle. Artificially inducing a clear-cut region, by just ignoring the damage in the muscle-region, would reduce d_s to 26 mm, as found in MRI-data.

Case 7 (figure 44(c), 44(d)), also shows a clear-cut ablation zone, which, again, is not seen in the simulation data. Interestingly, this case represents an outlier, in the sense that even the maximum predicted ablation zone underestimates the actual case. From the MRI-data it is seen that both the minimum and maximum diameter extend to the muscle-region. Such results can be achieved when either more extreme parameters are considered than those summarized in table 22, or the inclusion of a cell line which is less thermal-robust.

For now, we can mimic the latter by adjusting the cell viability threshold, G_0, such that the extent of the ablation zone is similar to the one in MRI-data. As seen in figure 45(a), a viability threshold 0.97% is needed to create a similar ablation zone as found in the MRI-data. Although, in reality, the viability threshold needed to create such an ablation zone would be a bit lower due to the effect of the threshold on the perfusion cut-off. Nevertheless, it would require a feeble cell line, while we already consider a cell line without a shoulder-region.

Further, we can also look at the temperature isotherm that corresponds with the border of the actual ablation zone at the end of ablation. As it turns out, this would correspond to a cell death model which shows irreversible damage at a peak temperature of no more than 39 °C as seen in figure 45(b). It is therefore much more reasonable that the increase in ablation zone is due to the electrical parameters, and as such, that the range of values found for σ_{tum} and σ_{tra} (table 21), does not adequately represent the variation found within the population.

In case 9 (figure 44(e), 44(f)), the minimum considered simulation case underestimates the actual ablation zone and does not predict a successful procedure. However, it is clear from the MRI-data that the tumor is fully located within the ablation zone. The average predicted case shows more resemblance to the actual case, differing only by 3 and 7mm for the longest and shortest diameter respectively. Note that the MRI-data does not show a clear-cut region as the tumor is located centrally within the trabecular bone.
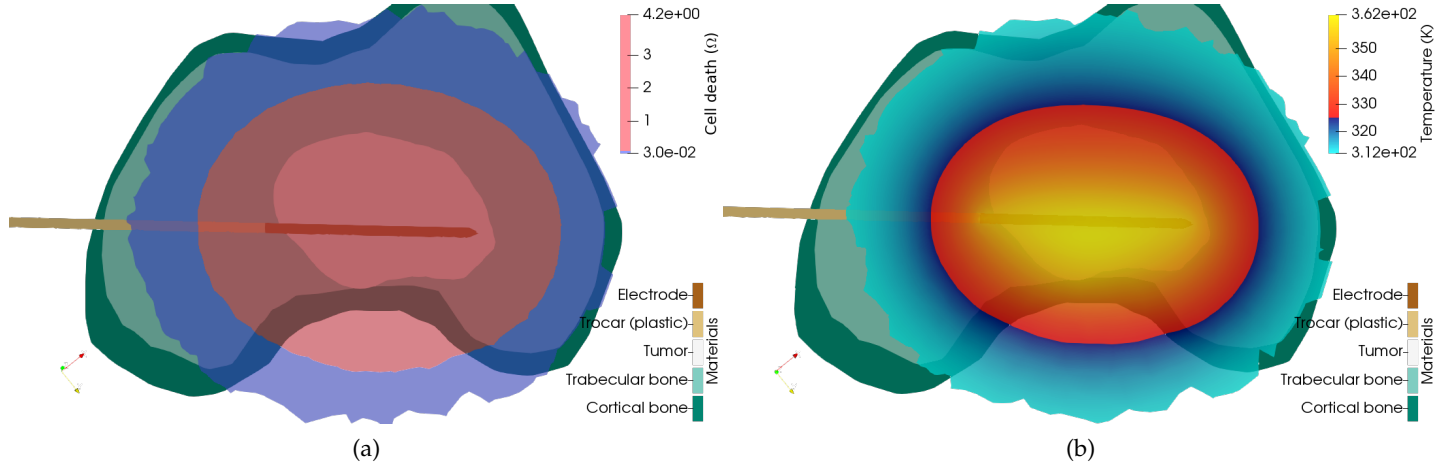
Figure 45: Isotherm data of the maximum simulation case of patient 7. (a) Arrhenius cell death at the end of simulation, the sharp border between the red and blue corresponds to the value of $\Omega = 0.105$, which corresponds to the 90% viability isotherm (eq. 3.5.8), which was used during the simulation. The border has been extended to $\Omega = 0.03$, or a 97% viability rate, to retrieve a similar ablation region as seen in the MRI-data (see fig. 44(c)). Similarly, (b) shows the temperature distribution at the end of ablation. The sharp border between red and blue denote the 50°C isotherm. To retrieve a similar ablation zone as seen in *in-vivo*, cells would need to accumulate irreversible cell damage at a peak temperature of 39°C.

Case 15 (figure 44(g), 44(h)), does show a clear-cut of the ablation zone at the cortical muscle interface, which, again, is not seen in the simulated data. Nonetheless, the average simulated case represents the actual situation quite well, differing only 3 and 1 mm in the longest and shortest diameter respectively. This case also showed the least difference between simulated cases. The average simulated case showed only an increase of 2 and 6 mm for the longest and shortest diameter respectively. At the same time, the case contained the smallest tumor, and as such, it should be expected that changing its parameters has the least overall effect of all the cases.

For each case, the difference between simulation cases is most significant in the shortest diameter, i.e., the direction perpendicular to the electrode, which always showed a more substantial increase than the diameter along the electrode. On average, the difference between the shortest diameter of a minimum and an average case was 8.25 mm, while only 3.75 mm for the longest diameter.

6

CONCLUSIONS

A model for simulating radio-frequency (RF) ablation has been made based on the finite element method. The model is capable of simulating axisymmetric- as well as three-dimensional models. Furthermore, non-linear material properties have been implemented as well as different power control schemes. These included a constant-voltage scheme, a target-temperature scheme dictated by a PI-controller and an impedance control scheme. Internally cooled electrodes, such as the *Cool-Tip*-electrode can also be modeled.

An apparent heat capacity form of the Pennes' bio-heat equation has been implemented to account for phase change phenomena when the temperature exceeds 100 °C. However, time step sizes must be reduced to represent phase changes adequately. To increase the efficiency of the model, two different time stepping schemes have been implemented. The first is the implicit Euler method, which was implemented due to the ease of programming, and acted as a benchmark. The second is an explicit three-level scheme from Lees [43], which has an adaptive time step method based on the change in temperature between two consecutive steps.

Different cell death models have been implemented. These include: the Arrhenius model, the Arrhenius model with a temperature-dependent time delay by Pearce [38], and the three-state model of O'Neill et al. [39]. Since perfusion is stopped when cells die due to coagulation, these models also included a feedback mechanism to determine the perfusion cutoff.

The implementation and validity of the different solvers have been extensively tested. The method of manufactured solutions was used to determine convergence rates. All tests retrieved their correct convergence rates. Second, two analytic problems were tested; the first being a two-dimensional, axisymmetric model containing a semi-infinite electrode, the second a one-dimensional Stefan problem. The solutions to both problems were found to be within 1% of the analytical solution. Third, simulations by other groups were replicated. Excellent agreement was reached for the simulations of Berjano [7] [28], differing less than 1% at all times. The replication of the simulation of Hall et al. involved a sensitivity analysis, which due to the statistical nature of the analysis was not expected to retrieve the same results. Nevertheless, very similar results were achieved [45], in particular, the order of parameter importance was conserved.

Then the model was used to investigate characteristics of RF ablation of ACT. First, the simulations were performed to compare differ-

ent cell death models. The three-state model showed significant lower predicted ablation zones than other models. Further, from these simulations, it became clear that ignoring the cool-down phase has a substantial impact on the expected ablation zone ($> 10\%$). This conclusion is shared by another simulation study of RF-ablation of the liver by Irastorza et al. [57]. Furthermore, an experiment of cell viability of SN12 cells by He and Bischof found that ignoring the non-isothermal periods of RF ablation (heat-up and cool-down) underestimates the final ablation zone [33]. However, it also became clear that most cell death models showed a-physical results over the extended period of cool-down, reaching a state of total cell death even under normothermic conditions. This is an artifact due to the limited time range over which the experimental data were fitted, considering ablation periods of at most 15 minutes.

The parameter sensitivity has been investigated for the three-state model as well as the Arrhenius model for SN12 cells, using the Morris method. The first represents a case of cells showing a shoulder-region while the latter does not. For both cases, the parameter governing the cell viability, $G_0 \in [70, 90\%]$ was of most importance. This is to be expected as it directly dictates when a cell is considered dead. The range was set as it would most likely correspond to a threshold which should be reliably detectable amid biological tissue [36].

Then the electrical parameters of the tumor, $_{tum} \in [0.08, 0.5](S/m)$ [7], and surrounding trabecular bone, $\sigma_{tra} \in [0.03, 0.08](S/m)$, showed the most significant contribution to the uncertainty in ablation zone . Interestingly, the parameters showed an opposite effect on the predicted ablation zone, a result also present in the study of Irastorza et al.[7]: increasing with an increase of σ_{tum} and decreasing with an increase σ_{tra}. It was concluded that this effect is a by-product of the used temperature control, where the target temperature was reached sooner due to a local decrease in electric potential around the electrode tip. The effect was, therefore, not seen when a constant-voltage control replaced the temperature control.

Further, the Arrhenius model showed the perfusion of muscle as an essential parameter. The standard deviation of this parameter was more significant than its mean. This meant that changing the parameter did not always result in a change in the predicted ablation zone, but when it did, the contribution was significant. Further investigation showed that the effect of the parameter was only significant when the ablation zone reached within the muscle. Nonetheless, the effect of this parameter can be underestimated as muscle perfusion increases with temperature [60].

The sensitivity analysis also showed the significant difference in predicted ablation zone between the three-state and SN12 model, predicting an area of $A_{abl} = 179 \pm 79 \text{mm}^2$ and $A_{abl} = 457 \pm 122 \text{mm}^2$ respectively. Where the latter showed an increase in ablation area dur-

ing cool-down of $12 \pm 2\%$, the first did not include a cool-down period, as it leads to the previously mentioned a-physical result of cell death at 37 °C. The increase during cool-down could be even more significant for such a model, due to the non-linear dependence on cell viability and the presence of the shoulder region, which delays the time at which cell damage occurs.

CT-data of four patient cases having an ACT were available from which patient-specific models could be created. The needle was placed under CT-guidance from which a final placement could be deduced. Furthermore, post-treatment MRI-images were available from which an actual final ablation zone could be determined. The final models contained between one and two million elements. To reduce the computation time, the model has been rewritten and implemented on the Peregrine high-performance cluster.

Based on the sensitivity analysis, a minimum, average, and maximum expected ablation zone case has been simulated for each of the patient cases. These were determined by changing the cell viability threshold, and the electrical conductivity parameters of the tumor and trabecular bone. Complications arose during three of the simulations. All three simulations involved a maximum considered-case where the temperature exceeded 100 °C. Although the model can handle phase-change phenomena, the time step reduced drastically, and the simulations did not finish within the requested time.

Nonetheless, the simulations show that patient-specific parameters are decisive in the outcome of the procedure. Considering a minimum simulation case, the procedure is ineffective in all patient cases, failing to ablate the whole of the tumor, whereas considering an average or maximum case shows a successful procedure.

One of the cases showed an ablation zone bigger than even the largest predicted ablation zone. Investigating how to achieve a similar ablation zone, a G_0 of 0.97% is required. Otherwise, using a different cell death model would need for a cell line which shows significant damage at a peak temperature of only 39 °C. A more reasonable explanation is therefore that the range of electrical conductivity parameters suggested does not cover the variation found within the population.

In three patient cases a clear-cut ablation region is seen, something which is not present in the simulations. In these cases, the ablation region does not extend to the muscle region. The temperature dependent perfusion rate, as mentioned earlier, could cause such a clear-cut between tissues, something which is not included in the model. The clear-cut could also be a consequence of different tissues being more robust than others under thermal stress [36][33][63]. Therefore, further research should focus on the cell viability response of both cancerous and healthy tissue, under hyperthermic stress. As of now, the same parameters are used for every type of tissue. Further steps

should be taken to improve the model. For one, the effect of a non-linear perfusion rate on the clear-cut region should be investigated.

The current implementation of the model lacks a cell death model which can accurately represent a shoulder region and not show cell death under normothermic conditions, over the extended simulated time when a cool-period is considered. A first step would be to replicate the three-state model of O'Neill et al., but include viability data over longer heating times and temperatures close to normothermia. This, in theory, should extend the time after which the model predicts cell death under normothermic conditions. This increased period is needed as it was shown that the ablation zone grows significantly during the cool-down phase.

Lastly, to reduce uncertainty in the predicted ablation zone, experiments should be conducted to get more information about the variation within electrical conductivity parameters of both the tumor and the immediately surrounding tissue, as concluded from the sensitivity analysis.

SIMULATION SPECIFIC PARAMETERS

In this appendix, additional tables are given with the specific simulation parameters for each simulation.

A.1 SEMI-INFINITE ELECTRODE

Parameter	value
$t_{ablation}$	until steady state
$T_{initial}$	5 °C
Power control	Constant
V_{el}	10V
Thermal conductivity (k)	Constant
Electrical conductivity (σ)	Constant
Density x specific heat (ρc)	Constant
Cell death model	None
Time stepping	
algorithm	Lees
$\Delta t_{initial}$	1×10^{-6} s
Δt_{max}	1×10^{12} s
τ_l	0.25 K
τ_u	0.5 K

Table 24: Summary of the simulation parameters used in the semi-infinite electrode model, in section 4.2.1.

Parameter	value
$t_{simulation}$	50 h
$T_{initial}$	20 °C
$T_{x=0}$	-10 °C
ΔT	$1, 0.5$ °C
Power control	Constant
V_{el}	0 V
Thermal conductivity (k)	Temperature-dependent
T_l	$0 - \Delta T$ °C
T_u	$0 + \Delta T$ °C
Electrical conductivity (σ)	Constant
Density x specific heat (ρc)	Temperature-dependent
T_l	$0 - \Delta T$ °C
T_u	$0 + \Delta T$ °C
C_{water}	100 %
L_{fusion}	333 (KJ/Kg)
ρ_{water}	1000 (Kg/m^3)
Cell death model	None
Time stepping	
algorithm	Lees
$\Delta t_{initial}$	$1x10^{-6}$ s
Δt_{max}	$1x10^{12}$ s
τ_l	0.25 K
τ_u	0.5 K

Table 25: Summary of the simulation parameters used in the one-dimensional solidification model, in section 4.2.2.

A.3 RF ABLATION IN OSTEOMA OSTEOIDE

Parameter	value
$t_{ablation}$	400 s
$T_{initial}$	35 °C
Power control	PI-control
T_{target}	95 °C
k_p	1.15
k_i	0.06
Thermal conductivity (k)	Temperature-dependent
T_0	37 °C
T_{max}	100 °C
Δk	$0.003(W/(m \cdot K^2))$
Electrical conductivity (σ)	Temperature-dependent
T_l	100 °C
T_u	105 °C
$\Delta\sigma$	$1.5\%K^{-1}$
σ_{vap}	$\sigma x10^{-4}$
Density x specific heat (ρc)	Temperature-dependent
T_l	99 °C
T_u	100 °C
C_{water}	99.2 %
$L_{vaporization}$	2260 (KJ/Kg)
ρ_{water}	1000 (Kg/m^3)
Time stepping	
algorithm	Lees
$\Delta t_{initial}$	$1x10^{-6}$ s
Δt_{max}	0.5 s
τ_l	0.1 K
τ_u	0.25 K

Table 26: Summary of the simulation parameters used in the Osteoma Osteoide model, in section 4.3.1.

A.4   RF ABLATION IN CORTICAL OSTEOMA OSTEOIDE

Parameter	value
$t_{ablation}$	400 s
$T_{initial}$	37 °C
Power control	PI-control
T_{target}	95 °C
k_p	1.15
k_i	0.06
Thermal conductivity (k)	Temperature-dependent
T_0	37 °C
T_{max}	100 °C
Δk	$0.003(W/(m \cdot K^2))$
Electrical conductivity (σ)	Temperature-dependent
T_l	100 °C
T_u	105 °C
$\Delta\sigma$	$1.5\%K^{-1}$
σ_{vap}	$\sigma x10^{-4}$
Density x specific heat (ρc)	Temperature-dependent
T_l	99 °C
T_u	100 °C
C_{water}	0.8 %
$L_{vaporization}$	2260 (KJ/Kg)
ρ_{water}	1000 (Kg/m³)
Cell death model	None
Perfusion	Temperature-dependent
β (T ⩽ 50°C)	1
β (T > 50°C)	0
Time stepping	
algorithm	Lees
$\Delta t_{initial}$	$1x10^{-6}$ s
Δt_{max}	0.5 s
τ_l	0.1 K
τ_u	0.25 K

Table 27: Summary of the simulation parameters used in the cortical Osteoma Osteoide model, in section 4.3.2.

A.5 THREE-STATE CELL DEATH MODEL

Parameter	value
$t_{ablation}$	$300, 600, 900$ s
$t_{incubation}$	$2, 26, 50$ h
$T_{initial}$	$37, 55, 65, 75, 85, 100$ °C
Power control	Constant
V_{el}	0V
Thermal conductivity (k)	Constant
Electrical conductivity (σ)	Constant
Density x specific heat (ρc)	Constant
Cell death model ($t \leqslant t_{ablation}$)	Three-state (Fast)
$\bar{k}_f$	$3.33 \times 10^{-3} s^{-1}$
k_b	$7.77 \times 10^{-3} s^{-1}$
T_f	40.5 °C
Cell death model ($t > t_{ablation}$)	Three-state (Slow)
$\bar{k}_s$	$0.316 \times 10^{-3} s^{-1}$
D_t	0.208
Time stepping	
algorithm	Lees
$\Delta t(t \leqslant t_{ablation})$	1 s
$\Delta t(t > t_{ablation})$	60 s

Table 28: Summary of the simulation parameters used in the three-state cell death verification model, in section 4.3.3.

A.6 SENSITIVITY ANALYSIS OF RF ABLATION PARAMETERS

Parameter	value
$t_{ablation}$	600 s
$T_{initial}$	37 °C
Power control	Impedance control
V_{el}	60 V
$\Omega_{threshold}$	120 Ω
$t_{shutdown}$	15 s
h	$3366W/(K \cdot m^2))$
Thermal conductivity (k)	see table 19
Electrical conductivity (σ)	see table 19
Density x specific heat (ρc)	see table 19
Cell death model	Three-state
$\bar{k}_f$	$3.33x10^{-3}s^{-1}$
k_b	$7.77x10^{-3}s^{-1}$
T_f	40.5 °C
Perfusion	Cell death-dependent
β (D > 80 %)	1
β (D ⩽ 80%)	0
Time stepping	
algorithm	Lees
$\Delta t_{initial}$	$1x10^{-6}$ s
Δt_{max}	0.5 s
τ_l	0.1 ΔT
τ_u	0.25ΔT

Table 29: Summary of the simulation parameters used in the parameter sensitivity model, in section 4.3.4.

A.7 ACT CELL DEATH MODELS

Parameter	value
$t_{ablation}$	600 s
$T_{initial}$	37 °C
Power control	PI-control
T_{target}	90 °C
k_p	1.15
k_i	0.06
Thermal conductivity (k)	Temperature-dependent
T_0	37 °C
T_{max}	100 °C
Δk	$0.003(W/(m \cdot K^2))$
Electrical conductivity (σ)	
type	Temperature-dependent
T_l	100 °C
T_u	105 °C
$\Delta\sigma$	$1.5\%K^{-1}$
σ_{vap}	$\sigma \times 10^{-4}$
Density x specific heat (ρc)	Temperature-dependent
T_l	99 °C
T_u	100 °C
$L_{vaporization}$	2260 (KJ/Kg)
ρ_{water}	1000 (Kg/m^3)
Cell death model (1)	Three-state HEPG2
$\bar{k}_f$	$0.8 \times 10^{-3} s^{-1}$
k_b	$0.25 \times 10^{-3} s^{-1}$
T_f	24.6 °C
Cell death model (2)	Three-state 50/50 HEPG2/MRC-5
$\bar{k}_f$	$3.52 \times 10^{-3} s^{-1}$
k_b	$8.46 \times 10^{-3} s^{-1}$
T_f	41.6 °C
Cell death model (3)	Arrhenius HepG2
A	$5.396 \times 10^{36} s^{-1}$
ΔE	$2.486 \times 10^5 Jmol^{-1}$
Cell death model (4)	Arrhenius SN12
A	$3.153 \times 10^{47} s^{-1}$
ΔE	$3.1489 \times 10^5 Jmol^{-1}$

Cell death model (5)	Arrhenius with delay PC3
A	$6.75 \times 10^{33} \, s^{-1}$
ΔE	$2.222 \times 10^5 \, J mol^{-1}$
b	2703 s
m	49.6 s °C^{-1}
Perfusion	Cell death-dependent
β (D > 80 %)	1
β (D $\leqslant$ 80%)	0
Time stepping	
algorithm	Lees
$\Delta t_{initial}$	1×10^{-6} s
Δt_{max}	0.5 s
τ_l	0.1 K
τ_u	0.25 K

Table 30: Summary of the simulation parameters used in the two-dimensional, axisymmetric, ACT model, in section 5.1.

A.8   ACT PARAMETER SENSITIVITY ANALYSIS

Parameter	value
$T_{initial}$	37 °C
Cool down target	37.05 °C
$t_{ablation}$	600 s
Power control	PI-control
T_{target}	90 °C
k_p	1.15
k_i	0.06
Thermal conductivity (k)	see table 21
Electrical conductivity (σ)	see table 21
Density x specific heat (ρc)	see table 21
Cell death model (1)	Three-state (see table 21)
Cell death model (2)	Arrhenius SN12
A	$3.153 \times 10^{47} s^{-1}$
ΔE	$3.1489 \times 10^5 Jmol^{-1}$
Perfusion	Cell death-dependent
β	see table 21
Time stepping	
algorithm	Lees
$\Delta t_{initial}$	1×10^{-6} s
Δt_{max}	0.5 s
τ_l	0.1 ΔT
τ_u	0.25 ΔT

Table 31: Summary of the simulation parameters used in the two-dimensional, axisymmetric, sensitivity ACT model, in section 5.2.

A.9   PATIENT SPECIFIC SIMULATIONS

Parameter	value
$T_{initial}$	37 °C
Cool down target	37.05 °C
$t_{ablation}$	
Patient 2	600 s, after reaching T_{target}
Patient 7	480 s, after reaching T_{target}
Patient 9	540 s, after reaching T_{target}
Patient 15	540 s, after reaching T_{target}
Power control	PI-control
T_{target}	90 °C
k_p	1.15
k_i	0.06
Thermal conductivity (k)	Temperature-dependent
T_0	37 °C
T_{max}	100 °C
Δk	$0.003(W/(m \cdot K^2))$
Electrical conductivity (σ)	Temperature-dependent
T_0	37 °C
T_{max}	100 °C
$\Delta \sigma$	$1.5\% K^{-1}$
σ_{vap}	$\sigma x 10^{-4}$
Density x specific heat (ρc)	Temperature-dependent
T_l	99 °C
T_u	100 °C
$L_{vaporization}$	2260 (KJ/Kg)
ρ_{water}	1000 (Kg/m^3)
Cell death model	Arrhenius SN12
A	$3.153 x 10^{47} s^{-1}$
ΔE	$3.1489 x 10^5 J mol^{-1}$
Perfusion	Cell death-dependent
β	see table 22
Time stepping	
algorithm	Lees
$\Delta t_{initial}$	$1 x 10^{-6}$ s
Δt_{max}	0.5 s
τ_l	0.1 K

τ_u	0.25 K

Table 32: Summary of the simulation parameters used in the patient specific ACT model, in section 5.3.

[1] R. Lencioni et al. "Percutaneous image-guided radiofrequency ablation in the therapeutic management of hepatocellular carcinoma." In: *Abdominal Imaging* 30.4 (2005), pp. 401–408. ISSN: 1432-0509. DOI: 10.1007/s00261-004-0254-8. URL: https://doi.org/10.1007/s00261-004-0254-8.

[2] Michael J. Stone et al. "Radiofrequency Ablation of Renal Tumors." In: *Tech Vasc Interv Radiol* 10.2 (2007). 18070691[pmid], pp. 132–139. ISSN: 1089-2516. DOI: 10.1053/j.tvir.2007.09.011. URL: http://www.ncbi.nlm.nih.gov/pmc/articles/PMC2621256/.

[3] J. Palussière et al. "Radiofrequency ablation of bone tumours." In: *Diagnostic and Interventional Imaging* 93.9 (2012), pp. 680 – 684. ISSN: 2211-5684. DOI: https://doi.org/10.1016/j.diii.2012.06.008. URL: http://www.sciencedirect.com/science/article/pii/S2211568412002409.

[4] Gaurav Jindal et al. "Palliative Radiofrequency Ablation for Recurrent Prostate Cancer." In: *Cardiovasc Intervent Radiol* 29.3 (2006). 16010507[pmid], pp. 482–485. ISSN: 0174-1551. DOI: 10.1007/s00270-004-0200-8. URL: http://www.ncbi.nlm.nih.gov/pmc/articles/PMC2386884/.

[5] Tiffany Nguyen et al. "Radiofrequency ablation and breast cancer: a review." In: *Gland Surg* 3.2 (2014). gs-03-02-128[PII], pp. 128–135. ISSN: 2227-684X. DOI: 10.3978/j.issn.2227-684X.2014.03.05. URL: http://www.ncbi.nlm.nih.gov/pmc/articles/PMC4115759/.

[6] E. J. Patterson et al. "Radiofrequency ablation of porcine liver in vivo: effects of blood flow and treatment time on lesion size." In: *Ann Surg* 227.4 (1998). 9563546[pmid], pp. 559–565. ISSN: 0003-4932. URL: http://www.ncbi.nlm.nih.gov/pmc/articles/PMC1191313/.

[7] Ramiro M Irastorza et al. "Computer modelling of RF ablation in cortical osteoid osteoma: Assessment of the insulating effect of the reactive zone." In: *International Journal of Hyperthermia* 32.3 (2016). PMID: 26862788, pp. 221–230. DOI: 10.3109/02656736.2015.1135998. eprint: https://doi.org/10.3109/02656736.2015.1135998. URL: https://doi.org/10.3109/02656736.2015.1135998.

[8]   Graham. *Glenn's Urologic Surgery, 7E*. Lww, 2010. ISBN: 0781791413.
       URL: https://www.amazon.com/Glenns-Urologic-Surgery-7E-
       Graham/dp/B007CUBQ54?SubscriptionId=0JYN1NVW651KCA56C102&
       tag=techkie-20&linkCode=xm2&camp=2025&creative=165953&
       creativeASIN=B007CUBQ54.

[9]   Young sun Kim et al. "Intrahepatic recurrence after percuta-
       neous radiofrequency ablation of hepatocellular carcinoma: Anal-
       ysis of the pattern and risk factors." In: *European Journal of Radi-
       ology* 59.3 (2006). Uncommon Traumatic Injuries, pp. 432 –441.
       ISSN: 0720-048X. DOI: https://doi.org/10.1016/j.ejrad.
       2006.03.007. URL: http://www.sciencedirect.com/science/
       article/pii/S0720048X06000908.

[10]   Roy Santosham et al. "How I do it: Radiofrequency ablation."
       In: *Indian J Radiol Imaging* 18.2 (2008). IJRI-18-166[PII], pp. 166–
       170. ISSN: 0971-3026. URL: http://www.ncbi.nlm.nih.gov/pmc/
       articles/PMC2768642/.

[11]   Hendrik Rathke et al. "Comparison of four radiofrequency ab-
       lation systems at two target volumes in an ex vivo bovine liver
       model." In: *Diagn Interv Radiol* 20.3 (2014). dir-20-3-251[PII], pp. 251–
       258. ISSN: 1305-3825. DOI: 10.5152/dir.2013.13157. URL: http:
       //www.ncbi.nlm.nih.gov/pmc/articles/PMC4463338/.

[12]   Frank Williamson. "Richard courant and the finite element method:
       A further look." In: *Historia Mathematica* 7.4 (1980), pp. 369 –
       378. ISSN: 0315-0860. DOI: https://doi.org/10.1016/0315-
       0860(80)90001-4. URL: http://www.sciencedirect.com/
       science/article/pii/0315086080900014.

[13]   H.P. Langtangen and K.A. Mardal. "Introduction to Numerical
       Methods for Variational Problems." Sept. 2016.

[14]   Zhilin Li et al. "Theoretical Foundations of the Finite Element
       Method." In: *Numerical Solution of Differential Equations: Introduc-
       tion to Finite Difference and Finite Element Methods*. Cambridge
       University Press, 2017, 158–180. DOI: 10.1017/9781316678725.
       008.

[15]   J.E. Flaherty. *Finite Element Analysis: Lecture notes at Rensselaer
       Polytechnic Institute*. Accessed on 7-5-2018. URL: http://www.cs.
       rpi.edu/~flaherje.

[16]   E. Sonnendrücker and A. Ratnani. *Advanced Finite Element Meth-
       ods*. Lecture notes at the Max-Planck-Institut für Plasmaphysik
       und Zentrum Mathematik, TU München.

[17]   Eric W. Weisstein. *Fundamental Theorems of Calculus. From MathWorld—
       A Wolfram Web Resource*. Accessed on 9-9-2018. URL: http://
       mathworld.wolfram.com/FundamentalTheoremsofCalculus.html.

[18] Eric W. Weisstein. *Schwarz's Inequality. From MathWorld—A Wolfram Web Resource*. Accessed on 9-9-2018. URL: http://mathworld.wolfram.com/SchwarzsInequality.html.

[19] W.D. Van Suijlekom. *Multi-Index Notation. From MathWorld—A Wolfram Web Resource*. Accessed on 12-9-2018. URL: http://mathworld.wolfram.com/Multi-IndexNotation.html.

[20] Cristopher Stover and Eric W. Weisstein. *Lax-Milgram Theorem. From MathWorld—A Wolfram Web Resource*. Accessed on 22-9-2018. URL: http://mathworld.wolfram.com/Lax-MilgramTheorem.htmll.

[21] J. H. Bramble and S. R. Hilbert. "Estimation of Linear Functionals on Sobolev Spaces with Application to Fourier Transforms and Spline Interpolation." In: 7.1 (1970), pp. 112–124. ISSN: 00361429. URL: http://www.jstor.org/stable/2949585.

[22] Endre Süli and David F. Mayers. *An Introduction to Numerical Analysis*. Cambridge University Press, 2012. ISBN: 0511801181. URL: https://www.amazon.com/Introduction-Numerical-Analysis-Endre-252/dp/0511801181?SubscriptionId=AKIAIOBINVZYXZQZ2U3A&tag=chimbori05-20&linkCode=xm2&camp=2025&creative=165953&creativeASIN=0511801181.

[23] Martin S. Alnæs et al. "The FEniCS Project Version 1.5." In: *Archive of Numerical Software* 3.100 (2015). DOI: 10.11588/ans.2015.100.20553.

[24] Enrique J. Berjano. "Theoretical modeling for radiofrequency ablation: state-of-the-art and challenges for the future." In: *BioMedical Engineering OnLine* 5.1 (2006), p. 24. ISSN: 1475-925X. DOI: 10.1186/1475-925X-5-24. URL: https://doi.org/10.1186/1475-925X-5-24.

[25] C. Rossmanna and D. Haemmerich. "Review of temperature dependence of thermal properties, dielectric properties, and perfusion of biological tissues at hyperthermic and ablation temperatures." In: *Crit Rev Biomed Eng* 42.6 (2014), pp. 467–492.

[26] I. Chang et al. "Effects of perfusion on radiofrequency ablation in swine kidneys." In: *Radiology* 231.2 (2004), pp. 500–505.

[27] D. Haemmerich and J. G. Webster. "Automatic control of finite element models for temperature-controlled radiofrequency ablation." In: *Biomed Eng Online* 4 (2005), p. 42.

[28] R. M. Irastorza et al. "Radiofrequency Ablation of Osteoma Osteoide: A Finite Element Study." In: *VI Latin American Congress on Biomedical Engineering CLAIB 2014, Paraná, Argentina 29, 30 & 31 October 2014*. Ed. by Ariel Braidot and Alejandro Hadad. Cham: Springer International Publishing, 2015, pp. 858–862. ISBN: 978-3-319-13117-7.

[29] S. Delis et al. "The imprint of radiofrequency in the management of hepatocellular carcinoma." In: *HPB (Oxford)* 8.4 (2006), pp. 255–263.

[30] S Gabriel et al. "The dielectric properties of biological tissues: II. Measurements in the frequency range 10 Hz to 20 GHz." In: *Physics in Medicine Biology* 41.11 (1996), p. 2251. URL: http://stacks.iop.org/0031-9155/41/i=11/a=002.

[31] Macarena Trujillo and Enrique Berjano. "Review of the mathematical functions used to model the temperature dependence of electrical and thermal conductivities of biological tissue in radiofrequency ablation." In: *International Journal of Hyperthermia* 29.6 (2013), pp. 590–597. DOI: 10.3109/02656736.2013.807438. eprint: https://doi.org/10.3109/02656736.2013.807438. URL: https://doi.org/10.3109/02656736.2013.807438.

[32] Henry Hu and Stavros A Argyropoulos. "Mathematical modelling of solidification and melting: a review." In: *Modelling and Simulation in Materials Science and Engineering* 4.4 (1996), p. 371. URL: http://stacks.iop.org/0965-0393/4/i=4/a=004.

[33] Xiaoming He and John C. Bischof. "The Kinetics of Thermal Injury in Human Renal Carcinoma Cells." In: *Annals of Biomedical Engineering* 33.4 (2005), pp. 502–510. ISSN: 1573-9686. DOI: 10.1007/s10439-005-2508-1. URL: https://doi.org/10.1007/s10439-005-2508-1.

[34] Y. Feng et al. "A two-state cell damage model under hyperthermic conditions: theory and in vitro experiments." In: *J Biomech Eng* 130.4 (2008), p. 041016.

[35] Zhenpeng Qin et al. "Correlated Parameter Fit of Arrhenius Model for Thermal Denaturation of Proteins and Cells." In: *Ann Biomed Eng* 42.12 (2014). 25205396[pmid], pp. 2392–2404. ISSN: 0090-6964. DOI: 10.1007/s10439-014-1100-y. URL: http://www.ncbi.nlm.nih.gov/pmc/articles/PMC4709256/.

[36] J. A. Pearce. "Comparative analysis of mathematical models of cell death and thermal damage processes." In: *Int J Hyperthermia* 29.4 (2013), pp. 262–280.

[37] Ramiro M. Irastorza et al. "How coagulation zone size is underestimated in computer modeling of RF ablation by ignoring the cooling phase just after RF power is switched off." In: *International Journal for Numerical Methods in Biomedical Engineering* 33.11 (). e2869 CNM-Dec-16-0280, e2869. DOI: 10.1002/cnm.2869. eprint: https://onlinelibrary.wiley.com/doi/pdf/10.1002/cnm.2869. URL: https://onlinelibrary.wiley.com/doi/abs/10.1002/cnm.2869.

[38]   J. A. Pearce. "Improving Accuracy in Arrhenius Models of Cell Death: Adding a Temperature-Dependent Time Delay." In: *J Biomech Eng* 137.12 (2015), p. 121006.

[39]   D. P. O'Neill et al. "A three-state mathematical model of hyperthermic cell death." In: *Ann Biomed Eng* 39.1 (2011), pp. 570–579.

[40]   B. Shah and S. Bhowmick. "Evaluation of important treatment parameters in supraphysiological thermal therapy of human liver cancer HepG2 cells." In: *Ann Biomed Eng* 34.11 (2006), pp. 1745–1757.

[41]   S. A. Sapareto et al. "Effects of hyperthermia on survival and progression of Chinese hamster ovary cells." In: *Cancer Res.* 38.2 (1978), pp. 393–400.

[42]   Milton Lees. "A linear three-level difference scheme for quasilinear parabolic equations." In: *Mathematics of Computation* 20.96 (1966), pp. 516–516. DOI: 10.1090/s0025-5718-1966-0207224-5. URL: https://doi.org/10.1090/s0025-5718-1966-0207224-5.

[43]   G. Comini et al. "Finite element solution of non-linear heat conduction problems with special reference to phase change." In: *International Journal for Numerical Methods in Engineering* 8.3 (), pp. 613–624. DOI: 10.1002/nme.1620080314. eprint: https://onlinelibrary.wiley.com/doi/pdf/10.1002/nme.1620080314. URL: https://onlinelibrary.wiley.com/doi/abs/10.1002/nme.1620080314.

[44]   C. Bonacina and G. Comini. "On the solution of the nonlinear heat conduction equations by numerical methods." In: *International Journal of Heat and Mass Transfer* 16.3 (1973), pp. 581–589. ISSN: 0017-9310. DOI: https://doi.org/10.1016/0017-9310(73)90225-1. URL: http://www.sciencedirect.com/science/article/pii/0017931073902251.

[45]   S. K. Hall et al. "Cell death, perfusion and electrical parameters are critical in models of hepatic radiofrequency ablation." In: *Int J Hyperthermia* 31.5 (2015), pp. 538–550.

[46]   David W. Hahn and M. Necati Özisik. *Heat Conduction*. Wiley, 2012. ISBN: 0470902930. URL: https://www.amazon.com/Heat-Conduction-David-W-Hahn/dp/0470902930?SubscriptionId=AKIAIOBINVZYXZQZ2U3A&tag=chimbori05-20&linkCode=xm2&camp=2025&creative=165953&creativeASIN=0470902930.

[47]   A. Paladini et al. "Osteoid osteoma treated with radiofrequency ablation in non-operating room anesthesia. A different way of approaching ablative therapy on osteoid osteoma." In: *Eur Rev Med Pharmacol Sci* 22.17 (2018), pp. 5438–5446.

[48] B. Jankharia and N. Burute. "Percutaneous radiofrequency ablation for osteoid osteoma: How we do it." In: *Indian J Radiol Imaging* 19.1 (2009), pp. 36–42.

[49] Rudi G. Bitsch et al. "Osteoid Osteoma in an ex Vivo Animal Model: Temperature Changes in Surrounding Soft Tissue during CT-guided Radiofrequency Ablation." In: *Radiology* 238.1 (2006). PMID: 16293805, pp. 107–112. DOI: 10.1148/radiol.2381041500. eprint: https://doi.org/10.1148/radiol.2381041500. URL: https://doi.org/10.1148/radiol.2381041500.

[50] Stryker 1998-2018. *Stryker Cannulae and Electrodes*. 2018. URL: https://www.stryker.com/us/en/interventional-spine/products/cannulae-and-electrodes.html (visited on 02/02/2018).

[51] Georg W. Omlor et al. "Enchondromas and atypical cartilaginous tumors at the proximal humerus treated with intralesional resection and bone cement filling with or without osteosynthesis: retrospective analysis of 42 cases with 6 years mean follow-up." In: *World Journal of Surgical Oncology* 16.1 (2018), p. 139. ISSN: 1477-7819. DOI: 10.1186/s12957-018-1437-z. URL: https://doi.org/10.1186/s12957-018-1437-z.

[52] K. Yamakado et al. "Radiofrequency ablation for the treatment of recurrent bone and soft-tissue sarcomas in non-surgical candidates." In: *Int. J. Clin. Oncol.* 19.5 (2014), pp. 955–962.

[53] C. Lagergren et al. "The Blood Vessels of Chondrosarcomas." In: *Acta Radiologica* 55.5 (1961), pp. 321–328. DOI: 10.3109/00016926109175125. eprint: https://doi.org/10.3109/00016926109175125. URL: https://doi.org/10.3109/00016926109175125.

[54] Pernick N. *Chondrosarcoma: conventional*. [Online; accessed 12-12-2018]. URL: http://www.pathologyoutlines.com/topic/bonechondrosarcomaconventional.html.

[55] M. Zileli et al. "Osteoid osteomas and osteoblastomas of the spine." In: *Neurosurg Focus* 15.5 (2003), E5.

[56] U. Mayrhauser et al. "Cell to cell interactions influence sensitivity of liver cell lines during hyperthermia." In: *Anticancer Res.* 31.11 (2011), pp. 3713–3717.

[57] R. M. Irastorza et al. "How coagulation zone size is underestimated in computer modeling of RF ablation by ignoring the cooling phase just after RF power is switched off." In: *Int J Numer Method Biomed Eng* 33.11 (Nov. 2017).

[58] Baumgartner C Neufeld E Lloyd B Gosselin MC Payne D Klingenböck A Kuster N Hasgall PA Di Gennaro F. "IT'IS Database (V4.0) for thermal and electromagnetic parameters of biological tissues." In: 4.0 (May 2018). DOI: 10.13099/VIP21000-04-0.

[59] Gabriel Camelia. "Compilation of the Dielectric Properties of Body Tissues at RF and Microwave Frequencies." In: 272 (1996).

[60] J. Lang et al. "Impact of nonlinear heat transfer on temperature control in regional hyperthermia." In: *IEEE Transactions on Biomedical Engineering* 46.9 (1999), pp. 1129–1138. ISSN: 0018-9294. DOI: 10.1109/10.784145.

[61] Christophe Geuzaine and Jean-François Remacle. "Gmsh: A 3-D finite element mesh generator with built-in pre- and post-processing facilities." In: *International Journal for Numerical Methods in Engineering* 79.11 (), pp. 1309–1331. DOI: 10.1002/nme.2579. eprint: https://onlinelibrary.wiley.com/doi/pdf/10.1002/nme.2579. URL: https://onlinelibrary.wiley.com/doi/abs/10.1002/nme.2579.

[62] Qingnan Zhou. *Pymesh: a rapid prototyping platform focused on geometry processing*. [Online; accessed 02-09-2018]. 2018–. URL: https://pymesh.readthedocs.io/en/latest/index.html.

[63] Chun-Cheng R. Chen et al. "Optimizing needle placement in treatment planning of radiofrequency ablation." In: 6141 (Mar. 2006).